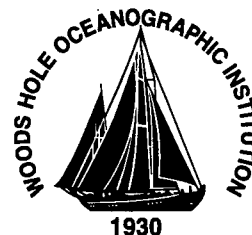


MIT/WHOI 00-08

**Massachusetts Institute of Technology
Woods Hole Oceanographic Institution**



**Joint Program
in Oceanography/
Applied Ocean Science
and Engineering**



DOCTORAL DISSERTATION

*Broadband Modal Coherence and Beamforming at
Megameter Ranges*

by

Kathleen E. Wage

February 2000

DTIC QUALITY INSPECTED 4

20001129 047

MIT/WHOI

00-08

Broadband Modal Coherence and Beamforming at Megameter Ranges

by

Kathleen E. Wage

Massachusetts Institute of Technology
Cambridge, Massachusetts 02139

and

Woods Hole Oceanographic Institution
Woods Hole, Massachusetts 02543

February 2000

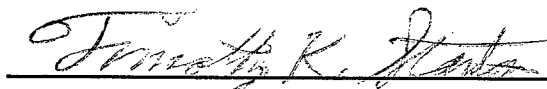
DOCTORAL DISSERTATION

Funding was provided by Office of Naval Research grant N00014-97-1-0788, a subcontract to the University of California-Scripps ATOC Agreement PO #10037359, and a GE Fund Faculty for the Future Fellowship.

Reproduction in whole or in part is permitted for any purpose of the United States Government. This thesis should be cited as: Kathleen E. Wage, 2000. Broadband Modal Coherence and Beamforming at Megameter Ranges. Ph.D. Thesis. MIT/WHOI, 00-08.

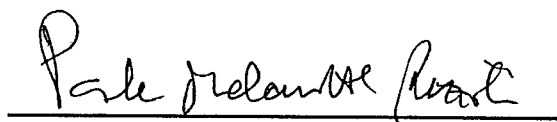
Approved for publication; distribution unlimited.

Approved for Distribution:



Timothy K. Stanton, Chair

Department of Applied Ocean Physics and Engineering



Paola Malanotte-Rizzoli
MIT Director of Joint Program



John W. Farrington
WHOI Dean of Graduate Studies

Broadband Modal Coherence and Beamforming at Megameter Ranges

by

Kathleen E. Wage

B.S., University of Tennessee (1990)

S.M., Massachusetts Institute of Technology (1994)

E.E., Massachusetts Institute of Technology (1996)

Submitted in partial fulfillment of the
requirements for the degree of

Doctor of Philosophy

at the

MASSACHUSETTS INSTITUTE OF TECHNOLOGY

and the

WOODS HOLE OCEANOGRAPHIC INSTITUTION

February 2000

©2000 Massachusetts Institute of Technology. All rights reserved.

Signature of Author Kathleen E. Wage
MIT Department of Electrical Engineering and Computer Science
MIT/WHOI Joint Program in Applied Ocean Science and Engineering
December 13, 1999

Certified by Arthur B. Baggeroer
Arthur B. Baggeroer, Thesis Supervisor
Ford Professor of Engineering
Secretary of the Navy/Chief of Naval Operations Chair for Ocean Science
Massachusetts Institute of Technology

Certified by James C. Preisig
James C. Preisig, Thesis Supervisor
Assistant Scientist, Woods Hole Oceanographic Institution

Accepted by Arthur C. Smith
Arthur C. Smith
Chairman, EECS Departmental Committee on Graduate Students
Massachusetts Institute of Technology

Accepted by Michael Triantafyllou
Michael Triantafyllou
Chairman, Joint Committee for Applied Ocean Science and Engineering
Massachusetts Institute of Technology/Woods Hole Oceanographic Institution

Broadband Modal Coherence and Beamforming at Megameter Ranges

by

Kathleen E. Wage

Submitted to the MIT Department of Electrical Engineering and Computer Science
and to the WHOI Department of Applied Ocean Science and Engineering
on December 13, 1999, in partial fulfillment of the
Requirements for the degree of Doctor of Philosophy in
Electrical Engineering

Abstract

This thesis develops a method for estimating the normal mode decomposition of broadband signals and uses it to analyze data from the Acoustic Thermometry of Ocean Climate (ATOC) experiment. Normal modes are the eigenfunctions of the ocean waveguide, derived from the frequency-domain wave equation. They are useful in underwater acoustics, particularly matched field processing and tomography, because the lowest modes provide an efficient description of the most energetic arrivals at long ranges. Extracting source or environmental information from the mode signals depends on understanding the effects of internal waves on coherence and the validity of adiabatic approximation. While much theoretical research has been done on long-range propagation of modes in deep water, there have been few opportunities to compare theoretical predictions with experimental measurements.

The first contribution of this thesis is a short-time Fourier framework for estimating broadband signals propagating in the lowest modes of the ocean waveguide. Since previous research has focused primarily on narrowband sources, this work concentrates on broadband processing issues. Specifically, it addresses the fundamental issue of frequency resolution required for mode estimation, analyzes the performance characteristics of two modal beamforming algorithms and explores the time/frequency tradeoffs inherent in STFT mode processing.

The second contribution of this research is a detailed analysis of the low-mode arrivals at megameter ranges using five months of data from the ATOC vertical line array at Hawaii (3515 km range). Short-time Fourier processing of these receptions revealed that each low mode contains a series of arrivals, rather than the single dispersive arrival that would characterize adiabatic propagation. Average coherence times of the mode signals are on the order of 6-8 minutes. The multipath structure changes significantly between receptions at 4-hour intervals, indicating that stochas-

tic methods are required for mode tomography at megameter ranges. A statistical analysis found that modes do retain travel-time information at megameter ranges, *e.g.*, the centroids show the expected dispersion characteristics of a deep water channel. The centroids show statistically significant trends in mode arrival time over the period of the experiment.

Thesis Supervisor: Arthur B. Baggeroer
Ford Professor of Engineering
Secretary of the Navy/Chief of Naval Operations Chair for Ocean Science
Massachusetts Institute of Technology

Thesis Supervisor: James C. Preisig
Assistant Scientist, Woods Hole Oceanographic Institution

Acknowledgements

First, I would like to thank my parents and my brother David for their love and support. You are truly a blessing in my life, and none of this would have been possible without you.

I thank my advisors, Arthur Baggeroer and Jim Preisig for sharing their ideas and insights, challenging me to and providing encouragement along the way. I hope that we will have the opportunity to work together in the future. I am very grateful for the advice and encouragement of my thesis committee members, John Colosi and David Staelin. Thanks also to Gregory Wornell for agreeing to serve as the chair of my defense at the last minute. I am thankful to Alan Oppenheim for all of his support and encouragement throughout the years. I consider my experience working as a teaching assistant with him on 6.011 to be one of the most valuable aspects of my experience at MIT.

I have learned a great deal from my colleagues in the Digital Signal Processing Group. Former DSPG'ers John Buck and Andy Singer welcomed me into the group and have definitely influenced my development as a researcher. I look forward to many years of friendship and collaboration in the future. Over the past several years, it has been a pleasure to share an office and many conversations with Matt Secor and Wade Torres. I appreciate Giovanni Aliberti for his kindness and generosity and for sharing his vast knowledge of computer systems. Both Maggie Beucler and Darla Chupp Secor have brightened my day on many occasions, and their presence helped make DSPG a great place to work. On the ocean acoustics side, I feel grateful for wonderful colleagues such as Brian Sperry and Peter Daly. I am thankful to them for many interesting conversations and feedback about my work.

Susan Worst has been a constant source of support and inspiration (and editorial assistance!) these past few years, and I can't imagine what I would do without her. I am indebted to my friend/priest/mentor Jane Gould for her good advice, willingness to learn a little about underwater acoustics, and at least a million cups of tea. Amy ("friend, but not so good") Troutman and Melissa ("Dr. Marlin") Caldwell have helped me stay sane by getting a little crazy at times. I am thankful to have such good friends and look forward to many future adventures, at home and abroad. Lisa Tucker-Kellogg and I have shared experiences in grad school and church, and our 8:30 am meetings played a key role in helping me finish this thesis. For their encouragement and friendship, I am also very grateful to Larry Cohen, Joanne Engquist, Sumila Gulyani, Karianne Hoier Kjolaas, Alice Liu, Kelly Poort, Trish Weinmann, and all of the members of the Lutheran-Episcopal Ministry.

This research was made possible by the experimental work carried out by the ATOC Group. I gratefully acknowledge financial support from the following sources: the University of California-Scripps ATOC Agreement, PO # 10037359, a subcontract to the University of California; a GE Fund Faculty for the Future Fellowship; and the Office of Naval Research Grant N00014-97-1-0788.

For Mom, Dad, and David

Contents

Table of Contents	6
List of Figures	7
1 Introduction	14
1.1 Use of Modes in Long-Range Acoustics	15
1.2 Broadband Mode Estimation at Megameter Ranges	18
1.3 Acoustic Thermometry of Ocean Climate Experiment	19
1.4 Thesis Objectives	20
2 Background	22
2.1 Broadband Normal Mode Representation	23
2.1.1 “Local” Orthonormal Basis	23
2.1.2 Mode Propagation	27
2.2 Broadband Mode Estimation Problem	37
2.3 Previous Work	40
2.4 Approach	45
3 Short-time Fourier Mode Processing	47
3.1 Overview of the STFT Framework	48
3.2 Mode Processing With Vertical Arrays	50

3.2.1	Broadband Processor Derivation	50
3.2.2	Narrowband Mode Filters	52
3.2.3	Narrowband Performance Analysis	58
3.2.4	Broadband Performance Analysis	64
3.3	Adiabatic Example	73
3.3.1	Processing Results	73
3.3.2	Analysis	75
3.4	Mooring Corrections	84
3.5	Impact of Environmental Uncertainty	86
3.6	Summary	88
4	STFT Mode Analysis of ATOC Receptions	91
4.1	ATOC Data Set	92
4.2	Simulated Data Set	97
4.3	Modal Time Series: Experiment vs. Simulation	98
4.3.1	ATOC Reception	99
4.3.2	Simulated Receptions	102
4.3.3	Downslope Propagation Example	107
4.4	Temporal Variability	111
4.5	Mode Statistics	115
4.6	Summary	128
5	Conclusions and Future Directions	131
A	Acoustic Mode Perturbations	136

List of Figures

1-1	Deep ocean waveguide. The left panel shows a typical deep water sound speed profile. The right panel illustrates how refractive effects permit propagation over extremely long ranges.	15
1-2	Broadband reception on 40-element VLA located 3515 km from source	16
1-3	ATOC source and receivers	19
2-1	Sound speed at the ATOC Hawaii array (20.2°N, −154.0°E). The solid line is the profile obtained using temperature and salinity from the Levitus database for the winter season. The dashed line corresponds to the profile computed from a CTD measurement taken at the time of array deployment (mid-November 1995).	25
2-2	Comparison of Levitus environment and measured environment at Hawaii. The left panel shows a closeup of the sound speed profiles around the channel axis. The right panel shows the modeshapes for the first 10 modes at 75 Hz in each environment.	26
2-3	Modeshapes for the first 10 modes of the Hawaii-Levitus environment at 60 Hz and 90 Hz. The plot shows the upper 2500 meters of the 5250 meter waveguide.	27

2-4	ATOC environment: geodesic path between source at Pioneer Seamount (off California) and the receiving array near Hawaii. The left panel is the average sound speed profile over the path, computed using 235 sections (≈ 15 km apart). The right panel shows the differences between the mean profile and the Levitus (winter) profile for each of the sections. Depth of the ocean bottom, shown in black, is taken from bathymetric surveys of Pioneer Seamount [1] and the ETOPO-5 topography database [2].	30
2-5	Sound speed perturbations due to internal waves at $1/2$ Garrett-Munk strength	31
2-6	Range-averaged group velocities for the first 40 modes of the CA-HI Levitus environment	32
2-7	Adiabatic predictions of mode time spread due to dispersion	32
2-8	PE simulation through Levitus environment. The top panel is the received pressure on a 40-element VLA; the bottom panel shows the corresponding arrival time series in the first 10 modes	33
2-9	PE simulation through Levitus environment plus internal waves	33
2-10	Proposed short-time Fourier mode processing framework	45
3-1	Block diagram of STFT-based mode processor	49
3-2	Modeshapes (75 Hz) and receiver locations (+’s) for the design example	59
3-3	MF Beampattern (75 Hz) for the 40-element ATOC VLA in the Hawaii-Levitus environment	60
3-4	Comparison of pseudo-inverse filter beampatterns (75 Hz) for the ATOC array in the Hawaii-Levitus environment	61
3-5	White noise gain at 75 Hz for the ATOC array in the Hawaii-Levitus environment	62
3-6	Maximum crosstalk	63

3-7	Frequency response of the matched filter. Solid lines indicate the response in the desired mode; dashed lines indicate crosstalk from neighboring modes (up to 10).	65
3-8	Frequency response of the PI filter designed for 10 modes. Solid lines indicate the response in the desired mode; dashed lines indicate crosstalk from neighboring modes (up to 10).	66
3-9	Frequency response of the PI filter for mode 10 (designed using 10 modes)	69
3-10	Time and frequency responses for three Hanning windows, assuming a 300 Hz sample rate. Amplitude differences among the impulse responses are a result of constraining the response to be equal to 1 at 0 Hz.	70
3-11	Simple illustration of time resolution imposed by the lowpass filter . .	71
3-12	White noise gain as a function of frequency for the matched filter and three different pseudo-inverse filters (for 10 modes, 12 modes, and 15 modes).	72
3-13	STFT example: processing of adiabatic propagation data. Top plot is the received pressure on a 40-element array as a function of time and depth. The bottom plots show the frequency-stacked outputs for modes 1 and 5, respectively.	74
3-14	Estimated frequency-stacked outputs for the first 10 modes, computed using a pseudo-inverse filter	76
3-15	Difference in range-averaged wavenumber and 3-term Taylor series approximation for the CA-HI Levitus environment. Note that the phase differences are scaled by the range (3515 km) of the ATOC experiment and normalized by π	79
3-16	Magnitude and phase across frequency at the peak arrival time in the 75 Hz bin for modes 1 and 5 of the adiabatic example	82

3-17	Difference in delay	86
3-18	Comparison of deployment and recovery sound speed profiles	87
3-19	Comparison of deployment and recovery modeshapes at 75 Hz	88
3-20	Beampattern for the mismatch case: PI filter designed with deployment profile modeshapes; recovery profile modes are the input	89
3-21	Beampattern for the mismatch case: matched filter designed with deployment profile modeshapes; recovery profile modes are the input	89
4-1	ATOC transmission schedule through yearday 509. Crosses mark the time of each good reception; receptions with bad channels have been eliminated from the data set. The line of numbers below the crosses indicates how the receptions are divided into 13 subgroups for post-processing.	93
4-2	Estimated noise spectra for hydrophones 10 and 30. The solid line is computed using the noise-only section prior to the signal arrival; dashed line is computed using the noise-only section after the signal arrivals.	94
4-3	Estimated spatial covariance in the 75 Hz bin; calculated from 300 snapshots. Units are dB, referenced to peak value.	95
4-4	Input noise levels at 60, 75, and 90 Hz as a function of reception number.	96
4-5	ATOC Reception	100
4-6	PE simulation without internal waves	100
4-7	PE simulation with internal waves at 1/2 Garrett-Munk strength	100
4-8	Frequency-stacked mode estimates for the ATOC reception in Fig. 4-5. Color scale is in dB.	101
4-9	Frequency-stacked mode estimates for the PE simulation without internal waves in Fig. 4-6. Black lines in each subplot are the predicted arrival times based on adiabatic dispersion curves.	104

4-10	Frequency-stacked mode estimates for the PE simulation with internal waves in Fig. 4-7	105
4-11	Comparison of ATOC data, PE simulations, and adiabatic predictions for modes 1 and 10.	106
4-12	Bathymetry near the ATOC source at Pioneer Seamount	107
4-13	Comparison of propagation through the environment that includes the actual sloping bottom near the source (top plot) and the environment without the slope (bottom plot)	108
4-14	Comparison of arrivals in modes 1 and 10 for the sloping bottom (top plots) and the zero-slope approximation (bottom plots)	109
4-15	Comparison of the time series for the first 80 modes at 50 km range from the Pioneer Seamount source. Top plot is for the actual slope. Middle two plots are for the 8.5 degree and 4.3 degree approximations, respectively. The bottom plot corresponds to the no slope case. . . .	110
4-16	Comparison of modes 1 and 10 for the first (top plots) and last (bottom plots) periods of a source transmission	112
4-17	Comparison of modes 1 and 10 for realizations of a time-varying internal wave environment. The lag time between the top and bottom plots is 16 minutes.	113
4-18	Temporal coherence as a function of frequency for mode 1 (left plot) and as a function of mode number for the 75 Hz bin (right plot). These results were obtained by averaging across 96 receptions (yeardays 363-435).	114
4-19	Variability of modes 1 and 10 across a single transmission (18.2 minutes) in the 75 Hz bin	115
4-20	Variability of modes 1 and 6 for the simulated data in the 75 Hz bin, calculated at 4 minute intervals.	116
4-21	Mode 1 in ATOC receptions at 4-hour intervals	117

4-22	Histogram of peak arrivals in the 75 Hz bin. Threshold for peak detection was set at 12 dB above the noise floor. These results were computed from the first 96 good receptions (yeardays 363 to 436). . .	118
4-23	Leading edge, falling edge, and centroid in the 75 Hz bin for the first 20 ATOC receptions, each consisting of 10 four-period averages. . . .	119
4-24	Comparison of average leading and falling edges for the first group of ATOC receptions and the simulated data set	120
4-25	Comparison of average centroid locations for the first group of ATOC receptions, the simulated receptions, and adiabatic predictions	122
4-26	Average centroids as a function of frequency for the first 7 groups of ATOC receptions. Legend is identical to that shown in Fig. 4-25. See Fig. 4-1 for a definition of the groups.	124
4-27	Average centroids as a function of frequency for groups 8-13 of the ATOC receptions. Legend is identical to that shown in Fig. 4-25. See Fig. 4-1 for a definition of the groups.	125
4-28	Average centroids in the 75 Hz bin for modes 1-10 as a function of yearday	126
4-29	Average leading and falling edges for mode 1 in the 75 Hz bin as a function of yearday	127
4-30	Average of the RMS error over 13 groups of receptions as a function of mode number. Results are shown for the centroids and the falling edges of the 75 Hz bin.	128

Chapter 1

Introduction

Normal modes provide a convenient description of low-frequency sound in the deep ocean. Their strong connection to the propagation environment makes them useful in a variety of applications, including source localization and acoustic tomography. Currently, there is much interest in using modes to analyze broadband receptions at megameter ranges for the purpose of studying ocean variability on basin-scales. At these ranges, the effects of internal waves on mode coherence are not known. This thesis develops a signal processing framework for estimating modal time series and uses it for analyzing data from the Acoustic Thermometry of Ocean Climate experiment. From a signal processing perspective, the key issue to consider is the broadband nature of the signals; specifically, any approach must accommodate variations in the mode characteristics across the bandwidth of the source. In examining the data, the focus is on understanding the fluctuations of mode arrivals and characterizing the complicated multipath structure.

The rest of this chapter introduces the research questions addressed by this thesis. As a starting point, the following section motivates the use of the modal description in the context of long-range acoustics and discusses open questions about megameter propagation. The second section highlights some of the signal processing issues surrounding the broadband mode estimation problem. Section 1.3 describes the

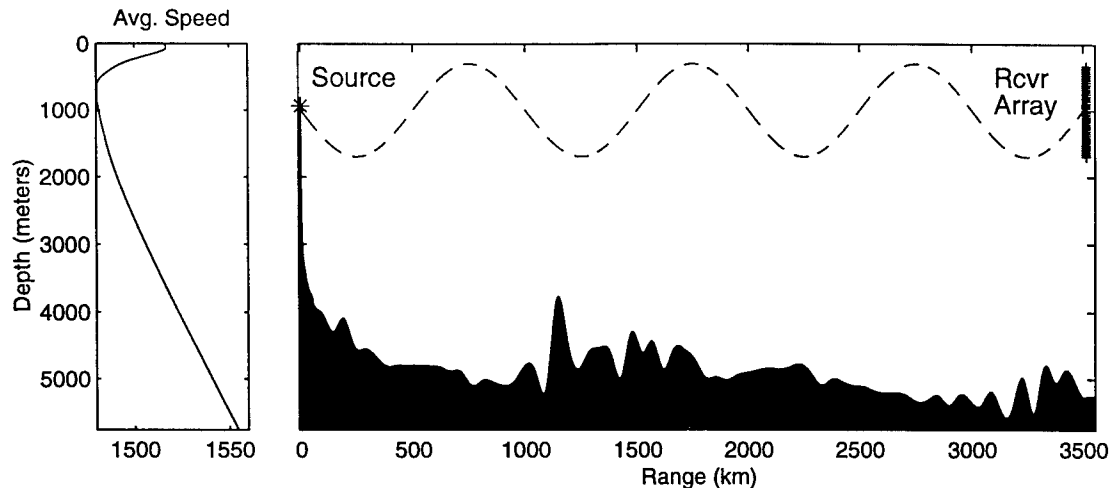


Figure 1-1: Deep ocean waveguide. The left panel shows a typical deep water sound speed profile. The right panel illustrates how refractive effects permit propagation over extremely long ranges.

opportunities presented by the recent ATOC experiment. Finally, Section 1.4 states the specific research objectives and outlines the remainder of the thesis.

1.1 Use of Modes in Long-Range Acoustics

The deep ocean is an efficient channel because it traps low-frequency acoustic signals, enabling them to be detected thousands of kilometers from their source. Figure 1-1 shows how the refractive effects of the underwater waveguide allows propagation to such long ranges. Acoustically, the deep ocean is characterized by a sound speed profile with a minimum, between 800 and 1200 meters depth, known as the sound channel axis. Sound waves bend towards regions of lower velocity, thus the minimum creates a duct. As the figure depicts, a sound wave leaving the source on a downward trajectory bends back towards the axis. Once it passes through the minimum on an upward path, it bends away from the surface. Purely refracted paths, such as the one shown, do not scatter energy at boundary interactions. Since absorption losses for low frequencies (on the order of 100 Hz) are minimal, the signals can propagate

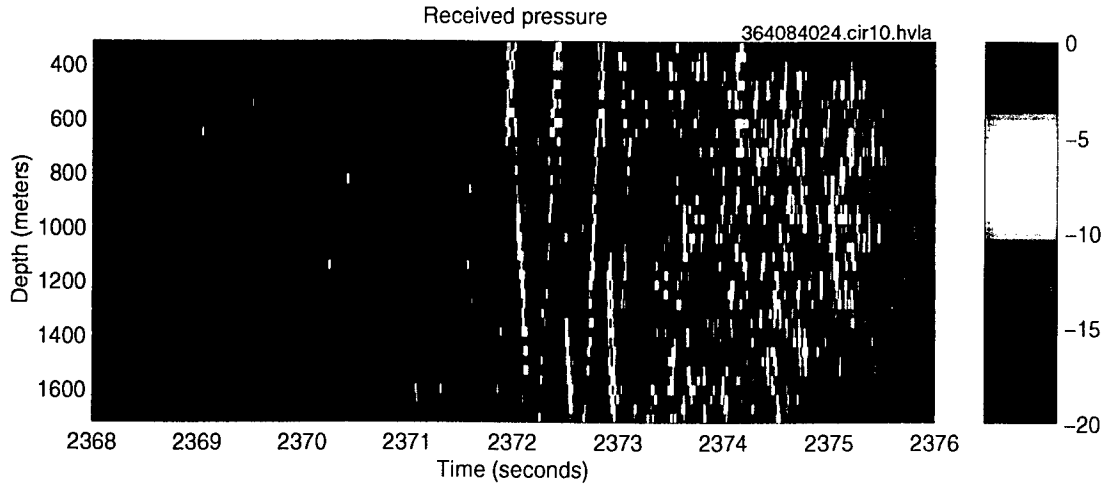


Figure 1-2: Broadband reception on 40-element VLA located 3515 km from source over extremely long distances in the channel.

Fig. 1-2 illustrates some general features of pulse propagation to megameter ranges. The plot shows the pulse-compressed and sequence-averaged time series recorded by a 40-element vertical line array (VLA) located 3515 km from a broadband source. Inter-element spacing is 35 m, and the array is approximately centered on the sound channel axis. This figure reveals an important characteristic of propagation in the underwater sound channel, namely the time-spread of the arrivals due to the fact that they take many different paths between source and receiver. The early arrivals traverse deep-diving ray paths that are associated with higher group velocities because they sample the water away from the sound speed minimum. Signals that propagate almost horizontally, along the sound channel axis, arrive last and are often more energetic. In general, the multipath arrival structure can be represented in terms of the vertical eigenfunctions, or normal modes, of the underwater waveguide. Modal dispersion accounts for the time-spread of the signal at long ranges. In deep water, the high modes travel faster than the low modes, thus the high modes are associated with the early-arriving energy in Fig. 1-2. The planewave-type arrivals visible in the early parts of the reception (up until ≈ 2373 seconds) are the result of constructive interference of groups of these higher order modes. Planewaves are

not evident in the last 2.5 seconds of the reception, associated with the low mode arrivals.

As solutions to the frequency-dependent wave equation, the modes provide many useful insights about sound propagation. Each mode essentially samples a different part of the water column: the low modes are concentrated around the axis, whereas the higher modes have greater vertical extents. Since the modes depend strongly on the environment, they can be used as observables for matched field processing or tomography applications. The key to matched field or tomographic inversions is the ability to associate an arrival with a particular path or section of the water column. In range-invariant environments, this problem is trivial because the modes propagate independently without exchanging energy, *i.e.*, an arrival in mode 1 is known to have traversed the entire path in mode 1. For a realistic ocean environment, however, inhomogeneities cause coupling of energy among the modes, which makes the problem much more difficult. Understanding the mechanisms and effects of mode coupling is crucial to using these signals in any type of application.

At long ranges, internal waves are thought to be the primary source of coupling. Vertical displacements of water associated with internal waves cause fluctuations of the temperature, thus changes in the sound speed, at a fixed depth. The horizontal variability of these sound speed fluctuations, in turn, can cause an exchange of energy among the modes as they propagate. The effects of these fluctuations on the planewave-type arrivals are fairly well-understood - these arrivals are amenable to analysis via geometrical optics approximation. Significantly less is known about the axial mode arrivals since there is no comparable theory. The late-arriving modes tend to describe the most energetic, trapped signals and thus are useful in detecting/estimating weak sources at long range. To develop an understanding of how these low modes propagate through internal wave fields and to test some of the limited theoretical results, it is necessary to study them experimentally.

1.2 Broadband Mode Estimation at Megameter Ranges

Measuring the mode arrival structure at long ranges presents an interesting signal processing problem. Unlike the planewave arrivals, axial mode arrivals generally overlap in time, and must be estimated via spatial processing. Since the modes are an orthonormal basis in depth, in principle they can be separated using vertical line arrays spanning the entire water column. In practice, the degree of orthogonality of the modeshapes, as sampled by a practical array, determines how well the modes can be resolved.

A key issue in this thesis is the use of broadband signals. The modes are inherently frequency-dependent, since they are derived from the frequency-domain wave equation. Previous work on mode estimation has primarily focused on situations where a narrowband approximation is valid, i.e., either the source is CW or the mode functions are approximately constant across the band of the source. A few researchers have implemented broadband mode processors using an FFT for the frequency decomposition, but they have not discussed the frequency resolution required for this approach. What is needed is a general framework for broadband mode estimation that will allow a careful analysis of performance in terms of mode resolution and time/frequency resolution.

A recent experiment provides an opportunity to develop methods of mode processing and to apply them to studying the coherence of mode arrivals at megameter ranges.

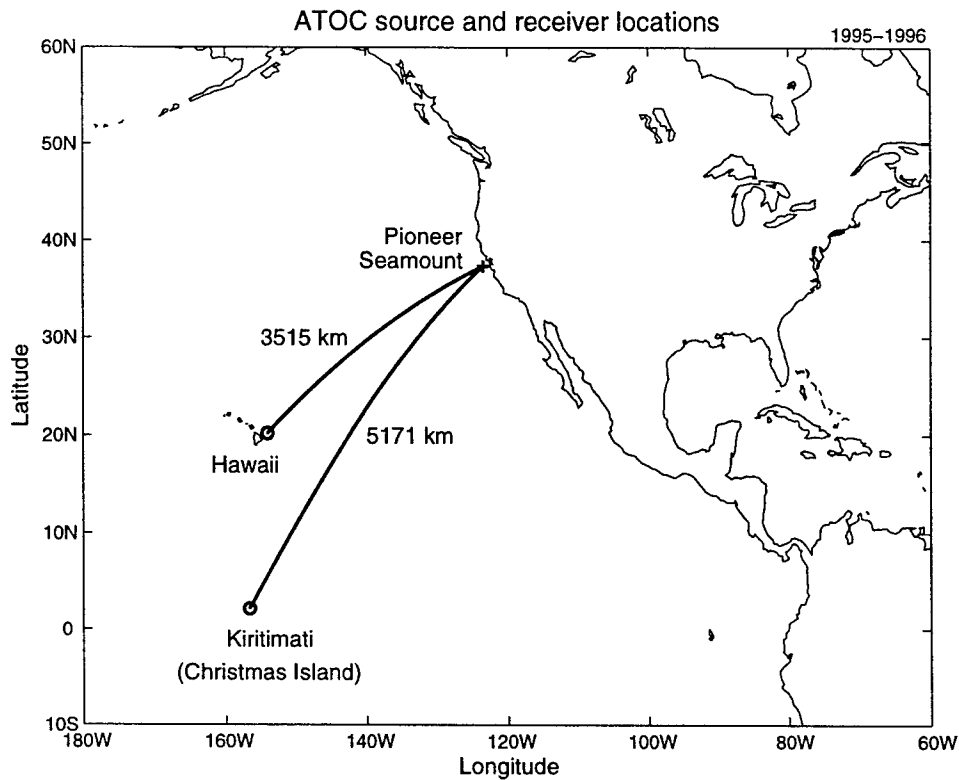


Figure 1-3: ATOC source and receivers

1.3 Acoustic Thermometry of Ocean Climate Experiment

The purpose of the Acoustic Thermometry of Ocean Climate (ATOC) experiment is to study long-range propagation of sound and to investigate acoustic methods for monitoring ocean climate variability. The intent is to demonstrate that travel-time tomography can be used to measure ocean temperature over ranges of 3,000 to 10,000 km. The ATOC network consists of a broadband source off the California coast, two vertical line arrays, and a number of bottom-mounted horizontal arrays. This thesis focuses on analyzing data from the two VLA's, which were designed to spatially resolve the lowest 10 modes at each location. Figure 1-3 shows the location of source and receivers considered in this thesis. The path lengths to the receivers at Hawaii and Kiritimati (Christmas Island) are 3515 km and 5171 km, respectively.

These arrays were deployed in November 1995 and recovered in September of 1996. The bottom-mounted source (934 m) on Pioneer Seamount transmitted pulses at a center frequency of 75 Hz. Each transmission consists of 40 periods of a pseudo-random sequence, phase modulated onto a 75 Hz carrier. The receiver averages every 4-periods internally. Over the duration of the experiment, transmissions are sent every 4 hours during periods established by the ATOC Marine Mammal Research Program.

ATOC presents the first opportunity to study mode arrivals at megameter ranges. The next section outlines the objectives of this thesis.

1.4 Thesis Objectives

The first objective of this research is to define a framework for broadband mode estimation. Since the modeshapes are frequency-dependent and the mode spectral coefficients are time-dependent, mode estimation involves a combination of temporal and spatial filtering. Most previous work has focused primarily on the narrowband mode estimation problem, and has not addressed issues unique to broadband signals.

The second objective is to analyze the low-order mode arrivals in the ATOC data. This is really the first opportunity of its kind. Specifically, this research hopes to characterize the complicated mode arrival structure and explore the effects of internal waves on mode coherence.

The organization of the thesis is as follows. Chapter 2 reviews background about normal mode representations and motivates several specific questions about long-range mode propagation. It clearly formulates the broadband mode estimation problem and proposes an approach for exploring the scientific/signal processing research topics using the ATOC data. Following that, Chapter 3 presents a framework for broadband mode processing, based on short-time Fourier techniques. The fourth chapter presents an analysis of the ATOC data set for the Hawaii array,

compares these results to simulations, and identifies several useful statistics of the mode arrivals. Finally, Chapter 5 summarizes the thesis contributions and indicates directions for future research.

Chapter 2

Background

As indicated in Chapter 1, normal modes are of interest in applications such as tomography and thermometry because the lowest modes provide a convenient description of the energetic late arrivals at megameter ranges. This chapter lays the groundwork for the rest of the thesis by motivating specific questions about long-range mode propagation, clearly formulating the broadband mode estimation problem, and proposing an approach for exploring these research topics using data from the ATOC vertical arrays. The material is divided into four parts. Section 2.1 reviews the salient characteristics of the normal mode representation and outlines some of the open questions concerning mode propagation through range-dependent and random environments. In the course of describing relevant features of the modal basis set, this section also introduces a range-dependent ocean environment, which is used for many of the examples in later chapters. Given this mathematical background and experimental motivation, Section 2.2 poses the mode estimation problem for vertical arrays and highlights important design considerations. In particular, the discussion emphasizes the broadband character of the problem since most prior work has focused on using modes to analyze narrowband signals. The third section reviews previous work on mode estimation in order to place the current research in context. Finally, Section 2.4 outlines the proposed approach, which is based on short-time

Fourier analysis techniques, and describes the areas addressed by the rest of the thesis.

2.1 Broadband Normal Mode Representation

Normal mode representations are useful in describing the acoustic pressure field in a variety of underwater environments. Several standard textbooks develop acoustic mode theory in detail [3, 4, 5]. The following discussion reviews the basic concepts, focusing primarily on modal representations for broadband signals in deep ocean environments such as those encountered in ATOC. This section is split into two parts: the first describes the use of the modes as a “local” basis set for the pressure field; the second discusses mode propagation in a variety of environments.

2.1.1 “Local” Orthonormal Basis

Normal modes are the eigenfunctions of the ocean waveguide, which are derived from the frequency domain wave equation (Helmholtz equation). At each frequency, a mode is characterized by its wavenumber k_m and its modeshape ϕ_m . For a given environment, defined by the sound speed profile and boundary conditions, the modes satisfy a second-order eigenvalue equation, *e.g.*, in cylindrical coordinates (assuming constant density):

$$\frac{d^2 \phi_m(r, z, \Omega)}{dz^2} + [k^2(r, z, \Omega) - k_m^2(r, \Omega)] \phi_m(r, z, \Omega) = 0; \quad k(r, z, \Omega) \equiv \frac{\Omega}{c(r, z)}. \quad (2.1)$$

In Eq. 2.1, Ω is the temporal frequency, $c(r, z)$ is the sound speed as a function of range r and depth z , and $k(r, z, \Omega)$ is the medium wavenumber. The modal wavenumber (k_m) determines propagation characteristics, such as phase and group speeds, and the modeshape determines the spatial distribution of pressure due to

each mode. These shapes are orthogonal functions, scaled such that

$$\frac{1}{\rho} \int_0^{z_{max}} \phi_m(\Omega, z) \phi_n(\Omega, z) dz = \delta(m - n), \quad (2.2)$$

where ρ is the density of water.

Since the modes are an orthonormal basis for narrowband signals, the pressure field at coordinates (r, z) can be represented as the weighted sum

$$p(r, z, \Omega) = \sum_m a_m(r, \Omega) \phi_m(r, z, \Omega) \quad (2.3)$$

where a_m is the frequency-dependent coefficient for mode m . In general, the sum in Eq. 2.3 is infinite, although in most realistic environments only a finite number of modes contribute significantly to the field. The remaining “leaky” modes have complex wavenumbers and suffer exponential losses as they propagate, thus their contributions are negligible in the far-field of the source. This thesis focuses on long-range propagation scenarios where it is reasonable to represent the pressure field with a finite set of modes.

Time- and frequency-domain representations of the pressure are related via Fourier synthesis, *i.e.*, the time series for a receiver at range r and depth z is

$$\psi(r, z, t) = \frac{1}{2\pi} \int_{\Omega} p(r, z, \Omega) e^{j\Omega t} d\Omega = \frac{1}{2\pi} \int_{\Omega} \left(\sum_m a_m(r, \Omega) \phi_m(r, z, \Omega) \right) e^{j\Omega t} d\Omega. \quad (2.4)$$

Similarly, the inverse Fourier transform of the frequency-dependent mode coefficient $a_m(\Omega)$ in Eq. 2.3 defines the time series associated with mode m at range r :

$$\alpha_m(r, t) = \frac{1}{2\pi} \int_{\Omega} a_m(r, \Omega) e^{j\Omega t} d\Omega. \quad (2.5)$$

Limits of integration in the above equations are determined by the source bandwidth and the frequency range over which the relevant modes are propagating.

The following example illustrates some of the essential characteristics of the nor-

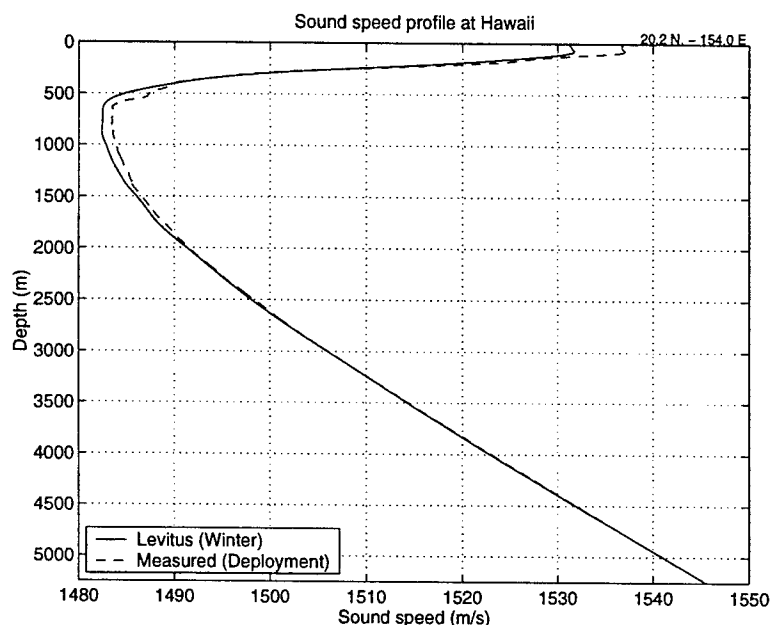


Figure 2-1: Sound speed at the ATOC Hawaii array (20.2°N, -154.0°E). The solid line is the profile obtained using temperature and salinity from the Levitus database for the winter season. The dashed line corresponds to the profile computed from a CTD measurement taken at the time of array deployment (mid-November 1995).

mal modes using the environment at the ATOC Hawaii array. Figure 2-1 shows the sound speed profile for this location, computed from Levitus climatological data [6, 7]. For reference, the plot also includes the profile derived from environmental measurements taken during the array deployment. Figure 2-2 shows the first 10 modeshapes at 75 Hz for both of these environments.¹ Note that each mode samples a different part of the waveguide: the lowest modes are concentrated around the sound channel axis, while the higher order modes cover greater extents of the water column. The modes of these two environments are qualitatively similar, however the shapes do reflect the differences in sound speed (up to 1 m/s near the channel axis).

Since the medium wavenumber depends on frequency as well as sound speed, the modes are functions of frequency, in general. To demonstrate this, Figure 2-3 compares the modeshapes at 60 and 90 Hz for the Levitus environment. The

¹Unless otherwise noted, mode functions are calculated using Baggeroer's Prufer code [8].

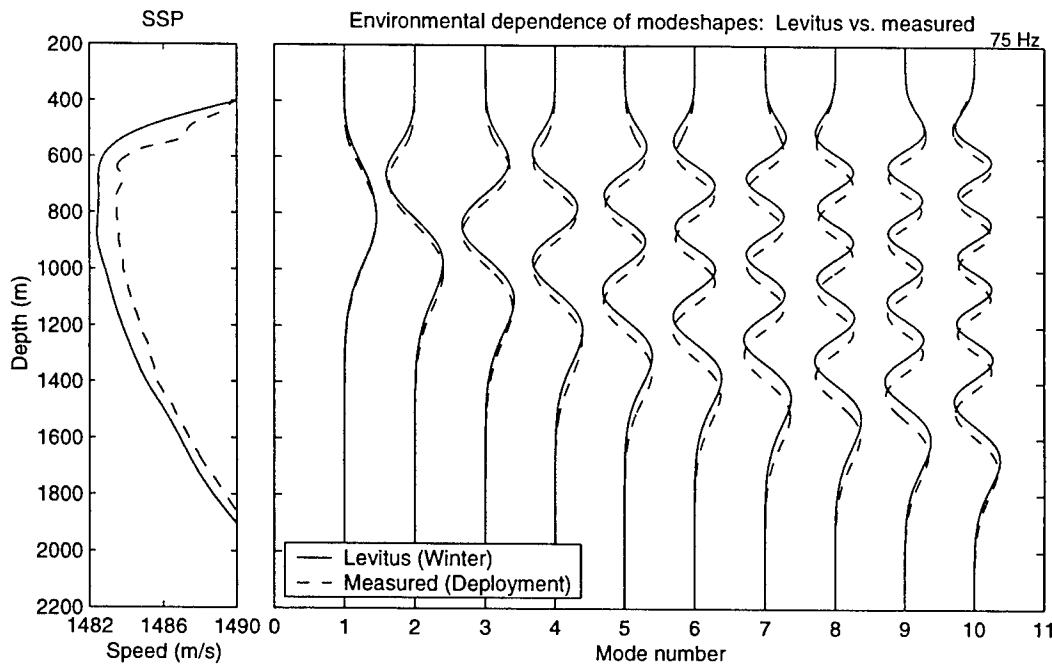


Figure 2-2: Comparison of Levitus environment and measured environment at Hawaii. The left panel shows a closeup of the sound speed profiles around the channel axis. The right panel shows the modeshapes for the first 10 modes at 75 Hz in each environment.

frequency range on the plot corresponds to the approximate bandwidth of the ATOC source. Over this 30 Hz interval, mode 1 varies slightly, whereas mode 10 changes quite significantly. In general, the environment and the source bandwidth determine the extent of modal frequency dependence. As this example clearly shows, modal frequency variations are an important factor to consider in the ATOC experiment.

The formulation in Equations 2.1-2.5 emphasizes that the modes are an orthonormal basis for a particular environment, defined by $c(r, z)$. Based on their spatial distributions, the lowest modes (eigenfunctions) can provide a compact description of acoustic energy concentrated around the sound channel axis. Beyond being useful as a “local” basis set, the modes are interesting because they are strongly connected with the propagation of signals in the ocean waveguide. The following section discusses how modes propagate in a variety of different environments and raises some questions about long-range sound transmissions.

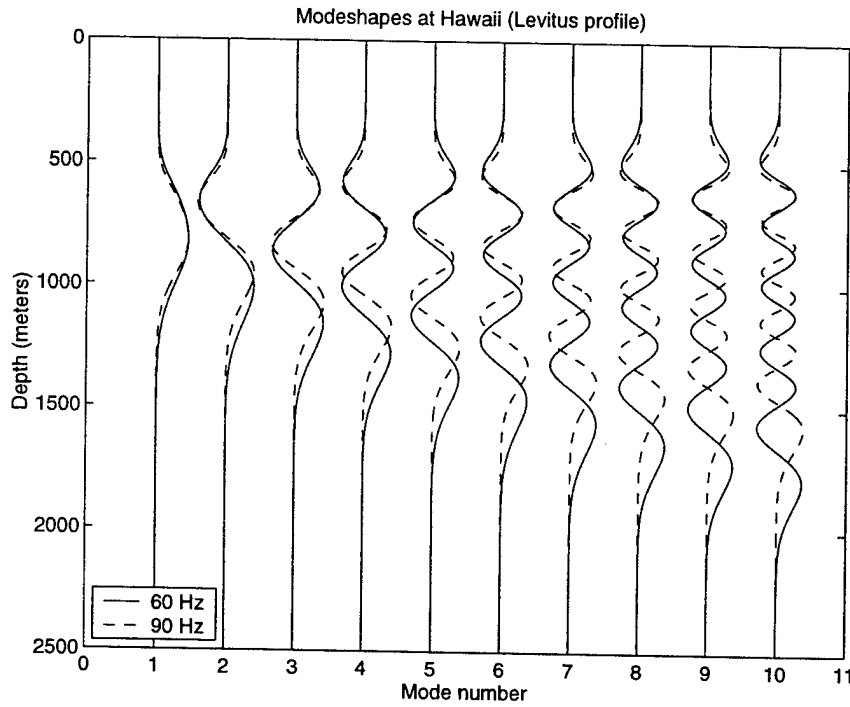


Figure 2-3: Modeshapes for the first 10 modes of the Hawaii-Levitus environment at 60 Hz and 90 Hz. The plot shows the upper 2500 meters of the 5250 meter waveguide.

2.1.2 Mode Propagation

From a simple input/output viewpoint, the underwater channel transforms the mode signals excited by the source into a modal time series at the receiver. Assuming a finite number of propagating modes, a concise frequency-domain description of this system is

$$\mathbf{a}[r, \Omega] = \mathbf{T}[\Omega] \mathbf{a}[0, \Omega] \quad (2.6)$$

where $\mathbf{a}[0, \Omega]$ is a vector of mode amplitudes at the source ($r = 0$) and $\mathbf{a}[r, \Omega]$ represents the corresponding vector at the receiver. For a point source, the modes are excited at levels proportional to the source spectrum S_{src} and the amplitude of the modeshape at the source depth z_s i.e.,

$$\mathbf{a}[0, \Omega] = \frac{S_{\text{src}}[\Omega] \phi_m(r=0, z_s, \Omega)}{\rho(z_s)} \quad (2.7)$$

In Eq. 2.6, $\mathbf{T}[\Omega]$ is a square matrix that defines the transformation of the spectral amplitudes, according to how the modes propagate in the channel. There are two broad classes of propagation environments to consider: range-independent and range-dependent.

Range-Independent Environments

Given a fixed sound speed profile and bottom depth, the modeshapes and wavenumbers are independent of range. In this case, the modes propagate without exchanging energy, *i.e.*, \mathbf{T} is a diagonal matrix:²

$$\mathbf{T}_{\text{RI}}[\Omega] = \frac{e^{j\pi/4}}{\sqrt{8\pi}} \begin{bmatrix} \ddots & & 0 \\ & \frac{e^{jk_m r}}{\sqrt{k_m r}} & \\ 0 & & \ddots \end{bmatrix}. \quad (2.8)$$

In this type of waveguide, each mode is a standing wave in depth that propagates outward from the source with a group velocity equal to $d\Omega/dk_m$. In general, group velocity varies with mode number and frequency, meaning that the channel is dispersive. For a deep water environment, the low modes travel slowest, since they represent energy trapped around the sound speed minimum; higher modes travel faster. In a deep channel, modal group velocity typically decreases with frequency.

Range-Dependent Environments

For realistic ocean waveguides, the environment is a function of range, or more generally, a function of range and azimuth. When the medium is inhomogeneous due to variations in sound speed and/or bathymetry, the modes no longer propagate independently. Instead there is coupling of energy among the modes, meaning that the \mathbf{T} matrix has non-zero off-diagonal terms. A range-dependent waveguide can be mod-

²Eq. 2.8 assumes the receiver is in the farfield of the source. See [4, 5] for a discussion of range-invariant waveguides.

eled using a cascade of range-independent segments. In this type of model, boundary conditions at the segment interfaces determine the mode coupling coefficients.

Since the coupled-mode approach leads to a computationally-intensive implementation, it is useful to consider a simplification. The adiabatic approximation assumes the range dependence is weak and neglects the coupling terms, reducing \mathbf{T} to a diagonal matrix. Under this assumption, each propagating mode adapts with range (changes shape and wavenumber), but does not transfer energy into the other modes. For an adiabatic model the range-averaged wavenumber,

$$\bar{k}_m = \frac{1}{r} \int_0^r k_m(r') dr', \quad (2.9)$$

determines the phase and group speeds for mode m , thus the adiabatic propagation matrix, \mathbf{T}_{AD} , is simply \mathbf{T}_{RI} with k_m replaced by \bar{k}_m . Obviously the validity of the adiabatic assumption is related to the nature of the inhomogeneities in the medium. Desaubies has analyzed this problem in detail, concluding that the approximation's accuracy depends strongly on frequency, mode number, range and the acoustic quantity of interest, *e.g.*, intensity, phase travel time [9, 10].

In long-range experiments, there are several types of inhomogeneities that may cause mode coupling. Consider the environment along the geodesic connecting ATOC source at Pioneer Seamount to the receiving array at Hawaii, shown in Fig. 2-4. The plot shows how the Levitus (winter) sound speed profiles change over the 3515 km path. Variability is concentrated in the upper 500 m of the water column and is a relatively mild function of range. The figure also displays the bathymetry for this section of the ocean. In a deep water environment, changes in the bottom are unlikely to affect the axial modes since they do not interact with the waveguide boundaries. For these modes, the most significant feature of this path is the rapid dropoff in the vicinity of Pioneer Seamount. The bottom-mounted source (935.5 m) does not directly excite the lowest modes. Instead they are excited by energy that couples from the higher order modes as the sound propagates downslope. Chapter 4 explores

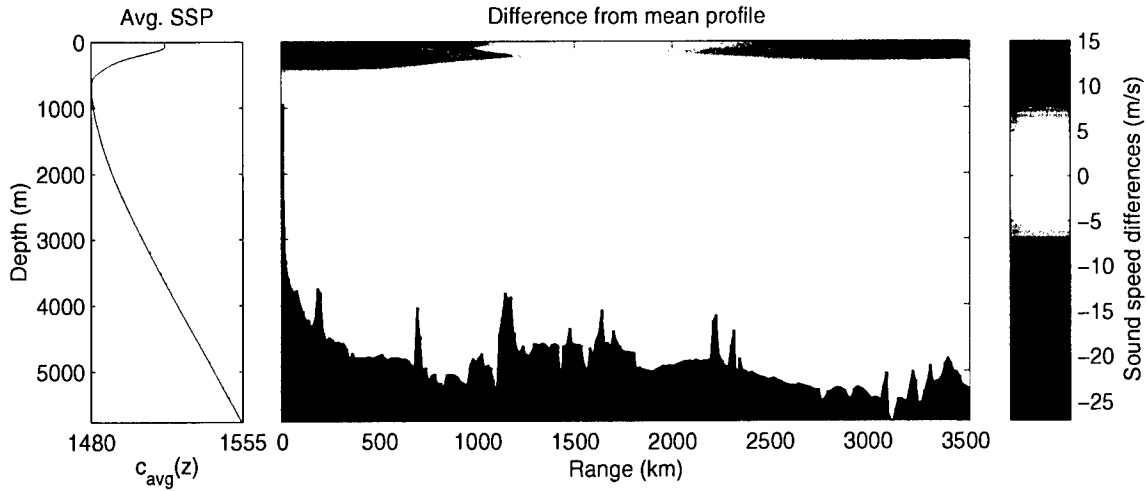


Figure 2-4: ATOC environment: geodesic path between source at Pioneer Seamount (off California) and the receiving array near Hawaii. The left panel is the average sound speed profile over the path, computed using 235 sections (≈ 15 km apart). The right panel shows the differences between the mean profile and the Levitus (winter) profile for each of the sections. Depth of the ocean bottom, shown in black, is taken from bathymetric surveys of Pioneer Seamount [1] and the ETOPO-5 topography database [2].

the issue of bathymetric coupling and its implications for the mode arrivals measured in ATOC.

As indicated in Chapter 1, internal waves are expected to be the primary source of mode coupling in long-range propagation experiments. In the deep ocean, internal wave variability is typically modeled using the empirical Garrett-Munk spectrum [11, 12]. Figure 2-5 shows one realization of sound speed perturbations due to internal wave fluctuations, computed using the method of Colosi and Brown [13]. The calculation assumes the internal waves are $1/2$ Garrett-Munk strength. Note that the variability is greatest in upper part of water column.

Before reviewing what is known about mode propagation through random internal wave fields, it is useful to consider two simulation examples. The first shows how broadband signals propagate through the slowly-range-varying Levitus environment. As a comparison, the second example illustrates the effects of internal waves by adding the sound speed perturbations of Fig. 2-5 to the background environment.

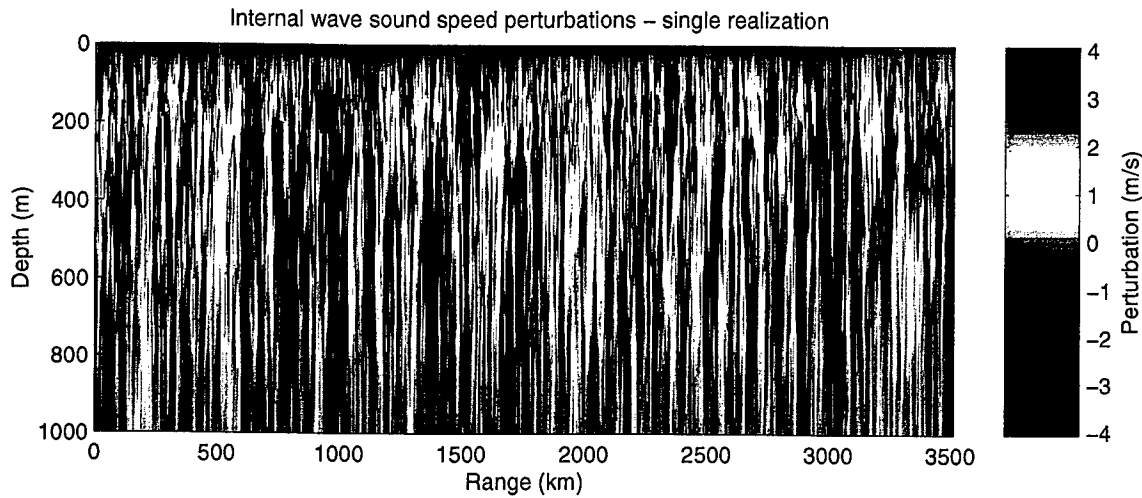


Figure 2-5: Sound speed perturbations due to internal waves at 1/2 Garrett-Munk strength

For simplicity, both simulations use an axial (rather than bottom-mounted) source and ignore the seamount.

To develop some general intuition about propagation in the unperturbed Levitus environment, consider the adiabatic group velocities. Figure 2-6 shows the velocities for the first 40 modes, derived from the average wavenumbers for the 3515 km path. On the plot, the bottom line on the plot corresponds to mode 1 and the top line corresponds to mode 40. Group velocity decreases with frequency and increases as a function of mode number, as is typical in a deep water channel. Figure 2-7 shows the predicted spread of mode arrival times at 3515 km range, assuming a bandlimited source spectrum between 60 and 90 Hz and adiabatic propagation. As expected from the group velocity curves, the high modes arrive first and exhibit the most dispersion, while the low modes arrive last and are less spread. Mode 1 is undispersed since its group speed is approximately constant with respect to frequency.

Figure 2-8 shows the results of a broadband parabolic equation (PE) simulation through the Levitus background environment. The top plot is the pressure time series at the Hawaii array location, calculated using the RAM PE code [14].³ Individual

³Simulations are explained in more detail in Chapter 4.

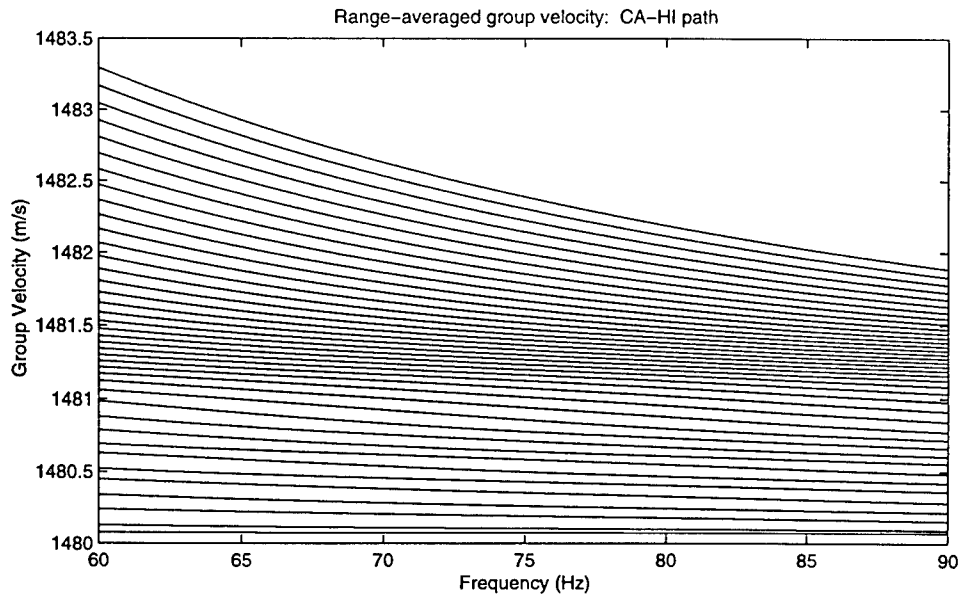


Figure 2-6: Range-averaged group velocities for the first 40 modes of the CA-HI Levitus environment

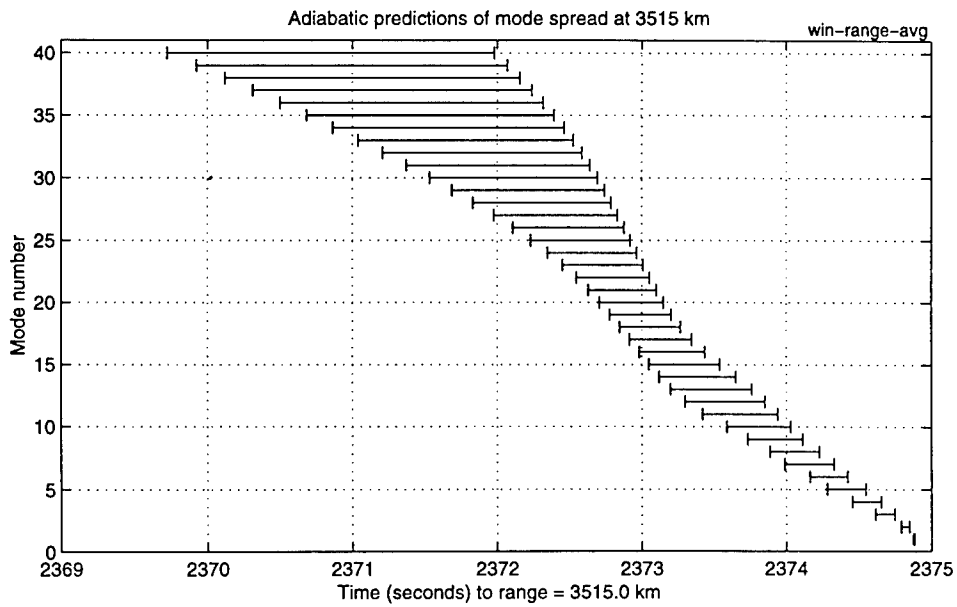


Figure 2-7: Adiabatic predictions of mode time spread due to dispersion

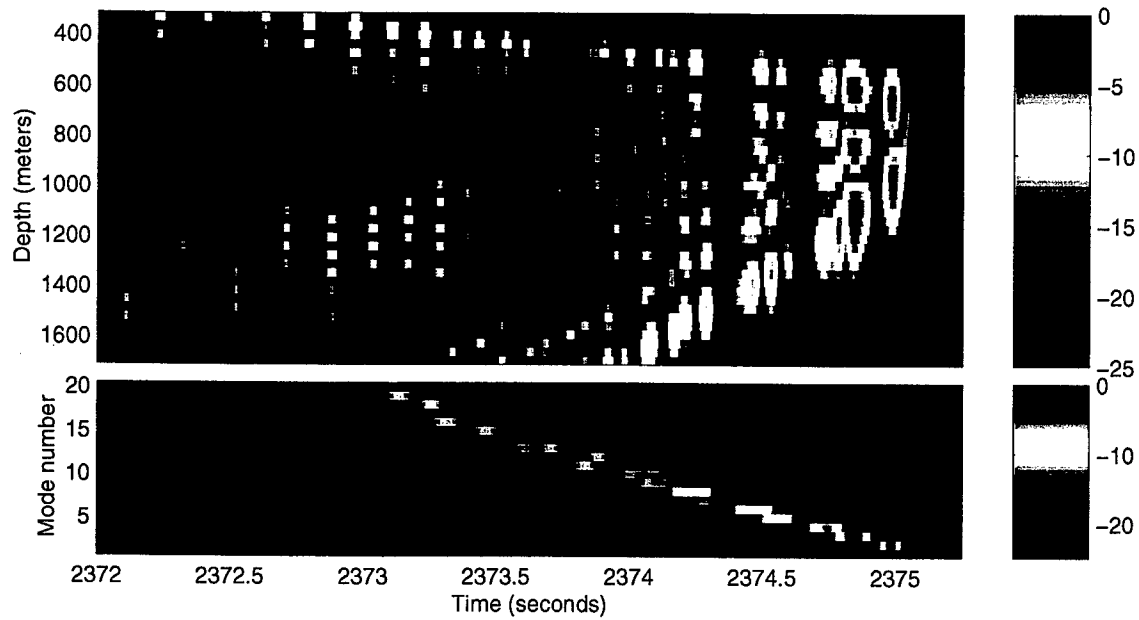


Figure 2-8: PE simulation through Levitus environment. The top panel is the received pressure on a 40-element VLA; the bottom panel shows the corresponding arrival time series in the first 10 modes

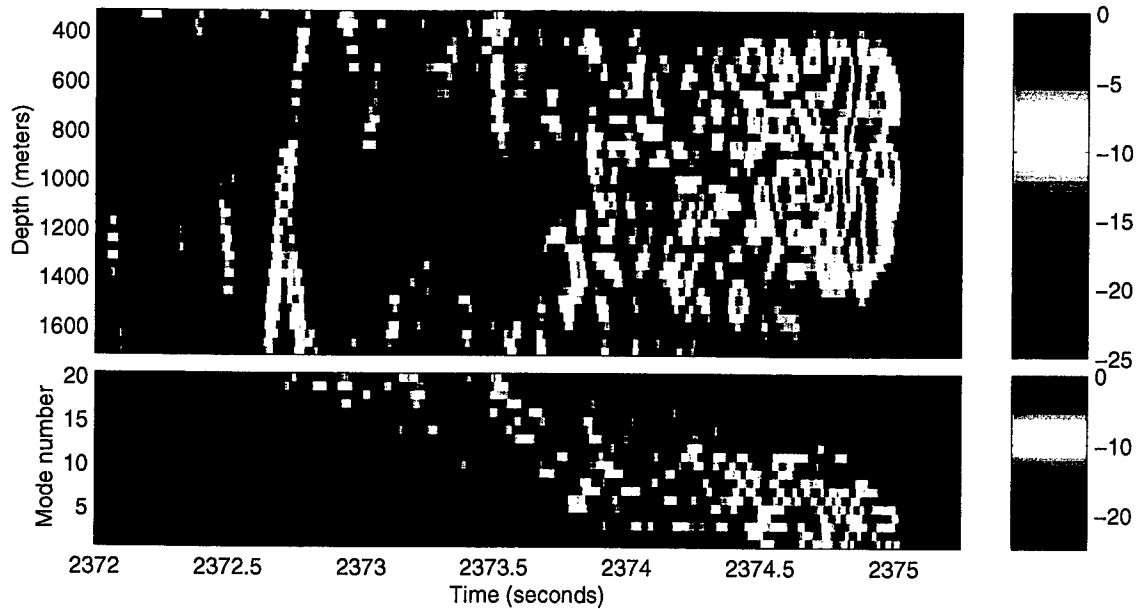


Figure 2-9: PE simulation through Levitus environment plus internal waves

mode arrivals are evident in the pressure field, *e.g.*, modes 5, 3, 1. Below the pressure plot is the modal time series obtained by projecting the PE field onto the functions at the receiver. The modes are obviously arriving in order from highest to lowest. The constructive interference of the higher modes result in the planewave (ray) arrivals in the early part of the reception.⁴ Each of the low modes appears to have a single dominant peak, which arrives at the predicted adiabatic arrival time. This implies that the range variations in the sound speed do not result in mode coupling. Dispersion characteristics of the waveguide are evident.

In contrast, Fig. 2-9 shows the analogous results of the PE simulation for the Levitus environment plus internal waves. The picture is quite different. Individual modes are no longer visible in the pressure time series. From the mode time series, it appears that instead of a single, dispersive arrival in each mode, there are multiple arrivals. This “modal multipath” creates the complicated interference patterns seen in the pressure waveforms. Comparing these two examples to the ATOC reception shown in Fig. 1-2 of Chapter 1 reveals that the experimental measurement more closely resembles the internal wave simulation.

From a theoretical standpoint, the effects of internal waves on long-range sound propagation are not fully understood. Most previous work has focused on the ray arrivals because they are amenable to analysis via the geometric optics approximation. The monograph by Flatte *et al.* summarizes the path integral theory that predicts the fluctuations and coherence of resolved rays [17]. No corresponding theory exists for predicting the behavior of the mode arrivals. The following discussion reviews important results regarding mode propagation through internal waves (but does not attempt a comprehensive overview of work in this area).

In two seminal papers, Dozier and Tappert derive statistics for the modal intensities of narrowband signals propagating in a random ocean [18, 19]. Based on theoretical work and a set of numerical simulations, they conclude that scattering

⁴A number of references explore the ray-mode analogy in detail, *e.g.*, [15, 16, 3].

eventually results in an equipartition of energy among the modes. To make the problem tractable, the authors rely on a number of key assumptions, which may not be valid in real ocean environments. Notably they assume that the acoustic modes are mutually incoherent (phase-random) and that there is no loss of energy into the bottom. Regarding the first assumption, Nechaev has shown that partial coherence of the modes can prevent the equipartition of energy predicted by Dozier and Tappert [20, 21]. Nechaev's analytical results indicate that decorrelation of neighboring modes can occur more slowly than the randomization of the overall field and that scattered modal energy can form a stable interference structure.

A series of papers in the Russian literature have investigated the degradation of mode coherence by internal waves and the resulting implications for various signal processing methods, *e.g.*, matched filtering [22], horizontal array beamforming [23, 24], and vertical array beamforming [25]. Recently, Sazontov has developed an approximate analytic method for computing the modal cross-coherences and using them to calculate the mutual coherence function for the total field [26]. Gorodetskaya *et al.* provide an excellent introduction to this technique, applying it to a study of horizontal and vertical array gain limitations due to internal wave fluctuations [27]. At present, it is not known how well the approximate expressions for coherence agree with experimental data.

Prior to ATOC, there have been very few opportunities to observe the axial arrivals at megameter ranges. Researchers have relied heavily on numerical simulations to test theories about the late-arriving mode energy. In one of the first looks at experimental data, Colosi *et al.* compare pressure measurements from the 1000 km SLICE89 experiment to broadband PE simulations [28]. Their results show that the broadening of the transmission finale in the data is attributable to internal waves. This smearing in depth of the final axial arrivals is due to an exchange of energy among the modes. Colosi and Flatte explore the subject of mode coupling via internal waves using PE simulations designed to model certain aspects of the ATOC experi-

ment [29]. They show that mode propagation through these random fields is strongly non-adiabatic and quantify the travel-time bias/spread and intensity fluctuations for the modes. According to Colosi *et al.*'s recent review article, internal-wave-induced mode coupling, while definitely an issue at 75 Hz, may be significantly reduced at lower frequencies, *e.g.*, 28 Hz [30].

Internal waves can obviously limit the effectiveness of tomographic inversions or MFP applications since it hampers the ability to associate an arrival with a particular path through the ocean. As indicated by this overview, there is much left to learn about broadband mode propagation through internal wave fields. Characterizing the mode arrival structure is a prerequisite to using the modes in tomography or source localization. The ATOC experiment is the first to have mode-resolving arrays deployed to measure axial modes at megameter ranges over a period of months. The following section describes some specific questions that this thesis proposes to explore using the ATOC receptions.

Questions About Long-Range Mode Propagation

This thesis seeks to address the following questions concerning long-range mode propagation. By answering these questions we hope to gain insight into how to identify appropriate observables for tomography and other applications.

First, a general question about axial arrivals at megameter ranges:

- How to characterize the mode arrival structure?
 - is each mode dominated by a single, dispersive arrival?
 - is there multipath?
 - are the dispersion characteristics of the channel evident?
- How do the mode signals vary with time?

The next question requires a different approach than previous researchers have taken, namely it requires short-time frequency decompositions.

- Can the characteristics of individual multipaths within a mode be measured?

How do they compare with the ray arrivals?

- temporal coherence?
- frequency coherence? resolvable multipath?
- fluctuation statistics

- How does the downslope propagation/bottom interaction near the source affect the initial mode excitations. In turn, how does that affect the receptions at megameter ranges?

For an experiment like ATOC where there are many questions about the forward propagation, it is crucial to design a mode estimator that doesn't assume any *a priori* knowledge of the arrival structure and to thoroughly analyze the estimator's behavior. The following section defines the broadband mode estimation problem and identifies the various factors that determine mode resolution.

2.2 Broadband Mode Estimation Problem

In general, the low order modes are not temporally resolvable [31], meaning that they are not directly observable in the time series from a single hydrophone. Instead, vertical arrays can be used to separate the mode signals based on their spatial characteristics. This approach relies heavily on the orthogonality of the sampled modes.

Using Eq. 2.3, the noisy pressure field at frequency Ω , sampled by an N -element vertical array, may be written:

$$\begin{bmatrix} p(r, z_1, \Omega) \\ \vdots \\ p(r, z_N, \Omega) \end{bmatrix} = \begin{bmatrix} \phi_1(r, z_1, \Omega) & \cdots & \phi_M(r, z_1, \Omega) \\ \vdots & & \vdots \\ \phi_1(r, z_N, \Omega) & \cdots & \phi_M(r, z_N, \Omega) \end{bmatrix} \begin{bmatrix} a_1(r, \Omega) \\ \vdots \\ a_M(r, \Omega) \end{bmatrix} + \begin{bmatrix} n(z_1, \Omega) \\ \vdots \\ n(z_N, \Omega) \end{bmatrix} \quad (2.10)$$

or in vector notation:

$$\mathbf{p}[r, \Omega] = \Phi[r, \Omega] \mathbf{a}[r, \Omega] + \mathbf{n}[\Omega]. \quad (2.11)$$

Φ is the matrix of sampled modeshapes, \mathbf{a} is the vector of mode amplitudes, and \mathbf{n} is the vector of observation noise. Eq. 2.10 assumes that the signal consists of M propagating modes. In the case of a broadband source, the array actually measures a vector time series, *i.e.*, from Eq. 2.4,

$$\Psi(r, t) = \int_{\Omega} \mathbf{p}[r, \Omega] e^{j\Omega t} d\Omega = \int_{\Omega} (\Phi[r, \Omega] \mathbf{a}[r, \Omega] + \mathbf{n}[\Omega]) e^{j\Omega t} d\Omega. \quad (2.12)$$

This thesis considers the problem of estimating the mode signals (*i.e.*, $\mathbf{a}[\Omega]$) from noisy measurements of the pressure field. A number of important signal processing issues arise in designing broadband mode estimators. The rest of this section discusses these issues in detail, using the ATOC experiment as the motivating example.

Modal frequency dependence is the most important issue to consider in broadband mode estimation. As Fig. 2-3 demonstrates, modeshapes can vary significantly across a 30 Hz source band. Clearly, spatial processing must be done on a set of subbands to avoid mismatch problems. Since a combination of temporal and spatial filtering is required, there are time/frequency tradeoffs to make. Good time resolution is desirable for resolving the individual multipaths within a mode. The allowable widths of the subbands is determined by the environment, *i.e.*, the modeshape variations.

On a band-by-band basis, mode estimation reduces to a classic linear inverse problem, discussed in many areas of the literature, *e.g.*, estimation theory [32], geophysical inverse theory [33]. In the narrowband mode estimation problem, the key issue to consider is the degrees of freedom of the sampled modeshape matrix. This determines how well the processor can resolve a mode and reject noise. From the point of view of estimating one mode, there are two types of noise to consider. The first component consists of signals propagating in the other modes - this is structured interference and may be correlated with this signal. The second is measurement noise

that uncorrelated with the signal, *e.g.*, shipping noise, sensor noise. Note that in terms of interference rejection, we assume that some time windowing can be done to limit the number of modes contained in the measurement, *i.e.*, the ray arrivals (high order modes) can be ignored by time-gating.

In addition to time/frequency tradeoffs and degrees of freedom concerns, two other issues arise in implementing mode estimators for realistic experiments. The first concerns arrays that are not perfectly vertical. This can be modeled by using a complex modeshape matrix - the phase terms represent the timing corrections required for each mode. In planewave beamforming, this is known as the array transit time problem. It is important to quantify the limitations it places on the processor for modes. Usually, reliable mooring motion estimates are available, so the problem is one of correcting for known delays.

A second practical concern relates to the dependence of the mode on the local environment at the array. Mode environmental dependence is the key to using them in tomography or matched field processing, but can be a hindrance when the receiver environment is not exactly known. Uncertainty in our knowledge of $\Phi[\Omega]$ affects ability to resolve the mode signals accurately. Consider the measured and archival profiles shown in Fig. 2-2. In this case, the archival profile does not adequately represent the modes of the measured environment. In ATOC the problem is that we only have two measurements of the environment: one at deployment and one at recovery. The time lapse between those two is approximately 9 months. It is expected that mesoscale effects and seasonal changes affect the profile over the course of the experiment, so that there may be mismatch between the modes of the measured profile and the true profile. It is important to quantify the effects of mismatch on mode processing.

In summary, there are a number of important design considerations in broadband mode estimation. The following section reviews relevant literature on mode filtering techniques and their application to tomography, focusing in particular on how

researchers have approached the design issues outlined above.

2.3 Previous Work

Most previous research has focused on experimental settings where a narrowband assumption is valid, meaning that either the source is continuous wave (CW) or the variations in the mode functions across the source band are negligible. In that context, Ferris and Ingenito describe the first use of vertical arrays for studying mode propagation in a real ocean environment [34, 35]. Their experiment consists of transmitting gated sinusoidal pulses in a shallow water channel to receivers at ranges on the order of 10 km from the source. They examine the mode structure of the arriving signals using both a temporal filtering method, which takes advantage of the differences in modal group velocities, and a spatial filtering method, which relies on the the orthogonality of the sampled modeshapes. For the latter, the authors use a filter matched to the modeshapes at the center frequency of the transmitted pulse. It is easy to show that the matched filter (sometimes called the sampled modeshapes filter) is the optimal linear mode filter for detecting/estimating any single mode in a background of spatially white noise [32]. The main problem with this filter is that it typically has poor interference rejection capabilities because it requires the orthogonality of the modes to separate them. While the modes are orthogonal functions over the continuous aperture, the modeshapes, as sampled by the array, may not be.

A solution to the problem of modal crosstalk is to use a least squares approach to solve the mode estimation problem. Tindle *et al.* are the first to introduce this method in the context of the underwater acoustics [36]. In this case, the mode filter is the pseudo-inverse of the sampled modeshape matrix. The primary advantage of this filter is that the weight vector for a particular mode has nulls in the directions of the other modes included in the estimate. Tindle *et al.* do note the connection

of least squares mode estimation and beamforming, but do not explore this idea in detail.

Polcari explores some of the tradeoffs of single beam vs. multiple beam mode filters in his study of mode coherence in the Arctic Ocean [37]. In addition to the least squares formulation, he considers a maximum likelihood method that uses estimates of the spatial covariance matrix (requiring that the signal be stationary over sufficiently long intervals). Polcari also discusses how to choose the number of modes to include in multiple mode estimators.

The pseudo-inverse filter is now a standard in the acoustic community, as indicated by its use in a number of matched mode processing applications [38, 39, 40]. The difficulty with this LS approach is that the pseudo-inverse may be poorly-conditioned. This is a common problem in inverse theory [33]. A number of authors have considered it specifically in the context of mode processing. Yang suggests using rank-reduced singular value decompositions to solve for the mode amplitudes [41]. Voronovich *et al.* review a number of standard approaches to solving this problem, but do not offer specific recommendations about which to use [42]. Buck *et al.* present a unified framework for the narrowband mode estimation problem [43] and use it to analyze the performance of several common mode filters. In particular, they discuss the sampled modeshapes filter and the pseudo-inverse filter in terms of tradeoffs in interference rejection and noise rejection. They develop a maximum *a posteriori* mode filter which gracefully transitions between these two extremes. Note that the MAP approach uses knowledge of the signal and noise covariance matrices; estimating these quantities typically requires some assumptions about signal stationarity.

There are numerous examples of narrowband mode processing being applied to experimental data. In the context of long-range propagation, there are two experiments of note: the Heard Island Feasibility Test (HIFT) and the Trans-Arctic Propagation (TAP) experiment. Baggeroer *et al.* discuss the use of least squares

modal filtering in the context of HIFT, which used a narrowband source operating at 57 Hz and transmitted across a 17,000 km path to a vertical array [44]. The failure of a large number of hydrophones made the modal estimation for HIFT significantly more difficult. Sperry considers this problem in detail and implements a damped least squares filter in order to perform the inversion [45]. He discusses in some detail how to choose the number of modes to include in the estimate based on how well the array samples the water column. The recent TAP experiment examined mode arrivals at megameter ranges in the Arctic [46]. Both CW and maximal-length sequences were used. Narrowband processing could be used for the latter because the modes did not vary significantly across the frequency band of the source (centered at 19.6 Hz).

In cases where modal frequency variations are non-negligible, researchers have generally approached the problem by using an FFT to separate the signal into frequency bins, doing mode processing for each bin, and obtaining a time series via inverse FFT. In one shallow water experiment, Chen and Lu use bandpass filters to facilitate mode processing for an explosive source [47]. They process the data in bands where the modeshapes may be assumed constant, but do not offer criteria for choosing the width or center frequencies of these bands. Numerous authors, including Romm [48], Yang [49], Casey [50] and Chiu *et al.* [51], have implemented broadband mode estimators using FFT's. Since they compute a single transform for each receiver's time series, their method does not provide a frequency vs. time decomposition of the modal structure. None of these researchers have discussed how the frequency resolution imposed by the length of the FFT affects the estimates. Sutton *et al.* have suggested using a combination of time-windowing and Fourier transform-based mode filtering to resolve modes using a sparse array [52]. Their article does not present the details of time windowing or explore the implications of window length on estimator resolution. Heaney has used a time-windowing approach as well for an analysis of the ATOC Engineering test data [53, 54]. His windows for the FFT are on the order

of 3-4 seconds long, meaning that he is not able to look at the behavior of individual multipaths in the Fourier decomposition. Heaney uses mode filtering as a part of matched field inversions for source location and internal wave strength. He does not study the mode arrival structure in great detail.

Another issue that needs to be considered in broadband mode estimation is environmental mismatch. While mismatch problems in general have been thoroughly investigated in the context of matched field processing applications (see [55] for an overview), there has been little attention focused on modal mismatch due to changes in the sound speed profile. Tolstoy considers the effects of sound speed mismatch on matched field localization using a normal mode model, but does not discuss the effects on the individual mode coefficients [56].

Although Munk and Wunsch first suggested using modes for tomography in 1979 [57] and expanded upon the theory in 1983 [16], most experimental applications of tomography have been based on ray theory. A ray is the result of the coherent interference of a set of higher order modes. The rays form a stable arrival structure that is well-suited to analysis via planewave beamforming techniques. See the recent book by Munk *et al.* for more information [15]. By comparison the mode tomography literature is somewhat limited. The following paragraphs summarize the relevant publications.

Romm's Ph.D. thesis investigates using modal group velocity perturbations in tomographic inversions for sound speed profile [48]. He uses basic linear inverse theory to derive the relationship between mode group speeds and sound speed. Simulations for a Greenland Sea environment are used to illustrate the usefulness of mode tomography. Romm briefly discusses the required acoustic signal processing, but his mode filtering techniques are quite limited and poorly explained.

Shang has developed a full-wave method for ocean acoustic tomography using adiabatic normal mode theory and low frequency sources [58]. He describes how to invert for the sound speed profile by using modal phase difference perturbations

for CW sources and modal travel time perturbations for broadband sources. Shang assumes that these perturbations can be measured using array processing algorithms or by using temporal separation to localize the pulse arrivals based on the time series from a single hydrophone. He does not comment on how well the modes must be resolved in order for the tomographic inversion to be successful. The paper includes a simulation which demonstrates the feasibility of the inversion but does not involve any acoustic array processing.

In a recent set of papers, Shang and Wang have applied matched mode processing techniques to the tomographic inversion of an El Niño profile [59, 60]. They base their simulation on measured sound speed profiles from an actual El Niño event, but the travel time perturbations used in the example are theoretical values. This research largely ignores the practical issues involved in estimating the mode arrival times. The authors do indicate a way to compute the resolution of the time delay estimate. Their measure of resolution comes from computing the Cramer-Rao bound for the problem. It is unclear whether this bound can be achieved with a practical system operating in a range-dependent ocean environment.

The paper by Sutton *et al.* is the only experiment to date where mode time delays have been incorporated into a tomographic inverse [52]. They used a broadband source with center frequency of 250 Hz and transmitted across a 106 km path in the Greenland Sea. The vertical receiving array was sparse, consisting of only 6 elements. The authors use a least squares method along with some time-windowing to determine the mode waveforms.

Based on this review, there is much to be done yet on broadband mode estimation. Specifically, none of the broadband mode processing schemes proposed thus far have addressed the fundamental question of what frequency resolution is required for accurate mode estimation. One purpose of this thesis is to develop and analyze a general framework for broadband mode processing.

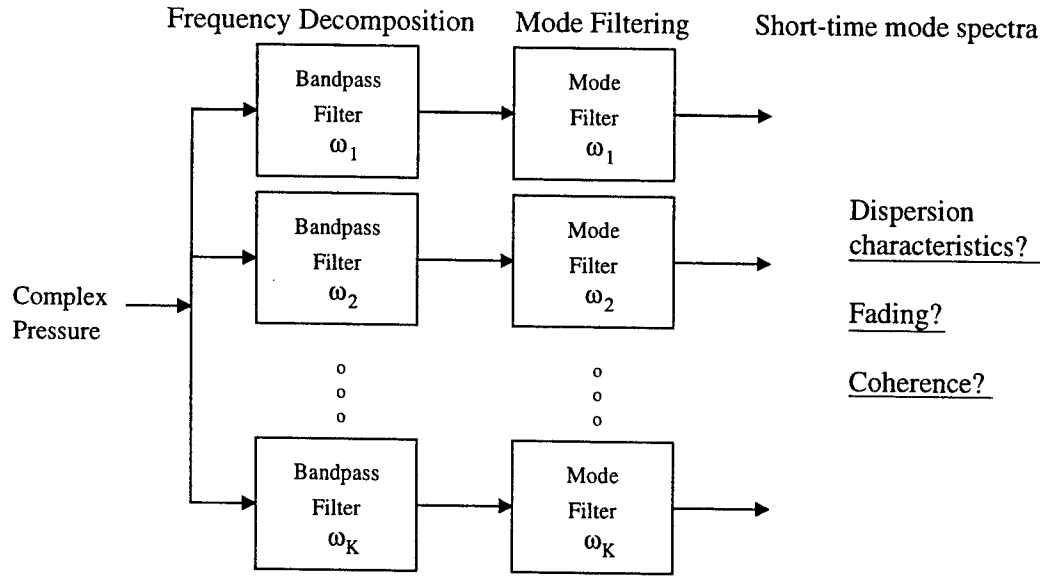


Figure 2-10: Proposed short-time Fourier mode processing framework

2.4 Approach

From the overview of previous work, it is clear that no one has quantified the time/frequency resolution attainable in mode estimation. To address these issues, this thesis proposes to develop the short-time Fourier mode processing framework shown in Fig. 2-10. The basic idea is to separate the pressure signals into a set of subbands using a filterbank and then do mode processing in each subband. The output is a time series of mode amplitudes (time-varying spectra) that can be used to examine the frequency-dependent structure in the signals, *e.g.*, to quantify dispersion or look for frequency-selective fading.

This method has several advantages. First, it allows us to examine the multiple arrivals within a single mode individually, rather than combining them by using a large FFT for the required frequency decomposition. This permits looking for frequency-coherent arrivals within the multipath arrival pattern and studying the fluctuation characteristics of a single arrival within in a mode rather than just studying the fluctuations of the entire mode signal. Note that the bandpass filtering effectively limits the number of modes that are present at each time step; this is a

generalization of the time-windowing approach proposed by others. Finally, it is important to note that all the previously-described methods fit within this framework.

The following chapter develops the short-time Fourier mode processing framework and explores the temporal and spatial resolution tradeoffs. It also discusses some implementation issues related to non-vertical arrays and environmental uncertainty. Chapter 4 applies the short-time Fourier techniques to the ATOC data set.

Chapter 3

Short-time Fourier Mode Processing

As Chapter 2 demonstrates, modal variations across frequency often require that spatial processing be done on a set of sub-bands to avoid modeshape mismatch problems. The purpose of this chapter is to present a framework for broadband mode estimation and to explore the time/frequency resolution tradeoffs inherent in the processing of transient mode signals. From a signal processing perspective, the short-time Fourier transform (STFT) is a natural way to approach the frequency decomposition required in mode estimation. The STFT provides a general framework for analyzing the time- and frequency-domain properties of modal beamforming algorithms. A significant advantage to this approach is that all the broadband mode processing methods described in the previous chapter (Section 2.3) fit conveniently within the basic STFT structure.

The discussion of short-time Fourier mode processing is organized as follows. Section 3.1 gives an overview of short-time Fourier mode processing and indicates some of the important design tradeoffs. Following that, Section 3.2 derives equations for the processor and analyzes performance using the ATOC experiment as a design example. Section 3.3 demonstrates STFT-based mode processing for a simple

adiabatic propagation environment. Analysis of the adiabatic case provides useful insights about the short-time estimates. Building on that example, Section 3.4 derives the mooring corrections required for tilted arrays. Section 3.5 briefly discusses the impact of environmental uncertainty on the STFT mode processor. Finally, Section 3.6 summarizes the key results of this chapter.

3.1 Overview of the STFT Framework

The STFT is a standard signal processing technique for examining the characteristics of transient or time-varying signals. Short-time Fourier *analysis* consists of computing discrete Fourier transforms for a sequence of finite-length data segments. There are two equally-valid interpretations of the resulting time-dependent spectrum: 1) as the output of a filterbank, or 2) as the output of a windowed FFT operation. Short-time Fourier *synthesis* is the process of reconstructing a signal from its time-varying spectral components. Allen and Rabiner [61] and Nawab and Quatieri [62] provide an excellent general introduction to the STFT; other authors concentrate on specific applications. For example, Rabiner and Schafer [63] discuss the short-time Fourier method in the context of speech processing, and Johnson and Dudgeon [64] describe how it applies to planewave beamforming. In the latter case, the STFT provides a convenient framework for separating a multichannel signal into subbands prior to spatial filtering. Similarly, the short-time Fourier transform is a useful way to formulate the frequency decomposition required in broadband mode estimation.

In STFT-based mode analysis, the processor separates the received pressure into a set of subbands and computes mode estimates for each subband. Figure 3-1 illustrates these steps and introduces some notation. The input to the filterbank is $\Psi[l]$, a sampled vector time series from an N -element receiving array. As shown, the filtering operation consists of complex demodulation followed by lowpass filtering; this is equivalent to bandpass filtering followed by demodulation. The result of the STFT

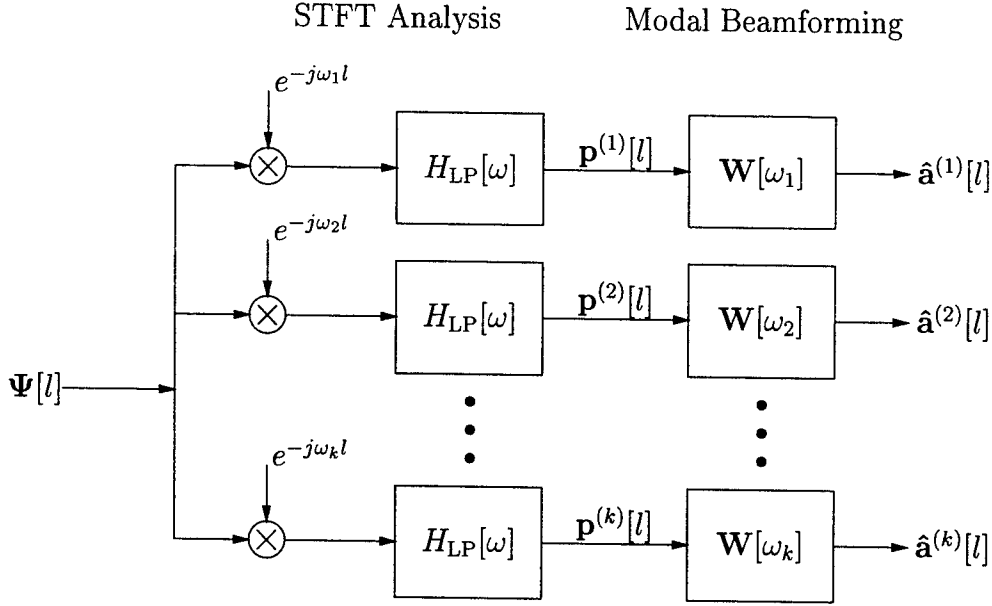


Figure 3-1: Block diagram of STFT-based mode processor

analysis step is an N -point complex vector time series of pressures for each band: $\mathbf{p}^{(k)}[l]$, where k denotes the band (bin) number and l is the time index. Using a set of narrowband modal beamformers, the processor computes the time-varying mode coefficients from the filtered pressures in each band. The M -point vector $\hat{\mathbf{a}}^{(k)}[l]$ is the estimated short-time Fourier transform of the first M modes in the bin centered around ω_k .

Within the STFT framework, the length of the lowpass filter, $H_{LP}[\omega]$, determines the time and frequency resolution of the estimates. In the context of mode processing, there are important filter length tradeoffs to consider. Long filters (equivalent to taking large FFT's) have good frequency resolution, implying small operating bandwidths for the spatial filter $\mathbf{W}[\omega_k]$. The disadvantage of long filters is that they smear the arrivals in time. Short filters provide much better temporal resolution, but they have wider passbands, meaning that the processor may be more sensitive to the frequency-dependent variations of the modes.

3.2 Mode Processing With Vertical Arrays

As outlined above, the short-time Fourier approach to mode processing is conceptually simple: separate the signal into subbands and estimate the mode signals in each subband using a narrowband spatial filter. This section describes the implementation of the STFT framework for a perfectly vertical array (*i.e.*, no tilt) in a known environment. A subsequent section discusses the corrections that are necessary for tilted arrays (3.4).

3.2.1 Broadband Processor Derivation

The purpose of deriving equations for the STFT processor is to facilitate a broadband performance analysis in terms of the time/frequency tradeoffs and other criteria established in Section 2.2. This derivation uses discrete-time (DT) representations, where l is the time index and ω is the DT frequency variable. To simplify notation, the mode parameters (shapes and wavenumbers) are written as functions of ω ; more precisely, they are functions of the corresponding analog frequency $\Omega = \omega \cdot f_s$, where f_s is the sample frequency.

Analogous to Eq. 2.12, the sampled time series of received pressures at a vertical array can be written using a discrete Fourier transform (DFT) representation, *i.e.*, the I -point DFT:

$$\Psi[l] = \frac{1}{I} \sum_i \mathbf{p}[\omega_i] e^{j\omega_i l} \quad \omega_i = \frac{2\pi i}{I} \quad i = 0, \dots, I-1. \quad (3.1)$$

To avoid complications, I must be large enough to represent the entire reception (including high order mode arrivals) and the subsequent filtering operations without time aliasing. For convenience, the following derivation assumes that the DFT length corresponds to the number of time samples recorded for each reception.

The first step in processing is complex demodulation, shown in Fig. 3-1 as multiplication by $e^{-j\omega_k l}$. After an appropriate change of variables, the demodulated

pressure in the k th bin can be written

$$\Psi_{\text{demod}}[l] = \frac{1}{I} \sum_i \mathbf{p}[\omega_k + \omega_i] e^{j\omega_i l}. \quad (3.2)$$

Note that Equation 3.2 assumes that the demodulation time reference is the first sample of the reception ($l = 0$). Choosing a different reference point simply introduces an additional complex exponential term. The demodulation reference is important because the phase of the short-time Fourier mode estimates depends on it.

Following demodulation the processor lowpass-filters each bin, resulting in

$$\mathbf{p}^{(k)}[l] = \frac{1}{I} \sum_i H_{\text{LP}}[\omega_i] \mathbf{p}[\omega_k + \omega_i] e^{j\omega_i l}. \quad (3.3)$$

Based on the development in Chapter 2, the received pressure at a particular frequency consists of a finite sum of modes plus noise, *i.e.*,

$$\mathbf{p}[\omega] = \Phi[\omega] \mathbf{a}[\omega] + \mathbf{n}[\omega]. \quad (3.4)$$

Φ represents the matrix of sampled modeshapes at the receiver, \mathbf{a} is the vector of frequency-dependent mode amplitudes, and \mathbf{n} is the noise vector.

Substituting this representation for the received pressure into Eq. 3.3 yields

$$\mathbf{p}^{(k)}[l] = \frac{1}{I} \sum_i H_{\text{LP}}[\omega_i] \Phi[\omega_k + \omega_i] \mathbf{a}[\omega_k + \omega_i] e^{j\omega_i l} + \frac{1}{I} \sum_i H_{\text{LP}}[\omega_i] \mathbf{n}[\omega_k + \omega_i] e^{j\omega_i l}. \quad (3.5)$$

In the above equation, the first summation is the filtered signal component of the pressure field; the second summation is the filtered noise component. Assuming that the modeshapes are approximately constant over the bandwidth of the lowpass filter:

$$\Phi[\omega_k + \omega_i] \approx \Phi[\omega_k], \quad (3.6)$$

then the measured pressure in the k th band becomes

$$\mathbf{p}^{(k)}[l] = \Phi[\omega_k] \mathbf{a}^{(k)}[l] + \mathbf{n}^{(k)}[l] \quad (3.7)$$

where

$$\mathbf{a}^{(k)}[l] = \frac{1}{I} \sum_i H_{\text{LP}}[\omega_i] \mathbf{a}[\omega_k + \omega_i] e^{j\omega_i l}, \quad (3.8)$$

$$\mathbf{n}^{(k)}[l] = \frac{1}{I} \sum_i H_{\text{LP}}[\omega_i] \mathbf{n}[\omega_k + \omega_i] e^{j\omega_i l} \quad (3.9)$$

are the bandpass-filtered (and demodulated) modal signal and noise components, respectively. In this type of mode filtering, the goal is to estimate the time-varying mode coefficients $\mathbf{a}^{(k)}[l]$ from the noisy pressure measurements $\mathbf{p}^{(k)}[l]$ for each bin.

3.2.2 Narrowband Mode Filters

Essentially, the STFT approach reduces the broadband mode estimation problem to a set of narrowband problems where the measurement takes the form of Eq. 3.7. Based on that equation, narrowband mode filtering is equivalent to determining the parameters of a linear model. This type of estimation problem is quite common, and there are a number of available techniques for solving it, *e.g.*, least squares methods or Wiener filtering. Selection of a particular approach strongly depends on what is known or can be reasonably assumed about the signal and noise characteristics. The following paragraph states the assumptions this thesis makes in designing a bank of narrowband mode processors for the ATOC data.

The filtered pressures are complex envelopes, resulting from the demodulation of real bandpass signals. Both the mode signals, $\mathbf{a}^{(k)}[l]$, and the noise, $\mathbf{n}^{(k)}[l]$, are complex time series. This thesis assumes that the noise is a zero-mean vector random process, independent of the mode signals. Unlike the noise, very little is assumed about the modal time series. Since the purpose of this research is to study the low

mode arrivals at megameter ranges, it is important to avoid biasing those results by assuming a particular temporal or spatial structure for these signals. Specifically, this means that the processor developed below does not rely on adiabatic predictions of travel time or dispersion characteristics to estimate the modes. Furthermore, this thesis does not consider time- or data-adaptive processing methods that require temporal and/or spatial statistics. Such statistics are not available *a priori* and cannot be reliably estimated from the data until more is known about the underlying signals, *e.g.*, their stationarity, *etc.*. Although adaptive algorithms are beyond the scope of this work, they are reasonable extensions to explore once more is known about long-range mode propagation.

Since time-adaption is not an option for the ATOC data, it makes sense to estimate the modes independently at each time step and to use the same mode filter for all time steps. This thesis focuses on estimates of the form

$$\hat{\mathbf{a}}^{(k)}[l] = \mathbf{W}_k^H \mathbf{p}^{(k)}[l] \quad (3.10)$$

where \mathbf{W}_k^H is an $M \times N$ matrix containing the time-invariant mode filter for the k th band. Equation 3.10 assumes that the estimated mode coefficients are linear combinations of the received pressures. This assumption is not very restrictive since linear filters represent a large subclass of solutions. Most narrowband acoustic mode filtering algorithms described in the literature (see Section 2.3) can be written in this form. For the purpose of designing the spatial filter, \mathbf{W}_k , this thesis assumes that the matrix of sampled modeshapes at the receiver (Φ) is known exactly. This is equivalent to assuming that accurate measurements of the sound speed profile at the receiver are available. Section 3.5 examines the impact of violating this assumption.

In designing the spatial processing for the low-modes, this thesis considers two standard narrowband mode filters: the matched (sampled modeshapes) filter and the pseudo-inverse (least squares) filter. There are a number of ways to derive these filters. This chapter approaches the problem from an array processing standpoint,

which emphasizes some of the implicit assumptions being made about the underlying spatial structure. The derivations below provide a complimentary perspective to the estimation theory approach to mode filtering that is commonly used in the literature (see [43] for a summary).

An important concept in these derivations is the array gain, which represents the improvement in the signal-to-noise ratio (SNR) due to processing. It is typically defined as the ratio of the SNR at the output of a beamformer to the SNR at a single sensor. Since the signal and noise characteristics often vary across an array, the input SNR is taken to be the arithmetic average of the single-phone SNR's:¹

$$\text{SNR}_{\text{in}} = \frac{1}{N} \sum_{n=1}^N \frac{(\text{signal power})_n}{(\text{noise power})_n}. \quad (3.11)$$

Note that in the case of modal beamforming, the signal levels vary from one sensor to another because the modes shapes are functions of depth.

White noise gain represents the gain of the processor when the noise is spatially white. For the mode processing problem, the white noise gain in mode m is defined as

$$G_w = N \frac{|\mathbf{w}_m^H \boldsymbol{\phi}_m|^2}{\mathbf{w}_m^H \mathbf{w}_m \boldsymbol{\phi}_m^H \boldsymbol{\phi}_m}, \quad (3.12)$$

where \mathbf{w}_m is the weight vector (filter) for the m th mode. Application of the Schwartz inequality shows that the maximum value of the white noise gain is N , the number of sensors in the array. Even if the noise isn't spatially white, the white noise gain provides a useful measure of the sensitivity of the processor, as discussed by Cox *et al.* [65].

Matched (Sampled Modeshapes) Filter

The matched filter (MF) results from choosing the weight vector for mode m which maximizes white noise gain while maintaining a unit gain in the desired mode. Max-

¹The geometric average is used in some applications.

imizing white noise gain subject to a unity gain constraint is mathematically equivalent to minimizing the squared length of the weight vector subject to the same gain constraint, thus the optimization problem becomes

$$\min \mathbf{w}_m^H \mathbf{w}_m \quad \text{subject to} \quad \mathbf{w}_m^H \boldsymbol{\phi}_m = 1. \quad (3.13)$$

Standard optimization techniques yield the following solution:

$$\mathbf{w}_m^H = \frac{1}{\boldsymbol{\phi}_m^H \boldsymbol{\phi}_m} \boldsymbol{\phi}_m^H, \quad (3.14)$$

or in terms of the weight matrix for M modes

$$\mathbf{W}^H = \begin{bmatrix} \frac{1}{\boldsymbol{\phi}_1^H \boldsymbol{\phi}_1} & & 0 \\ & \ddots & \\ 0 & & \frac{1}{\boldsymbol{\phi}_M^H \boldsymbol{\phi}_M} \end{bmatrix} \mathbf{E}^H \quad (3.15)$$

where \mathbf{E} is the sampled modeshape matrix containing the first M modes, *i.e.*, the first M columns of $\boldsymbol{\Phi}$. Matched filters are commonly used in detection/estimation problems and their behavior is well-understood. It is clear from equations 3.12 and 3.14 that the matched filter achieves the maximum possible white noise gain for an array of a given length N . Although this filter is optimal in the sense that it maximizes G_w , it does not explicitly prevent the signal in one mode from leaking into another. Instead, it must rely on the orthogonality of the modes to separate them. It is important to note that while the modeshapes are orthogonal functions of the continuous variable z , the sampled modeshape vectors are not guaranteed to have this property. The degree of orthogonality of the sampled modeshapes determines the crosstalk rejection capabilities of the matched filter.

Pseudo-inverse (Least Squares) Filter

The pseudo-inverse (PI) filter results from trying to constrain mode leakage by placing nulls in the modal beampattern at the locations of a set of interfering modes. In this case, the optimization problem consists of maximizing the white noise gain (minimizing the weight vector length) subject to multiple constraints, *i.e.*,

$$\min \mathbf{w}_m^H \mathbf{w}_m \quad \text{subject to} \quad \begin{aligned} \mathbf{w}_m^H \boldsymbol{\phi}_m &= 1, \\ \mathbf{w}_m^H \boldsymbol{\phi}_{n \neq m} &= 0 \quad 1 \leq n \leq M. \end{aligned} \quad (3.16)$$

It is useful to rewrite the problem

$$\min \mathbf{w}_m^H \mathbf{w}_m \quad \text{subject to} \quad \mathbf{w}_m^H \mathbf{E} = \mathbf{c}_m^T = [0 \quad \cdots \quad 0 \quad \underbrace{1}_{m\text{th position}} \quad 0 \quad \cdots \quad 0] \quad (3.17)$$

where \mathbf{E} contains the first M columns of the sampled modeshape matrix and \mathbf{c} is an M -point column vector with a one in the m th position and zeros everywhere else. Equation 3.17 can be solved using standard optimization methods involving LaGrange multipliers. Assuming that the matrix \mathbf{E} has rank M , the weight vector for the m th mode is

$$\mathbf{w}_m^H = \mathbf{c}_m^T (\mathbf{E}^H \mathbf{E})^{-1} \mathbf{E}^H. \quad (3.18)$$

Equation 3.18 corresponds to one row of the pseudo-inverse of the the sampled modeshapes matrix containing the first M modes, thus \mathbf{W}^H is simply

$$\mathbf{W}^H = (\mathbf{E}^H \mathbf{E})^{-1} \mathbf{E}^H. \quad (3.19)$$

Provided that the matrix \mathbf{E} , which contains a subset of the sampled modeshapes, has rank M , the $M - 1$ null constraints are met exactly. If \mathbf{E} has rank less than M , a minimum norm solution of the constraint equation is required. The minimum norm solution involves the generalized inverse of \mathbf{E} (typically written in terms of the singular value decomposition).

Another way to derive the pseudo-inverse mode filter is to solve a least squares problem, *i.e.*, to estimate for \mathbf{a} by minimizing the quantity $|\mathbf{p} - \mathbf{E}\mathbf{a}|^2$. This approach is the most common in the underwater acoustics literature. The advantage to viewing mode filtering as a constrained beamforming problem is that the desired spatial characteristics must be explicitly stated and that white noise gain provides a useful measure of the price paid for nulls in the spatial response. White noise gain of the PI filter for the m th mode is

$$G_{w-PI} = \frac{N}{\boldsymbol{\phi}_m^H \boldsymbol{\phi}_m} \cdot \frac{1}{\mathbf{c}_m^T (\mathbf{E}^H \mathbf{E})^{-1} \mathbf{c}_m} \quad (3.20)$$

From this expression, it is clear that the white noise gain of the PI filter is intimately connected with the conditioning of the pseudo-inverse. The term second term is bounded by the squared singular values of the \mathbf{E} matrix:

$$\sigma_{\min}^2 \leq \frac{1}{\mathbf{c}^T (\mathbf{E}^H \mathbf{E})^{-1} \mathbf{c}} \leq \sigma_{\max}^2 \quad (3.21)$$

where σ_{\min} and σ_{\max} are the minimum and maximum singular values of \mathbf{E} , respectively. The white noise gain of the PI filter less than or equal to that of the matched filter (which achieves the maximum possible G_w).

Conditioning problems are well known in both least squares problems and in adaptive filtering. Menke discusses methods of dealing with poorly-conditioned pseudo-inverses in the context of inverse theory [33]. Cox provides a nice discussion of robustness issues in the context of adaptive beamforming [65]. There are many ways of dealing with this problem. Cox provides some time-adaptive approaches (which are not appropriate for the ATOC data due to the transient nature of the signals). Non-adaptive solutions to conditioning problems typically involving deleting small singular values from the inverse, or added a small weight to the diagonal terms of $\mathbf{E}^H \mathbf{E}$ before inverting it in order to stabilize the inversion. Both these methods bias the results and should be used with care (especially when not much is known/understood

about the arrival structure).

Thus far, this section has derived equations for the STFT processor, showing how it reduces the broadband mode estimation problem to a set of narrowband problems. Two approaches to narrowband filtering have been discussed. The following subsections explore narrowband and broadband performance issues, using a design example based on the ATOC experiment.

ATOC Design Example

Numerical results presented below use the Levitus environment for the California-Hawaii path, described in Chapter 2. Note that although the archival sound speed differs from the measured profile at the array (see Fig. 2-1), these differences do not affect the basic conclusions regarding the number of modes that can be reliably estimated, the allowable bandwidth, *etc.* The array in the example corresponds to the ATOC VLA configuration: 40 elements, with a spacing of 35 m, spanning the water column between 330 m and 1695 m. For reference, Fig. 3-2 shows the hydrophone locations relative to the first 20 modes at 75 Hz for the Hawaii-Levitus environment. 75 Hz is the center frequency for the ATOC source, which has approximately a 30 Hz bandwidth (from 60-90 Hz). The sample rate for the experiment is 300 Hz.

3.2.3 Narrowband Performance Analysis

The main purpose of this section is to compare the matched filter and the pseudo-inverse narrowband beamformers, focusing primarily on the tradeoffs in noise and interference rejection. Beampatterns provide a useful measure of the crosstalk rejection capabilities of a spatial processor. In the context of modal beamforming, the beampattern is defined as $20 \log_{10}(\mathbf{W}^H \Phi)$, where \mathbf{W} is the multidimensional mode filter and Φ is the matrix of sampled modeshapes. The m th row of the beampattern matrix corresponds to the projection of the modes into the estimate for mode m .

For the matched filter, the beampattern corresponds to a normalized version of

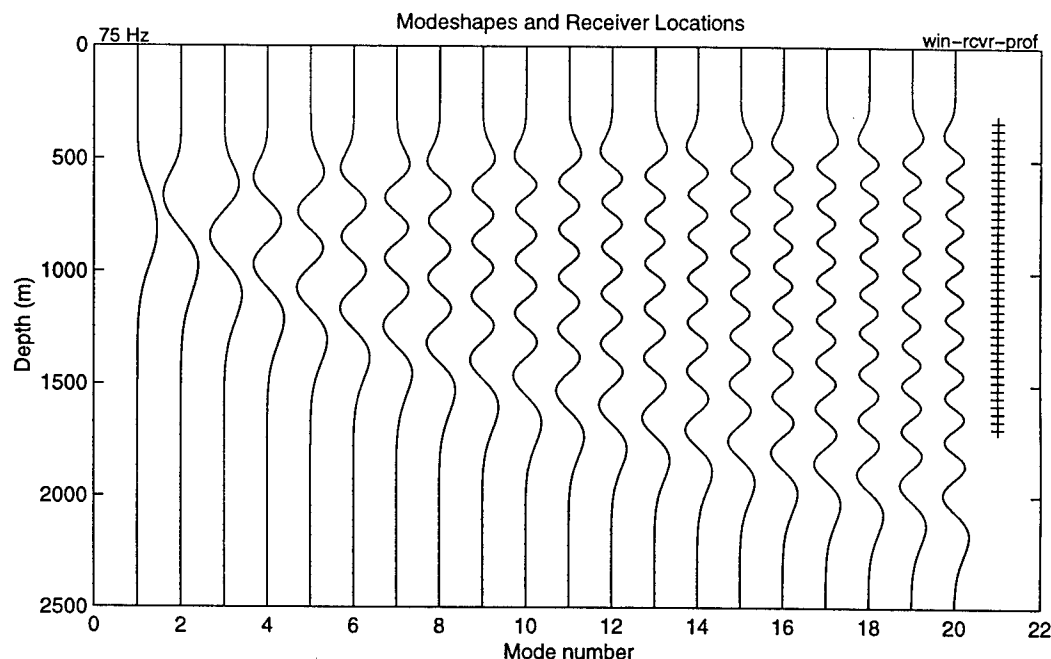


Figure 3-2: Modeshapes (75 Hz) and receiver locations (+’s) for the design example

the sampled modeshape correlation matrix, $\Phi^H \Phi$. Figure 3-3 shows MF beampattern for the first 40 modes, using the ATOC array at Hawaii. This beamformer has excellent crosstalk rejection for the lowest modes, up until approximately mode 8. Above that, the modeshapes sampled by the array are obviously correlated. As a result, energy from one mode will leak into its neighbors. Performance of this beamformer degrades significantly for modes above 10; this is not surprising since the array is designed to sample the first 10 modes.

Figure 3-4 shows the beampatterns for three different pseudo-inverse filters, designed for 10 modes, 15 modes, and 20 modes, respectively. Note that the Fig. 3-4(c) has a different dB scale than figures 3-4(a) and 3-4(b). By design, the PI filter guarantees nulls for a specified set of modes, thus the beampatterns have a diagonal structure. It is important to remember that while the PI filter guarantees a fixed set of nulls, it does nothing to prevent higher order modes not included in the pseudo-inverse from leaking into the lower order modes. The beampatterns show how the higher order modes (up to 40) not included in the pseudo-inverse alias into the lower

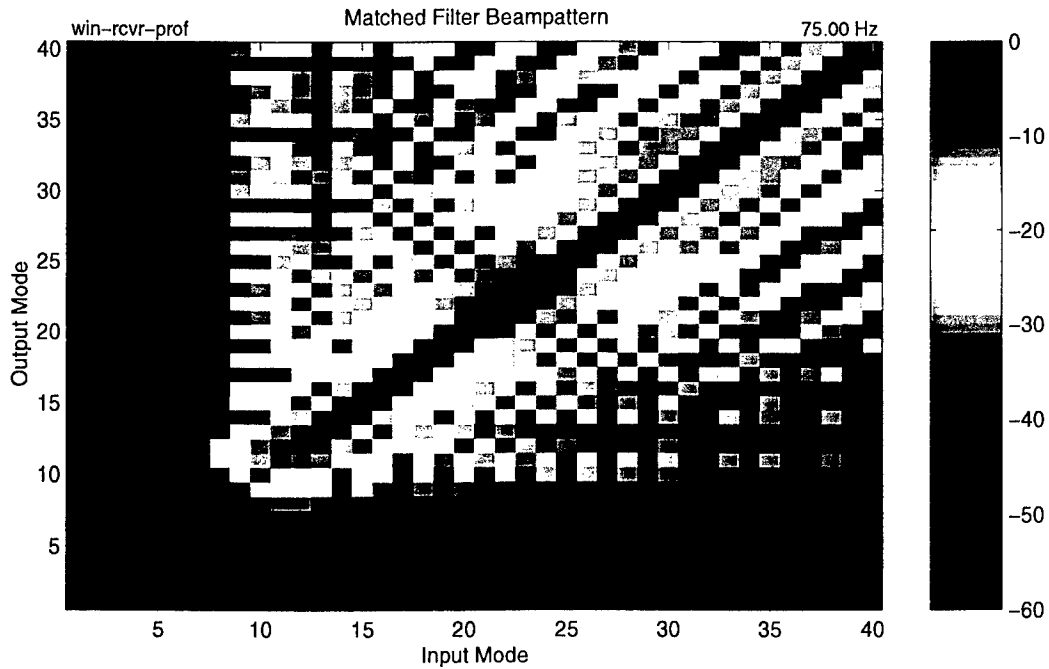
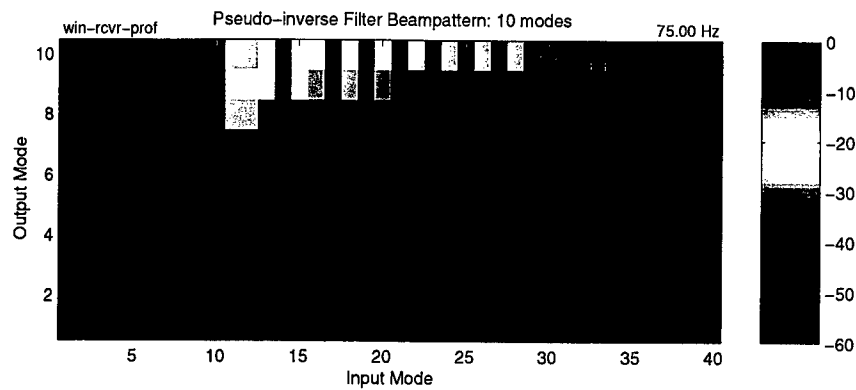


Figure 3-3: MF Beampattern (75 Hz) for the 40-element ATOC VLA in the Hawaii-Levitus environment

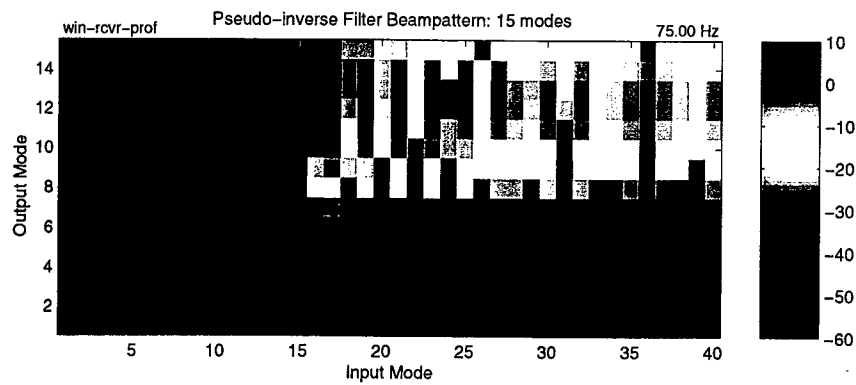
modes.

The price paid for the nulls in the PI beampattern is a loss in white noise gain. Figure 3-5 shows the white noise gain as a function of mode number for the 10-, 15-, and 20-mode filters. The dotted line shows the maximum white noise gain, $10 \log_{10}(N)$, which is achieved by the matched filter. For the 10-mode PI filter, the white noise gain is equivalent to the matched filter results. The 15- and 20-mode PI filters show the loss in white noise gain associated with poor conditioning of the pseudo-inverse. For the 20-mode filter, the white noise gain is negative for some modes meaning that the noise will be significantly amplified compared to the signal.

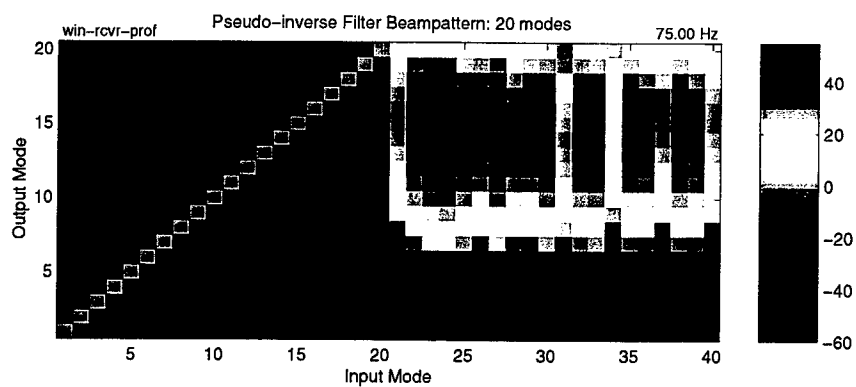
The amount of crosstalk is also governed by the conditioning of the pseudoinverse, *i.e.*, crosstalk increases as the conditioning degrades. This is important because, while it may be possible to assume that the time-windowing imposed by the lowpass filter operation in the STFT processor eliminates the highest modes (earliest ray arrivals), the potential for internal-wave-induced mode scattering means that there



(a) 10-mode PI filter



(b) 15-mode PI filter



(c) 20-mode PI filter; note the different dB scale.

Figure 3-4: Comparison of pseudo-inverse filter beampatterns (75 Hz) for the ATOC array in the Hawaii-Levitus environment

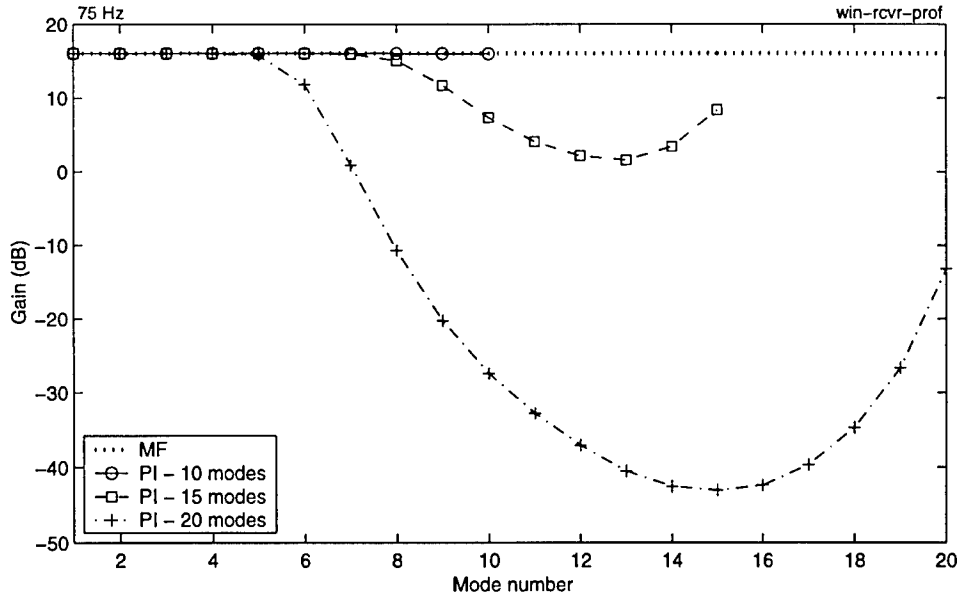


Figure 3-5: White noise gain at 75 Hz for the ATOC array in the Hawaii-Levitus environment

may be a large number of modes within the time window spanned by the temporal filter. As Fig 3-4(c) shows, the crosstalk from higher order modes dominates the estimate for the 20-mode filter, as a result of poor matrix conditioning. Figure 3-6 is a plot of the maximum crosstalk as a function of the number of modes considered. The x-value represents the highest mode considered and the y-value represents the peak crosstalk into that set of modes. For example, the leftmost point on the plot represents how much crosstalk there is into mode 1 from all the other modes up to mode 40. This plot illustrates how using the PI strategy of placing nulls at neighboring modes in order to eliminate crosstalk is a losing game when there are a large number of modes propagating in the waveguide. As the number of constraints increases, so does the length of the weight vector, meaning that modes still not included in the estimate are amplified even more.

It is interesting to note that the degradation in conditioning of the pseudo-inverse exhibited in the 20-mode filter is not significant enough for a matrix inversion program (such as the one used by Matlab) to give a warning about conditioning. From

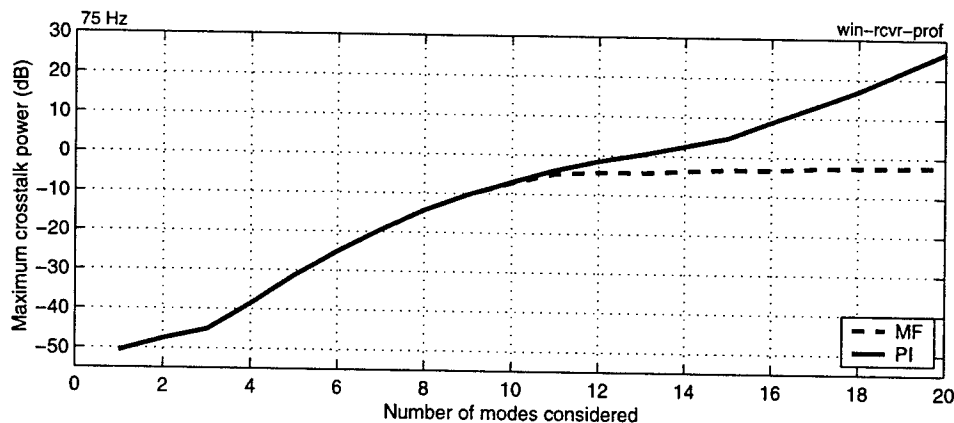


Figure 3-6: Maximum crosstalk

a numerical perspective, the inverse can still be computed without errors, but from an array processing perspective, performance is significantly degraded. If there were no noise in the reception, then the mode estimates could be computed effectively, even with this type of poorly conditioned pseudo-inverse. Obviously, assuming the absence of noise is unrealistic for any experiment. There are ways of mitigating conditioning problems, but only at the expense of biasing the estimates.

This section has shown how modeshape orthogonality affects the matched filter results, how the PI filter null placement strategy can eliminate some of the crosstalk problems but at the expense of robustness. It has been shown that noise and crosstalk from higher order modes both increase as the pseudo-inverse becomes ill-conditioned. Based on the numerical examples, it is clear that the PI filter for 10 modes gives noise gain results equal to that of the matched filter while providing the added benefit of eliminating the crosstalk among modes 8 through 10 which is present in the matched filter. In terms of the ATOC experiment, the PI-10 filter is a reasonable choice for the best narrowband performance. The following section explores broadband performance issues.

3.2.4 Broadband Performance Analysis

In designing a short-time Fourier mode processor, it is crucial to have a measure of how well a narrowband mode filter designed for frequency ω performs on the modes at a neighboring frequency, $\omega \pm \Delta\omega$. Essentially, the operating bandwidth determines the required frequency resolution of the lowpass filter, which in turn defines the temporal resolution of the STFT processor. This section explores these broadband performance issues. First, it examines the frequency response of both the MF and PI mode filters, using the ATOC design example. Based on these results, it is possible to select an appropriate lowpass filter/data window for the STFT. Using that selection, we discuss the time resolution of the STFT processor for the ATOC example. Finally, this section considers the noise response as a function of frequency. This is important because it gives a measure of the conditioning of the mode filter across the source band (allows us to explore how the conditioning of the mode filter is affected by the changes in the modeshapes across frequency).

Frequency Resolution

Consider the signal component of the mode estimate (combining equations 3.10 and 3.5):

$$\hat{\mathbf{a}}^{(k)}[l] = \mathbf{W}_k^H \left(\frac{1}{I} \sum_i H_{LP}[\omega_i] \Phi[\omega_k + \omega_i] \mathbf{a}[\omega_k + \omega_i] e^{j\omega_i l} \right) \quad (3.22)$$

Based on this equation, the frequency response of the STFT processor is primarily governed by the matrix $\mathbf{W}_k^H \Phi[\omega_k + \omega_i]$, which represents the frequency-dependent beampattern of the mode filter \mathbf{W}_k . Figures 3-7 and 3-8 show plots of these beampatterns for the matched filter and the pseudo-inverse filter. Both filters are designed using the Hawaii-Levitus environment modeshapes at 75 Hz; the PI filter is designed for 10 modes. Results are shown for the 30 Hz (± 15 Hz) band around the center frequency. In these figures, each subplot corresponds to the beampattern for a single mode. The solid line represents the response in the desired mode and the dashed

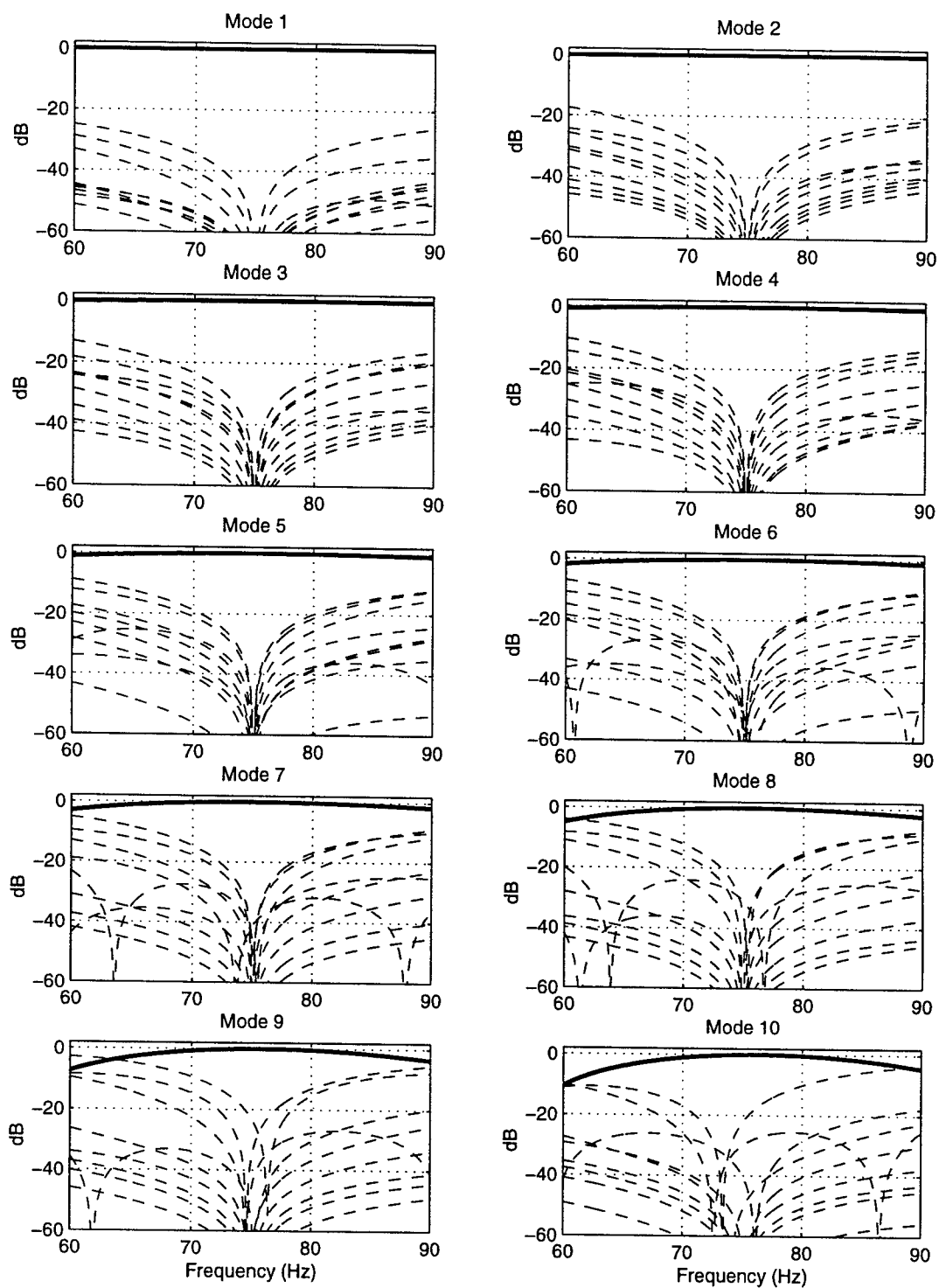


Figure 3-7: Frequency response of the matched filter. Solid lines indicate the response in the desired mode; dashed lines indicate crosstalk from neighboring modes (up to 10).

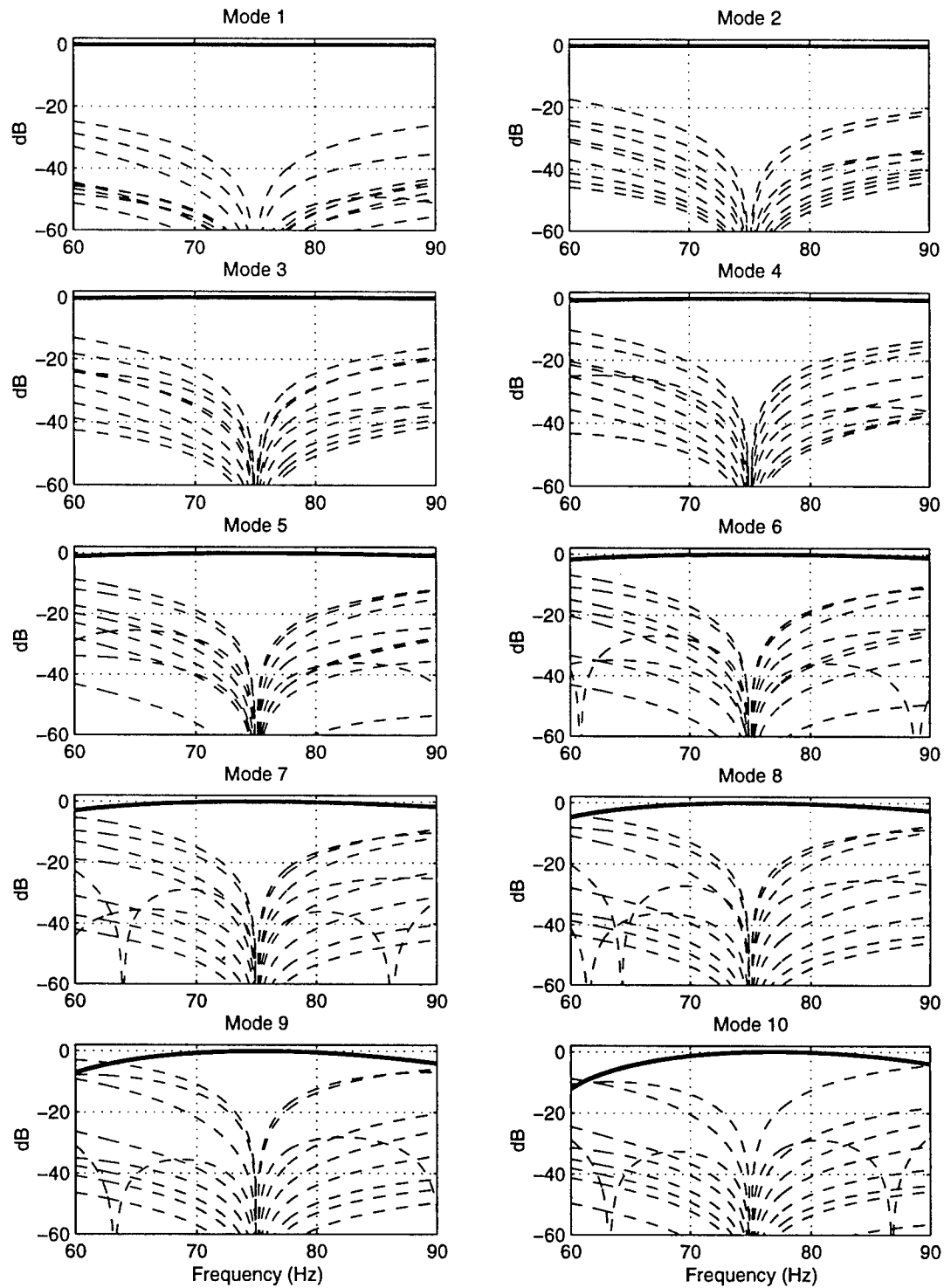


Figure 3-8: Frequency response of the PI filter designed for 10 modes. Solid lines indicate the response in the desired mode; dashed lines indicate crosstalk from neighboring modes (up to 10).

lines represent the crosstalk from neighboring modes (from 1 to 10) into the desired mode.

First consider the matched filter results for mode 1. The beamformer has a flat response for this mode across the 30 Hz band. There are nulls in the direction of the other modes at the center frequency, but crosstalk increases sharply as ω deviates from the design frequency (75 Hz in this case). Plots for the higher modes indicate that frequency mismatch can significantly affect the gain in the desired mode as well as the crosstalk rejection, *e.g.*, the gain in mode 10 is down by 10 dB at 60 Hz. As expected from the narrowband analysis, Fig. 3-7 also shows that the MF beamformer does not prevent crosstalk at the center frequency in modes 8 through 10. The beampatterns for the PI mode filter in Fig. 3-8 show similar behavior. Each filter is constrained at 75 Hz to have unity gain in the desired mode and nulls at the other modes, but these constraints are not guaranteed to be maintained for other frequencies.

Both the MF and PI beampatterns indicate that crosstalk rejection is more significantly affected by frequency mismatch than is the gain in the desired mode. Further insight into this observation is obtained by considering a perturbation theory analysis of the modeshapes as a function of frequency. Appendix A discusses the application of perturbation theory to the mode eigenvalue problem in general and presents the frequency perturbation analysis upon which the results below depend. The basic idea is that the modeshape at frequency $\omega + \Delta\omega$ can be represented as the sum of the modeshape at frequency ω plus first- and second-order correction terms:

$$\phi_m[\omega + \Delta\omega] \approx \phi_m[\omega] + \left(\frac{\Delta\omega}{\omega}\right) \Phi \mathbf{g}_m^{(1)} + \left(\frac{\Delta\omega}{\omega}\right)^2 \Phi \mathbf{g}_m^{(2)} \quad (3.23)$$

where Φ is the matrix of sampled modeshapes at frequency ω and $\mathbf{g}_m^{(1)}$ and $\mathbf{g}_m^{(2)}$ are column vectors containing the first- and second-order perturbation coefficients. As Eq. 3.23 indicates, the correction terms are written in terms of the modes themselves, since they form a complete orthonormal basis. In general, the perturbation of mode

m due to a change in frequency is well-represented by a small set of mode m 's nearest neighbors, thus only a few coefficients in the \mathbf{g} vectors are important.

Using the perturbation expansion, first consider the response in the desired mode *i.e.*,

$$\mathbf{w}_m^H \boldsymbol{\phi}_m[\omega + \Delta\omega] \approx \mathbf{w}_m^H \boldsymbol{\phi}_m[\omega] + \left(\frac{\Delta\omega}{\omega}\right) \mathbf{w}_m^H \boldsymbol{\Phi} \mathbf{g}_m^{(1)} + \left(\frac{\Delta\omega}{\omega}\right)^2 \mathbf{w}_m^H \boldsymbol{\Phi} \mathbf{g}_m^{(2)} \quad (3.24)$$

where the dependence of the weight vector on ω has been suppressed. Assuming that the weight vector effectively passes only the desired mode at the center frequency (a reasonable assumption for a well-conditioned PI filter), then this expression reduces to

$$\mathbf{w}_m^H \boldsymbol{\phi}_m[\omega + \Delta\omega] \approx 1 + \left(\frac{\Delta\omega}{\omega}\right) g_{mm}^{(1)} + \left(\frac{\Delta\omega}{\omega}\right)^2 g_{mm}^{(2)} \quad (3.25)$$

where $g_{mm}^{(1)}$ and $g_{mm}^{(2)}$ represent the amount of $\boldsymbol{\phi}_m$ contained in the first- and second-order perturbations of $\boldsymbol{\phi}_m$. As derived in Appendix A, $g_{mm}^{(1)}$ is equal to 0, and $g_{mm}^{(2)}$ is negative. Thus the loss in the gain of the desired mode is a second-order effect. Similarly, looking at the crosstalk factor shows that

$$\mathbf{w}_m^H \boldsymbol{\phi}_k[\omega + \Delta\omega] \approx 0 + \left(\frac{\Delta\omega}{\omega}\right) g_{km}^{(1)} + \left(\frac{\Delta\omega}{\omega}\right)^2 g_{km}^{(2)} \quad (3.26)$$

In this case, $g_{km}^{(1)}$ is not generally equal to zero, thus the crosstalk terms go as $\frac{\Delta\omega}{\omega}$.

Perturbation theory results can be used to obtain approximate bandwidths for mode filters. In practice, it is often just as easy to plot the response and choose the bandwidth based on that rather than an approximation. Figure 3-9 is a closeup of the frequency response of the 10-mode PI filter. From this figure, it is clear that the crosstalk stays 20 dB down for frequencies within 2.5 Hz of the center frequency. This seems like a reasonable 3 dB bandwidth to choose for the lowpass filter. Based on the perturbation theory analysis, the crosstalk sidelobes increase at a rate of 20 dB per decade, thus it is useful to select a lowpass filter whose sidelobes fall off faster

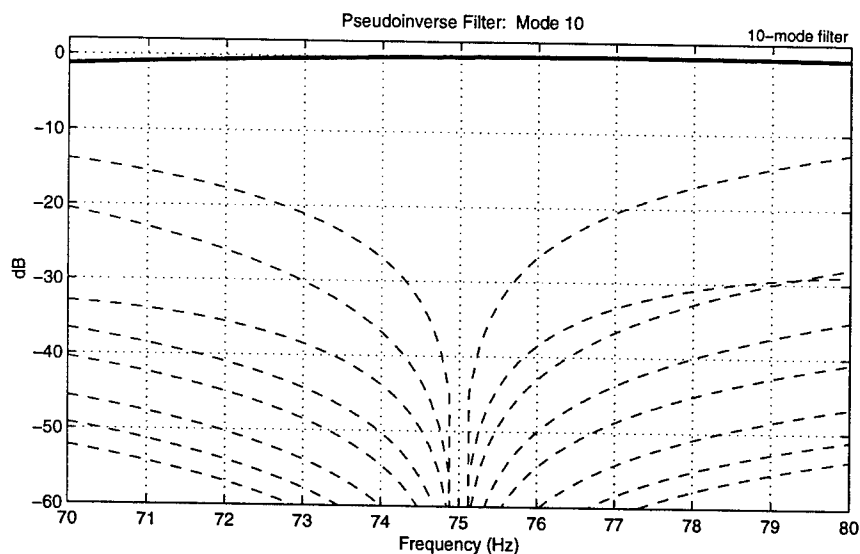


Figure 3-9: Frequency response of the PI filter for mode 10 (designed using 10 modes)

than 20 dB per decade.

Although H_{LP} can be any filter with a lowpass characteristic, short-time Fourier analysis typically employs the same set of windows that is used in spectral estimation [66]. Harris provides an extensive list of window functions in his classic paper [67]. As argued above, the ATOC data requires a filter with approximately a 5 Hz (± 2.5 Hz) bandwidth with sidelobes that fall off at a rate greater than 20 dB per decade. Consider the Hanning window, which has sidelobes that fall off at 60 dB per decade (in terms of the power metric, $20 \log_{10} |H_{LP}|$). Figure 3-10 shows the impulse and frequency responses for Hanning windows of three different lengths, 60 points, 120 points, and 240 points, assuming the ATOC sample rate of 300 Hz. From this plot it appears that an 0.4 second (120-pt) Hanning window gives the desired bandwidth and sidelobe characteristics. It provides adequate suppression of mode crosstalk for modes up to 10. This choice of filter defines the time resolution of the processor. The following section discusses the temporal response of the STFT processor.

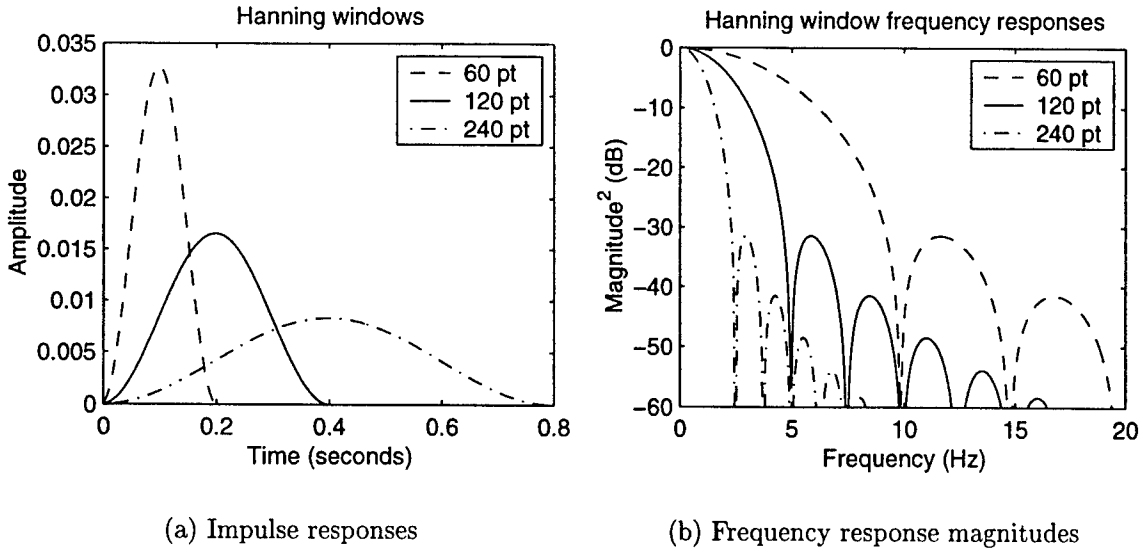


Figure 3-10: Time and frequency responses for three Hanning windows, assuming a 300 Hz sample rate. Amplitude differences among the impulse responses are a result of constraining the response to be equal to 1 at 0 Hz.

Time Resolution

To understand the time resolution of the bandpass-filtered mode estimates, it is useful to determine the minimum separation between two arrivals such that they are resolvable as individual peaks at the output of the filter. For simplicity, suppose the input signal consists of two equal-amplitude impulses, then the output is the sum of two filter impulse responses. Figure 3-11 depicts the result of this superposition for two different assumptions about the spacing of the impulses. A reasonable criterion for resolving the arrivals is that the response at the midpoint between them is smaller than the response at the peak locations. This is true provided that the input separation is greater than the “3 dB timewidth” of the window, *i.e.*, the width between the points where the window amplitude is equal to 1/2 of its peak. For a Hanning window, the 3 dB timewidth is equal to $L/(2f_s)$ where L is the number of points and f_s is the sampling frequency. This definition of temporal resolution is obviously oversimplified, in particular because the effects of noise have been ignored.

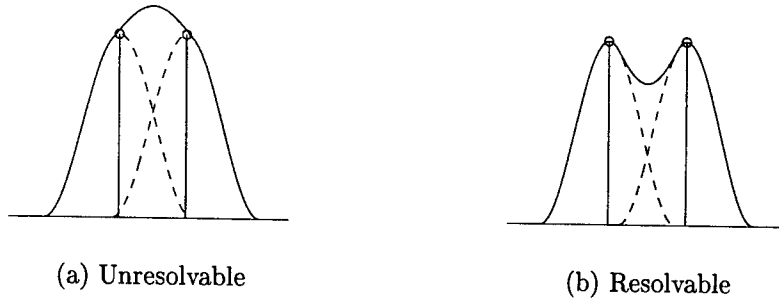


Figure 3-11: Simple illustration of time resolution imposed by the lowpass filter

Nevertheless, it is useful as an approximate measure of the temporal smearing introduced by the lowpass filter. The taper of the 0.4 second (120 point) Hanning window is such that it is not possible to resolve arrivals spaced more closely than 0.2 seconds.

In addition to smearing the signals in time, the lowpass-filtering operation also introduces a delay. The group delay of the filterbank specifies the time adjustment required to accurately relate the bandpass-filtered mode estimates to the received pressure time series. Provided that the filters have approximately constant delay across the passband, the correction involves a simple shift of the time axis. Fortunately, many of the standard analysis windows (including the Hanning window) qualify as generalized linear phase systems². Such systems are known to have a constant group delay, which is equal to $\left(\frac{L-1}{2}\right) f_s$ (where L is the filter length). All of the STFT estimates discussed in this thesis implicitly incorporate the filter delay correction.

Noise Response

A previous section has shown that the pseudo-inverse filter designed for 10 modes is well-conditioned and achieves nearly the optimal white noise gain. Since the modeshapes are functions of frequency, it is important to examine how the noise

²Specifically, these windows are real and symmetric: $h[l] = h[L-1-l]$, $0 \leq l \leq L-1$. Oppenheim and Schaffer discuss the properties of generalized linear phase systems in detail [68].

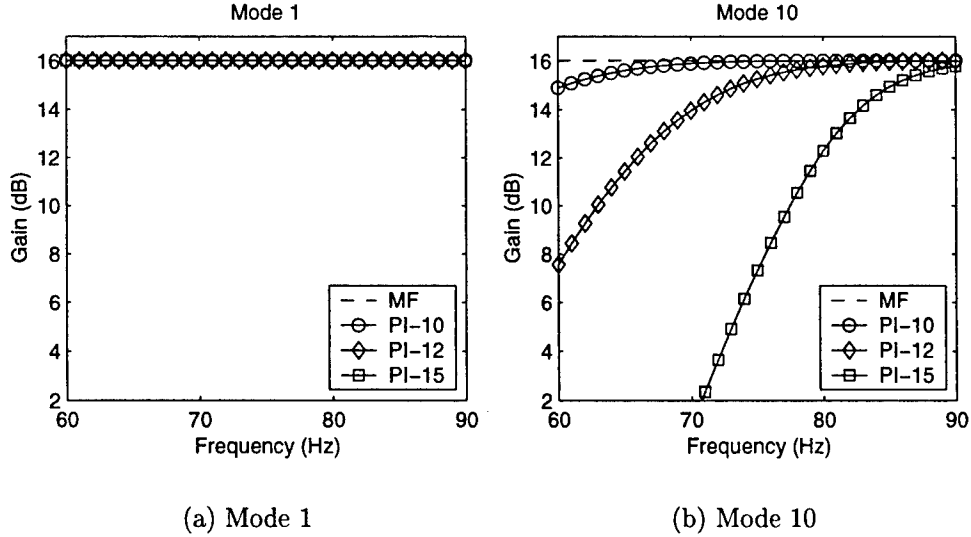


Figure 3-12: White noise gain as a function of frequency for the matched filter and three different pseudo-inverse filters (for 10 modes, 12 modes, and 15 modes).

characteristics vary over the source band. Figure 3-12 shows the white noise gain for modes 1 and 10, plotted over the 30 Hz interval corresponding to the ATOC source. The plots have 4 curves: one for the matched filter and three for different realizations of the pseudo-inverse filter which are designed for 10 modes, 12 modes, and 15 modes, respectively. Mode 1 is clearly unaffected by frequency, but conditioning problems are clearly evident for mode 10 PI filters. It is useful to compare these results with the plot of the modeshapes at 60 and 90 Hz, shown in Fig. 2-3 of Chapter 2. The changes in mode 1 with respect to frequency are negligible and that results in constant white noise gain across the band. Mode 10, on the other hand, changes significantly. At the lower frequencies the modeshape covers a greater extent of the water column than it does at the higher frequencies. As a result the array does not sample the mode as well, therefore the pseudo-inverse is more poorly conditioned. Based on these results, the 10-mode PI filter still appears to be reasonable choice for the ATOC data since its noise response does not change significantly across the source band.

Conclusions of the ATOC Design Example

Based on the numerical results presented above, the pseudo-inverse filter for 10 modes provides the best possible combination of noise gain and interference rejection. This filter has a bandwidth of approximately 5 Hz (± 2.5 Hz). An 0.4 second Hanning window has the desired bandwidth, and has the additional advantage of sidelobes that fall off faster than the crosstalk increases. These are the default parameters for the STFT processor designed for the ATOC data. Using this design, the next section applies STFT techniques to analyze a simple propagation example.

3.3 Adiabatic Example

The purpose of this section is to illustrate important characteristics of the STFT processor using an adiabatic propagation example. The discussion of this example consists of two parts. First, Section 3.3.1 shows the received pressure and corresponding mode estimates for adiabatic propagation through the California-Hawaii Levitus environment. Following that, Section 3.3.2 derives analytic expressions for these estimates to verify the numerical results and to provide more intuition about this type of mode processing.

3.3.1 Processing Results

Table 3.1 summarizes the parameters for the adiabatic simulation. The environment contains a broadband point source at 700 m depth, located 3515.2 km away from a 40-element receiving array (35 meter spacing). In this example, the source transmits a single windowed-sinusoidal pulse with approximately 30 Hz bandwidth, at a center frequency of 75 Hz. The time series for the receivers is synthesized using the first 40 modes. Figure 3-13 shows the received pressure as a function of time and depth for the adiabatic simulation. For this case, the modes are dispersed enough (at 3515.2 km range) that it is possible to identify individual modes in the pressure time

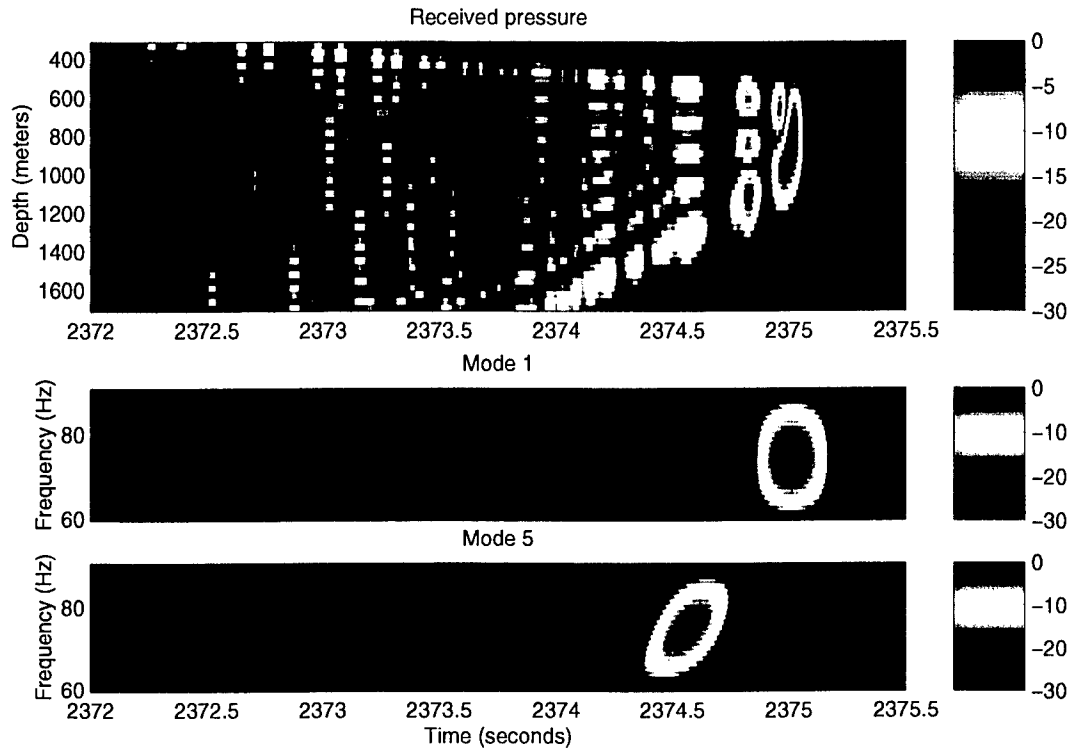


Figure 3-13: STFT example: processing of adiabatic propagation data. Top plot is the received pressure on a 40-element array as a function of time and depth. The bottom plots show the frequency-stacked outputs for modes 1 and 5, respectively.

Source	depth:	700 m
	center frequency:	75 Hz
	pulse:	triangular-windowed sinusoid
	pulse duration:	.11 secs (≈ 30 Hz bandwidth)
Receiver	range:	3515.2 km
	no. of receivers:	40
	element spacing:	35 m
	span:	330 m - 1695 m
	sample rate:	300 Hz
Modes	number synthesized at receiver:	40

Table 3.1: Simulation parameters for the California-Hawaii adiabatic propagation example

series, *e.g.*, mode 1 is the strong final arrival, and mode 5 is associated with the five strong peaks lined up right after 2374.5 seconds.

Mode estimates were calculated from this pressure time series using a 10-mode PI filter and the 0.4 second Hanning window filter described in the previous section. Note that “critical sampling” for this Hanning window requires computing bins every 2.5 Hz. Critical sampling refers to the bin-spacing required in theory to be able to resynthesize a time series from the STFT decomposition. For this example the STFT processor used a bin-spacing of 1.25 Hz; the additional samples improve the look of the plots, but do not improve the frequency resolution. The bottom two plots in Fig. 3-13 show the frequency-stacked outputs for modes 1 and 5. There are several interesting features to note. First, in this example these modes are actually evident in the pressure time series. The dispersion characteristics of the two modes are evident in the plots. Mode 1 is effectively undispersed, *i.e.*, all it arrives at the same time in all frequency bins. Mode 5 is clearly somewhat dispersed since the signal at lower frequencies arrives before the signal at higher frequencies.

Figure 3-14 shows the results of STFT processing for the first 10 modes. The significantly lower signal levels for modes 4, 6, and 9 are the result of low excitation of the mode by the source due to the low amplitude of these modes at the source depth. Modes 9 and 10 contain some energy arriving before their adiabatic arrival times; this is due to crosstalk from higher order modes not nulled out by the 10-mode PI filter. As noted above, the dispersion characteristics of the modes are evident in these plots. Note that because of the temporal smearing caused by the filter, the dispersion has to be on the order of 0.2 seconds before it will be evident in the STFT output.

3.3.2 Analysis

The starting point for the analysis of the adiabatic example is the filtered pressure time series (Eq. 3.5). Assuming that the signal consists of only the m th mode and

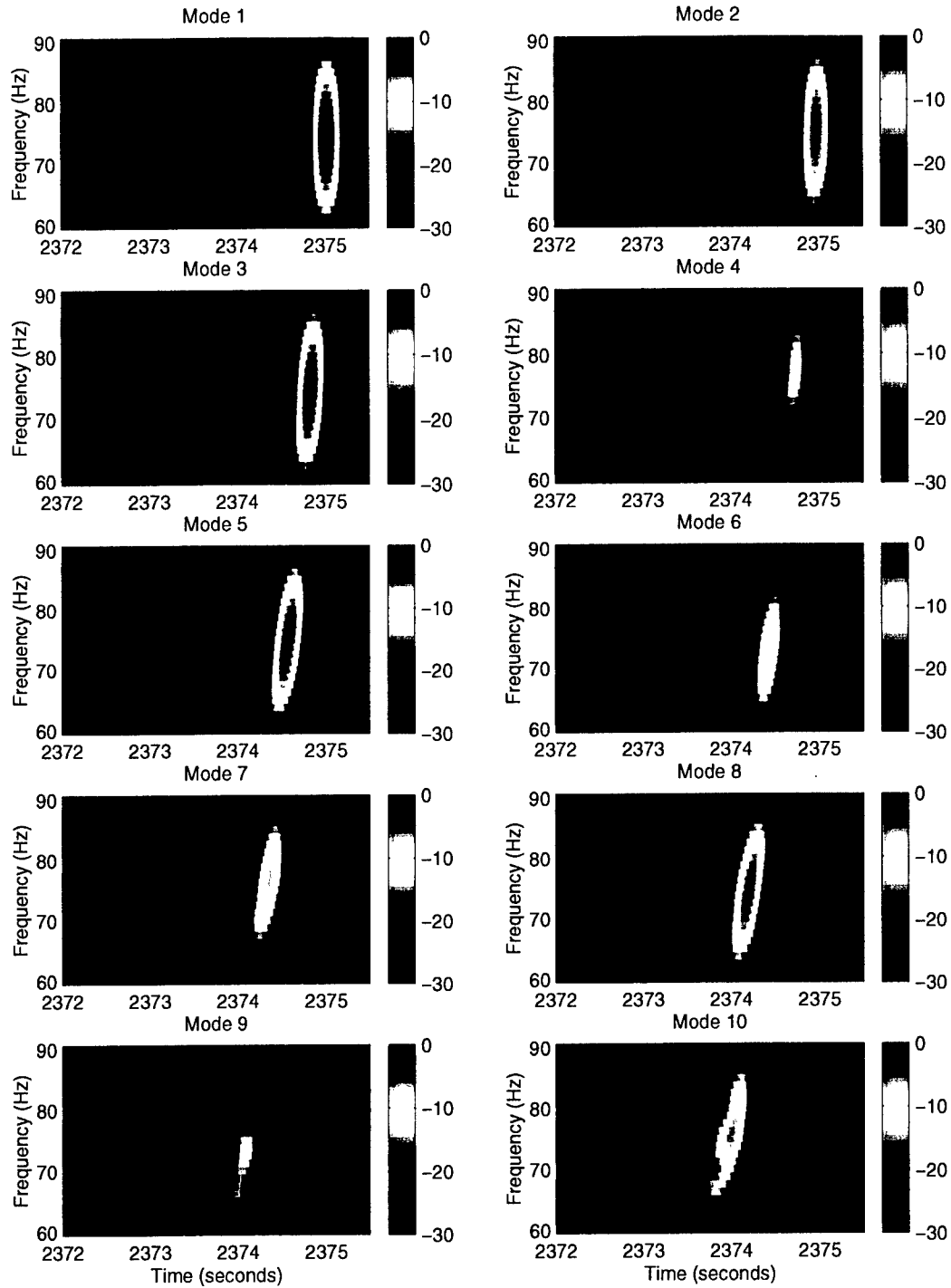


Figure 3-14: Estimated frequency-stacked outputs for the first 10 modes, computed using a pseudo-inverse filter

that there is no additive noise, the received pressure on the n th hydrophone in the k th band is

$$p_n^{(k)}[l] = \frac{1}{I} \sum_i H_{LP}[\omega_i] \phi_m[z_n, \omega_k + \omega_i] a_m[\omega_k + \omega_i] e^{j\omega_i l}. \quad (3.27)$$

As discussed previously, the lowpass filter has a generalized linear phase, meaning that its frequency response is of the form:

$$H_{LP}[\omega] = H[\omega] e^{j\omega(\frac{L-1}{2})} = H[\omega] e^{j\omega(t_H f_s)} \quad (3.28)$$

where $H[\omega]$ is a real and even function of ω , L is the number of points in the filter, and t_H represents the delay (in seconds) associated with filter, *i.e.* $t_H = \frac{L-1}{2f_s}$. For simplicity, this derivation assumes that the lowpass filter is designed to prevent significant spatial mismatch, thus $\phi_m[\omega_k + \omega_i] \approx \phi_m[\omega]$ for all ω_i passed by the filter. Using that assumption and substituting in the generalized linear phase representation of the lowpass filter yields

$$p_n^{(k)}[l] = \phi_m[z_n, \omega_k] \left(\frac{1}{I} \right) \sum_i H[\omega_i] a_m[\omega_k + \omega_i] e^{-j\omega_i(t_H f_s)} e^{j\omega_i l}. \quad (3.29)$$

The adiabatic model presented in Chapter 2 gives an expression for the frequency-dependent mode amplitude a_m . Based on equations 2.6 and 2.7, this amplitude is

$$a_m[\omega] = \underbrace{\frac{S_{src}[\omega] \phi_m[r=0, z_s, \omega]}{\rho[z_s]}}_{\text{source excitation}} \cdot \underbrace{\frac{e^{j\pi/4} e^{-jk_m[\omega]r}}{\sqrt{8\pi k_m[\omega]r}}}_{\text{channel}} \cdot \underbrace{e^{j\omega(t_0 f_s)}}_{\text{time advance}}. \quad (3.30)$$

In Eq. 3.30, the first term represents the excitation of mode m by a point source located at the range origin and the depth z_s . The second term represents the effects of the channel on the signal propagating in mode m . In this term, k_m is the adiabatic

(range-averaged) wavenumber, which is a function of frequency.³ The final term represents the phase shift required to time-advance the signal so that the I -term Fourier expansion corresponds to a reception starting at time t_0 seconds instead of 0 seconds. Before substituting the expression for a_m into Eq. 3.29, it is convenient to define the following spectral amplitude for mode m :

$$A_m[\omega, r] = \frac{S_{\text{src}}[\omega]\phi_m[r = 0, z_s, \omega]}{\rho[z_s]\sqrt{8\pi k_m[\omega]r}}. \quad (3.31)$$

For simplicity, assume that the source is zerophase and that its magnitude varies slowly with respect to ω .⁴ Since the modeshape and wavenumber are also smooth functions of ω , the amplitude A_m is slowly-varying function of frequency. Provided that the lowpass filter is sufficiently narrowband, the term $A_m[\omega_k + \omega_i]$, required by Eq. 3.29, is approximately equal to $A_m[\omega_k]$. With these assumptions, the pressure time series may be written

$$p_n^{(k)}[l] = A_m[\omega_k, r_n]e^{j\pi/4}\phi_m[z_n, \omega_k] \left(\frac{1}{I}\right) \sum_i H[\omega_i]e^{-j(k_m r_n - t_0 f_s)(\omega_k + \omega_i)}e^{-j\omega_i(t_H f_s)}e^{j\omega_i l} \quad (3.32)$$

where r_n is the range to the n th hydrophone.

The next step in the analysis requires a model for the variations of the modal wavenumber with frequency. Since the range-averaged wavenumber is not an analytic function in general, it is necessary to use a Taylor series for k_m . Expanding the

³The use of an overbar ($\overline{k_m}$) to indicate the range-averaged wavenumber has been dropped to simplify notation.

⁴This is equivalent to assuming either that the source transmits a symmetric pulse or that the receiver uses pulse compression (a temporal matched filter applied to the time series on each hydrophone). In the latter case S_{src} represents the Fourier transform of an autocorrelation function, which is symmetric. To be more precise, the source has a generalized linear phase representation (to account for time shifts of the pulse). There is no loss of generality in assuming zerophase since any linear phase term can easily be incorporated into the $e^{j\omega t_0 f_s}$ term in Eq. 3.30.

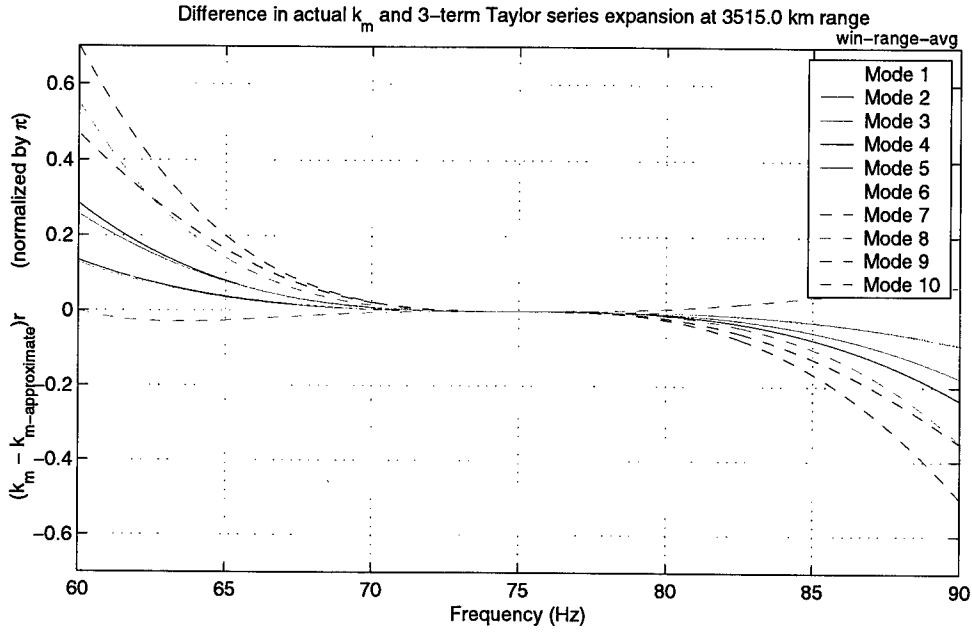


Figure 3-15: Difference in range-averaged wavenumber and 3-term Taylor series approximation for the CA-HI Levitus environment. Note that the phase differences are scaled by the range (3515 km) of the ATOC experiment and normalized by π .

wavenumber around the frequency Ω_c (continuous-time) yields

$$k_m[\Omega] \approx \underbrace{k_m[\Omega_c]}_{\Omega_c s_{pm}} + (\Omega - \Omega_c) \underbrace{\left. \frac{dk_m}{d\Omega} \right|_{\Omega=\Omega_c}}_{s_{gm}} + \frac{1}{2} (\Omega - \Omega_c)^2 \underbrace{\left. \frac{d^2 k_m}{d\Omega^2} \right|_{\Omega=\Omega_c}}_{d_m} + \dots \quad (3.33)$$

The terms s_{pm} , s_{gm} , and d_m represent the phase slowness, group slowness, and dispersion coefficient, respectively, for mode m . Ω_c is defined to be the center frequency of the source, *e.g.*, $f_c = 75$ Hz for the ATOC experiment. Figure 3-15 illustrates the accuracy of this approximation for the CA-HI Levitus environment. The plot shows the differences, scaled by range, in the actual wavenumber for the path and the 3-term Taylor series approximation. As the figure shows, phase errors due to the approximation are less than $\pi/4$ for the 20 Hz band (65-85 Hz) for the first 10 modes. Differences increase substantially outside of that band, especially for the higher order modes.

Using the Taylor series expansion, the second-order approximation to the $k_m r$ term in Eq. 3.32 is (after converting to DT frequency)

$$k_m[\omega_k + \omega_i]r \approx \omega_c s_{pm} r f_s + (\Delta\omega_k + \omega_i) s_{gm} r f_s + \frac{1}{2}(\Delta\omega_k + \omega_i)^2 d_m r f_s^2 \quad (3.34)$$

where

$$\Delta\omega_k = \omega_k - \omega_c. \quad (3.35)$$

Note that $s_{pm}r$ is the phase delay (seconds) and $s_{gm}r$ is the group delay (seconds) associated with propagation through the channel. Substituting Eq. 3.34 into Eq. 3.32 and taking the terms not involving ω_i outside the summation

$$p_n^{(k)}[l] = A_m e^{jB_m} \phi_m[z_n, \omega_k] \left(\frac{1}{I}\right) \sum_i H[\omega_i] e^{-j(t_m + t_H - t_0)f_s \omega_i} e^{-j\beta \omega_i^2} e^{j\omega_i l} \quad (3.36)$$

where B_m is a phase shift:

$$B_m[\omega_k, r_n] = \frac{\pi}{4} - \omega_c(s_{pm}r_n - t_0)f_s - \Delta\omega_k(s_{gm}r_n - t_0)f_s - \frac{1}{2}(\Delta\omega_k)^2 d_m r_n f_s^2, \quad (3.37)$$

t_m corresponds to the arrival time (in seconds) of the m th mode at frequency ω_k :

$$t_m[\omega_k, r_n] = s_{gm}r_n + \Delta\omega_k d_m r_n f_s, \quad (3.38)$$

and β is a dispersion factor:

$$\beta[r_n] = d_m r_n f_s^2. \quad (3.39)$$

Equation 3.36 looks complicated, but has a rather simple interpretation. $A_m e^{jB_m}$ is a complex scale factor and ϕ_m is the spatial weighting associated with the modeshape.

The summation represents the inverse Fourier transform of a pulse:

$$h_{\text{pulse}}[l] = \left(\frac{1}{I}\right) \sum_i \underbrace{H[\omega_i]}_{\text{pulse shape}} \underbrace{e^{-j(t_m + t_H - t_0)f_s \omega_i}}_{\text{pulse location}} \underbrace{e^{-j\beta \omega_i^2}}_{\text{distortion}} e^{j\omega_i l} \quad (3.40)$$

$$\approx h[l - (t_m + t_H - t_0)f_s] = h[l - l_m] \quad (3.41)$$

The first factor in the sum determines the pulse shape, the second term determines its location, and the third produces a distortion of the pulse shape (due to the dispersion of mode m). Since the passband of the filter is assumed to be very narrow,⁵ the distortion of the pulse shape is minimal. Neglecting the dispersion factor ($e^{-j\beta\omega_i^2}$), the pulse is simply a shifted version of the impulse response of the filter. In other words, the pulse looks like the window associated with the short-time transform, as is indicated in the approximate expression in Eq. 3.41. It is important to note that it is only the effect of dispersion on the pulse shape that is being neglected here. Modal dispersion also determines the phase of a mode arrival across the frequency bins of the STFT, and in general, the dispersion term in Eq. 3.37 cannot be neglected.

Substituting Eq. 3.41 into Eq. 3.36 yields

$$p_n^{(k)}[l] = \phi_m[z_n]A_m[r_n]e^{jB_m[r_n]}h[l - l_m[r_n]]. \quad (3.42)$$

where the dependence of ϕ_m , A_m , B_m , and l_m on ω_k is implicit and the dependence on the receiver coordinates (r_n, z_n) has been emphasized. Recall that spatial processing consists of computing a weighted sum of the pressure over N sensors, *i.e.*,

$$\hat{a}_m^{(k)}[l] = \sum_{n=1}^N w_m^H[z_n]p_n^{(k)}[l] \quad (3.43)$$

where $w_m[z_n]$ is the n th component of the weight vector for mode m . Substituting Eq. 3.42 into Eq. 3.43 results in an approximate expression for the estimated time series for mode m . The resulting equation illustrates what happens for both vertical and non-vertical array geometries.

First, consider the case of a vertical array, where $r_n = r$ for all n . Most of the

⁵Note that if the narrowband assumption for $H[\omega_i]$ is violated, spatial crosstalk, rather than phase distortion, is likely to be the dominant source of errors.

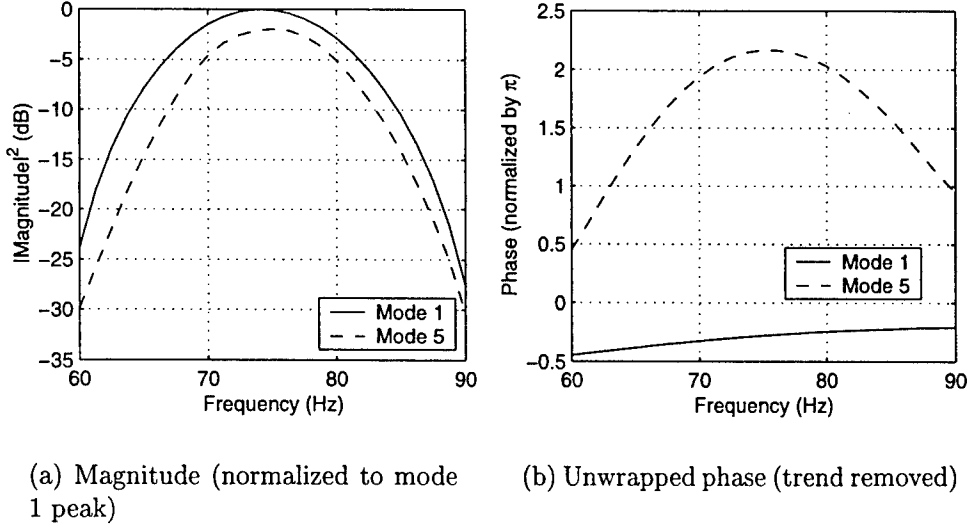


Figure 3-16: Magnitude and phase across frequency at the peak arrival time in the 75 Hz bin for modes 1 and 5 of the adiabatic example

terms can be pulled outside the sum, therefore

$$\hat{a}_m^{(k)}[l] = A_m e^{jB_m} h[l - l_m] \underbrace{\sum_{n=1}^N w_m^H[z_n] \phi_m[z_n]}_{= 1} \quad (3.44)$$

The summation is equal to one because of the unity gain constraint imposed on the weight vector. From Eq. 3.44, the mode m signal in the k th band is a pulse centered around sample l_m . Converting from samples to seconds, mode m arrives at time $t = t_m + t_H$ (assuming the source emits a pulse at $t = 0$). The amplitude and phase (A_m and B_m , respectively) do not vary over the extent of the arrival, *i.e.*, they are not functions of l . Amplitude, phase and arrival time do depend on the frequency ω_k as indicated by equations 3.31, 3.37, and 3.38.

Consider taking a slice of the STFT estimate across frequency at the peak arrival time. This gives a measure of the amplitude A_m and the phase B_m . Figure 3-16 shows the frequency slices taken at the peak arrival times for modes 1 and 5 of the adiabatic example. The amplitude reflects the spectrum of the source (the triangular-

windowed sinusoid). For mode 5, the amplitude is also affected by the fact that the peak arrivals in the bins do not line up exactly (due to dispersion within mode 5). The latter effect is minimal.

Note that the phase of the arrival across frequency bins has a linear term associated with its arrival time relative to the start of the reception. This is expected since a delay in the time domain corresponds to a phase shift of the Fourier transform. For the results shown in Fig. 3-16(b) this trend has been removed. In theory, the linear component can be completely removed, given knowledge of the arrival time relative to the start of the processing interval. In practice, a small linear component may remain due to the fact that the picked peak may not correspond to the exact arrival time of the pulse (can be off due to noise, etc.).

As long as dispersive spreading within mode m is not greater than the window width, the amount of dispersion can be measured using a frequency slice taken at a constant time. If the dispersive spreading is larger than the window width (0.4 seconds in this case), then it would be necessary to look along a slanted line in time-frequency space. For the adiabatic modes of the California-Hawaii Levitus environment, the maximum dispersive spreading up to mode 10 is approximately 0.4 seconds.

How do the adiabatic results generalize? It is worth pointing out that even in non-adiabatic cases, we can still associate a magnitude, phase, and time with an arrival. In the general case, the effective wavenumber would be a weighted average of the wavenumbers of the modes that the signal has traversed the path in. Removal of the linear term in the phase is still possible because that simply requires knowledge of the arrival time of the pulse. In this way, it may be possible to get insight about the dispersion characteristics of a particular multipath arrival.

3.4 Mooring Corrections

The previous discussion has assumed a perfectly vertical array for the pressure measurements, *i.e.*, all sensors located at the same range from the source. This section relaxes that assumption and considers the practical problem of compensating for array tilt. Since STFT processing involves a joint time/frequency representation of the signals, the mooring corrections involve both a phase and a time adjustment. For the purposes of this chapter, it is assumed that accurate location information is available for all sensors. This is a reasonable assumption in many experiments like ATOC.

Building upon the derivation in the previous section, assume that the array is not vertical. In cylindrical coordinates, this means that the distance to the n th sensor is $r_n = r - \Delta r_n$, where r is a reference distance. In this case the mode estimate becomes (from Eq. 3.43):

$$\hat{a}_m^{(k)}[l] = \sum_{n=1}^N A_m[r - \Delta r_n] e^{j(B_m - \Delta B_m)} h[l - (l_m - \Delta l_m)] (w_m^H[z_n] \phi_m[z_n]) \quad (3.45)$$

where ΔB_m and Δl_m depend on Δr_n :

$$\Delta B_m = -\omega_c s_{pm} f_s + \Delta \omega_k s_{gm} \Delta r_n f_s + \frac{1}{2} (\Delta \omega_k)^2 d_m \Delta r_n f_s^2, \quad (3.46)$$

$$\Delta l_m = (s_{gm} + \Delta \omega_k d_m) f_s \Delta r_n. \quad (3.47)$$

In reducing this equation, first consider the amplitude A_m , given by Eq. 3.31. Provided that r is large compared to Δr_n , the amplitude is unaffected by the fact that the array is not vertical. This is certainly true in ATOC where r is on the order of megameters and Δr_n on the order of 100 meters. The phase shift and time shift terms, ΔB_m and Δl_m are much more significant. Note that the phase shift ΔB_m is simply the second order approximation to $k_m \Delta r_n$. Using this information, Eq. 3.45

becomes

$$\hat{a}_m^{(k)}[l] = A_m e^{jB_m} \sum_{n=1}^N h[l - (l_m - \Delta l_m)] w_m^H[z_n] \phi_m[z_n] e^{jk_m \Delta r_n}. \quad (3.48)$$

From this equation, it is clear that the array tilt results in a phase shift *and* a time shift of the pulse associated with each sensor. In general, compensation for both of these effects is required for proper interpretation of the STFT mode estimates.

Based on Eq. 3.48, the way to implement the phase adjustment is to design the mode filters for complex modeshapes, *i.e.*,

$$\phi_m = \begin{bmatrix} \phi_m(z_n) e^{jk_m r_1} \\ \phi_m(z_n) e^{jk_m r_2} \\ \vdots \\ \phi_m(z_n) e^{jk_m r_N} \end{bmatrix}. \quad (3.49)$$

Using complex modeshapes is the standard way to incorporate the phase compensation into the MF, PI, or other mode filter designs. Note that the derivations presented in Section 3.2.1 are equally-valid for the case of complex modeshapes.

The corrections for the time shift due to array tilt are easily implemented by adding the appropriate delay to the lowpass-filtering operation. It is useful to consider whether the time-corrections need to be done on a mode-by-mode basis or not. The dominant term in the time shift, l_m is $s_{gm} \Delta r_n$ (the dispersion being a 2nd order effect). Figure 3-17 shows the difference in the delay term associated with mode m and the delay term associated with mode 1, *i.e.*, $t_m - t_1$ as a function of the change in range Δr_n . The group slownesses used for this calculation are those associated with the range-averaged Levitus wavenumbers. The differences are less than 3 milliseconds up to differential ranges of 10 km. For most vertical array geometries, the maximum value of Δr_n , will be much less than the maximum value shown here. The maximum Δr_n for the ATOC experiment is less than 300 m. Clearly, for that con-

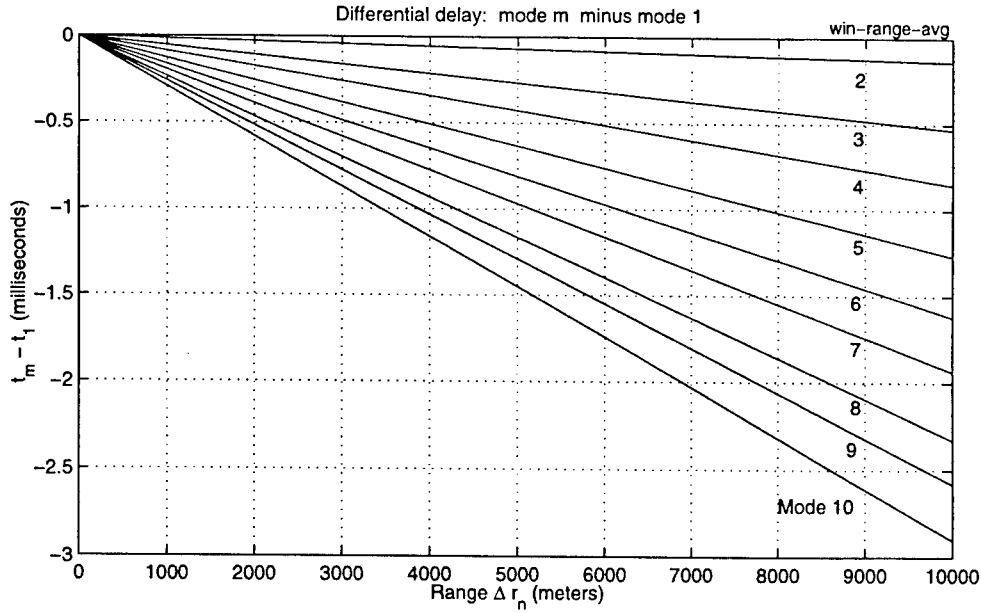


Figure 3-17: Difference in delay

figuration, the difference due to mode number is negligible. Making the assumption that the time shift is mode-independent simplifies the processing, since it means that the filterbank will be identical for all modes.

3.5 Impact of Environmental Uncertainty

The purpose of this section is to briefly address the issue of environmental uncertainty in the context of broadband mode processing, specifically in terms of the ATOC experiment. The modeshapes used in designing the mode filters depend on the local environment at the receiving array. For the ATOC experiment, there were only two measurements of that environment: one when the array was deployed in November of 1995 and one when the array was recovered in August of 1996. Figure 3-18 shows the sound speed profiles associated with these two environmental measurements. The differences in these two measured profiles are slight, compared to the difference between the measured profiles and their archival counterparts (see the comparison of Levitus and measured in Chapter 2. Still, these differences do affect the mode shapes

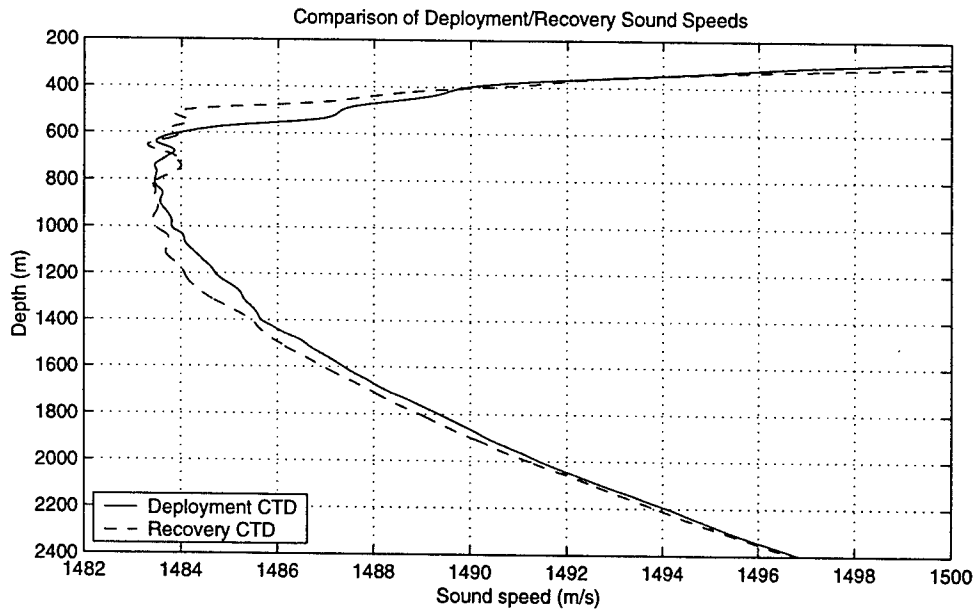


Figure 3-18: Comparison of deployment and recovery sound speed profiles

and wavenumbers, which means they affect the performance of the spatial filter in two ways: in the spatial beampattern and in the mooring corrections. Figure 3-19 shows the modeshapes at 75 Hz for the two different profiles. First consider how mismatch affects the beampattern. Figure 3-20 shows the effective PI beampattern when the mode filters are designed using the deployment-profile modes, but the true underlying modes of the signal correspond to those for the recovery profile. Figure 3-21 shows similar results for the matched filter case. As both of these beampatterns illustrate, mismatch produces nearest-neighbor coupling of energy. In the worst case, neighboring modes are only about 10 dB down (in power) from the peak in the desired mode. While there are slight differences in the mismatched beampatterns for the PI and MF designs, the magnitude of the coupling is the same for both.

In addition to altering the beampattern, mismatch may also affect the mooring corrections. For ATOC, the maximum difference in the wavenumbers at 75 Hz between the deployment and recovery profiles is approximately 2×10^{-5} , thus the phase errors involved in correcting for a maximum Δr_n of 300 m are negligible.

Since only 2 measurements of the receiver environment are available for the ATOC

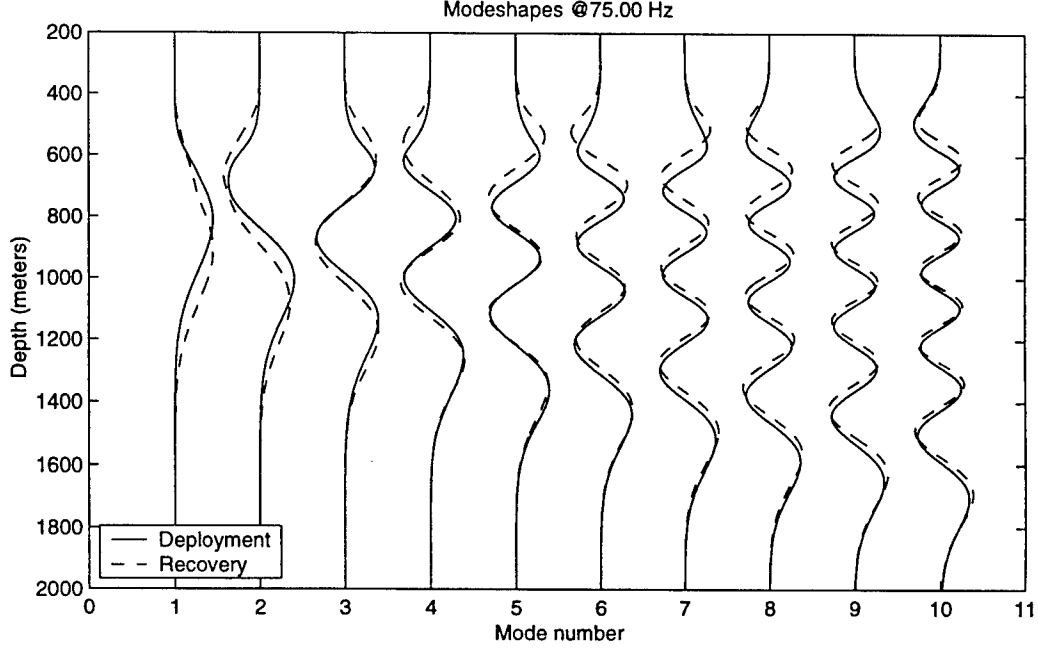


Figure 3-19: Comparison of deployment and recovery modeshapes at 75 Hz

experiment, it is hard to characterize the maximum possible mismatch (the profiles during when the receptions occurred could be very different from either of the measurements). The archival profiles are offset from both the measured profiles by enough that they are not useful for estimating the profile in between the two measurements. Accurate characterization of the local environment is obviously an important issue in mode estimation. It is possible to envision schemes for mitigating the impact of this mismatch, but they require more information and are beyond the scope of this thesis.

3.6 Summary

This chapter has presented a short-time Fourier framework for broadband mode processing. The narrowband mode filters that are a part of the STFT structure were derived using a different approach than the standard one in the acoustics literature. This approach made the connection of mode processing to optimal beamforming.

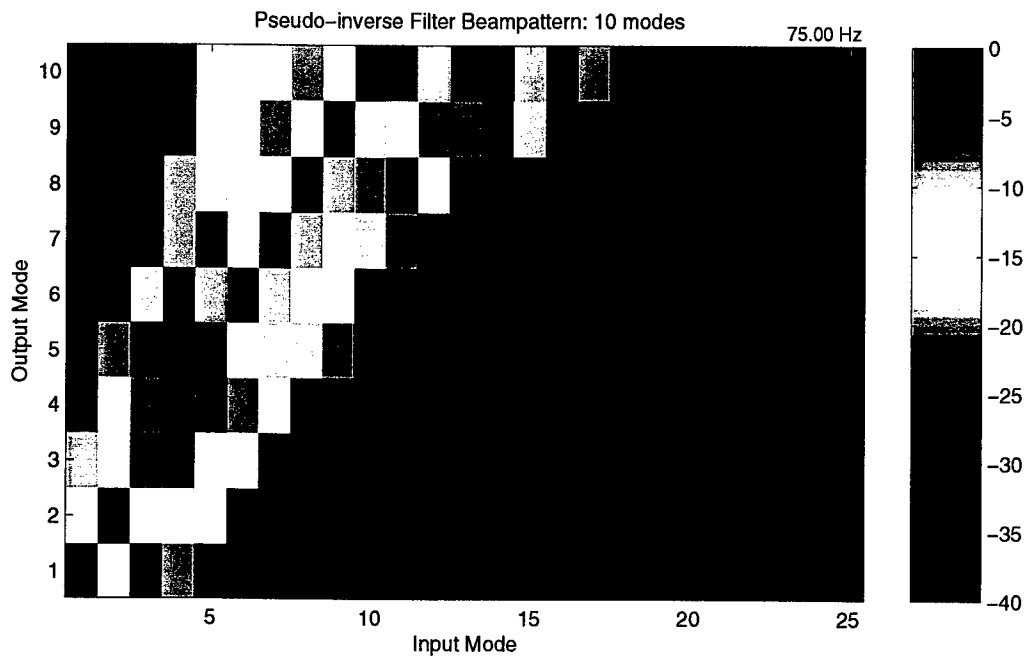


Figure 3-20: Beampattern for the mismatch case: PI filter designed with deployment profile modes; recovery profile modes are the input

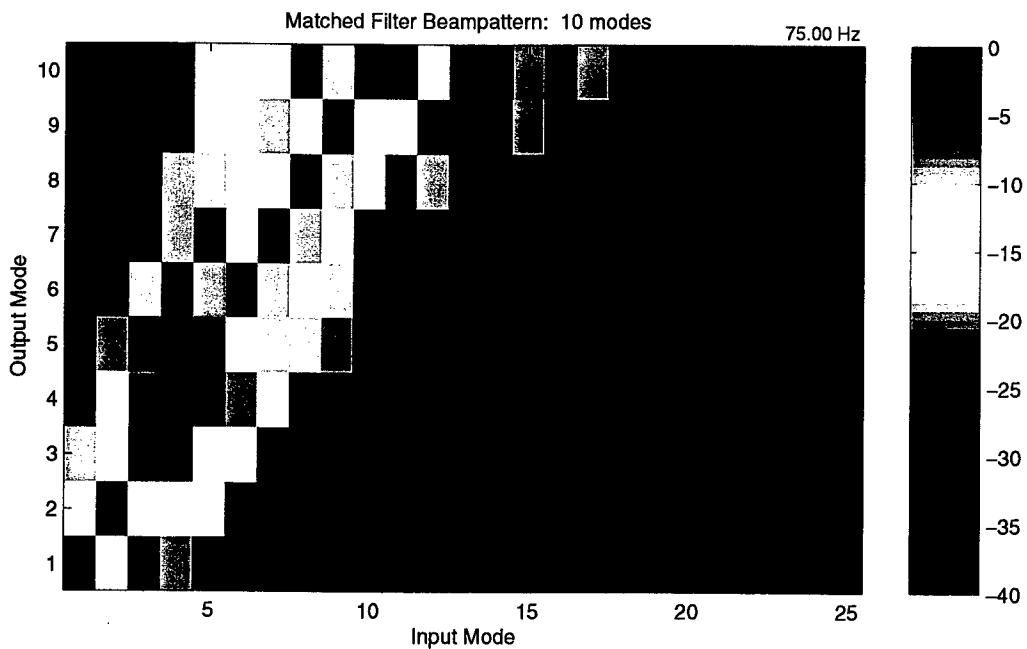


Figure 3-21: Beampattern for the mismatch case: matched filter designed with deployment profile modes; recovery profile modes are the input

A thorough performance analysis of the system has explored both narrowband and broadband issues. Based on this analysis, the STFT processor parameters for the ATOC data were chosen.

Chapter 4

STFT Mode Analysis of ATOC Receptions

As stated in Chapter 1, the motivation for developing a framework for broadband mode estimation is to study the mode arrivals at megameter ranges. This chapter presents an analysis of the ATOC receptions on the Hawaii VLA, using the short-time Fourier techniques described in the previous chapter. Processing of the ATOC data reveals a complicated multipath arrival pattern for the first 10 modes at 3515 km range. This chapter investigates the frequency characteristics of the measured arrival structure, compares experimental estimates to simulation results, and identifies several useful statistics for characterizing the low-mode signals.

The outline of this chapter is as follows. Section 4.1 begins by introducing the ATOC data set, focusing on the receptions at Hawaii considered in this thesis. Following that, Section 4.2 describes a set of PE simulations used for comparison purposes. Section 4.3 provides the first look at the time-varying mode spectra for the ATOC receptions and compares the experimental results to the STFT estimates for simulated receptions. Next, Section 4.4 addresses the issue of temporal variability by comparing ATOC data with simulated receptions, and computing average coherence as a function of time. Section 4.5 examines some statistics of the mode estimates,

obtained by averaging over multiple transmissions. Finally, Section 4.6 summarizes major conclusions of this chapter.

4.1 ATOC Data Set

As described in Chapter 1, the ATOC experiment involved a bottom-mounted source at Pioneer Seamount (off California) broadcasting to two vertical arrays and a set of bottom-mounted receivers in the Northeastern Pacific. The source transmitted phase-encoded pseudo-random sequences at a center frequency of 75 Hz, with a 3 dB bandwidth of 37.5 Hz. Each transmission consisted of 44 repetitions of the 27.28 second pseudo-random sequence, corresponding to a transmission length of approximately 20 minutes. The source and the two VLA's were deployed in the fall of 1995, and regular transmissions began in December of that year. Over the course of the experiment, the source transmitted signals every four hours during periods set by the Marine Mammal Research Program associated with ATOC.

This thesis considers only the data recorded on the Hawaii VLA, which was located at a range of 3515.2 km from the source. Figure 4-1 shows the schedule of reception times for this array from December 28, 1995 (yearday 362) to May 23, 1996 (yearday 509).¹ Although the array was not recovered until August 1996 the deepest 20 hydrophones failed sometime after day 509. Since mode processing is much more difficult with only the shallow half of the array (due to poor sampling of the modeshapes), this study is limited to 188 receptions recorded on the full array.

For each transmission, the 40-element array recorded 10 four-period averages (over 18.2 minutes) of the pseudo-random sequence received on each hydrophone.² Subsequently, the time series for each sensor was demodulated and matched-filtered

¹This plot only shows the times of 188 "good" receptions. There were 229 transmissions between yeardays 362-509, but 41 of these have been ignored due to incomplete or corrupted data.

²Although the source transmitted 44 periods of the M-sequence, the array only recorded 40 periods. The start-time for recording was chosen so that sampling began approximately two periods after the start of the reception [69].

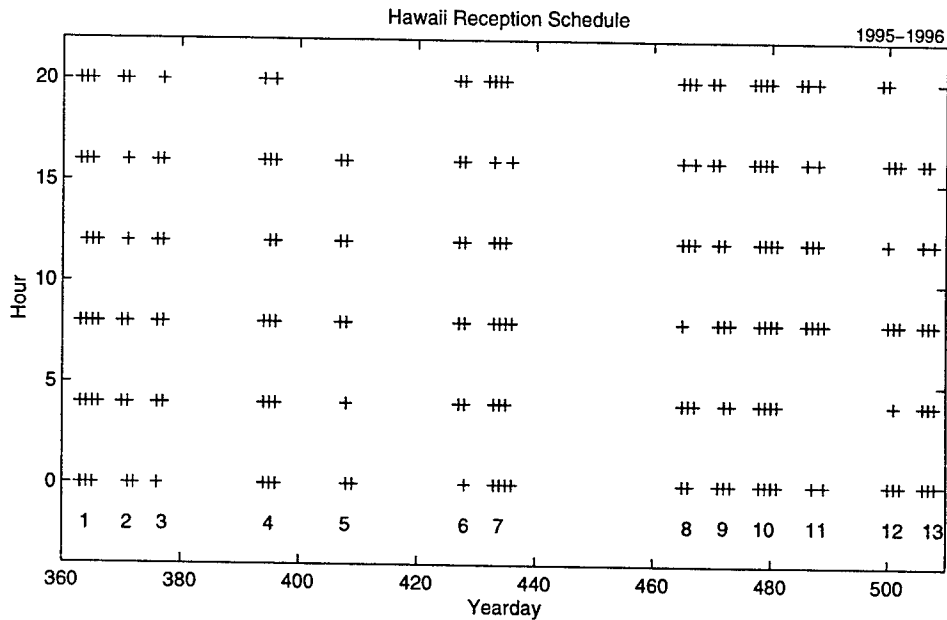


Figure 4-1: ATOC transmission schedule through yearday 509. Crosses mark the time of each good reception; receptions with bad channels have been eliminated from the data set. The line of numbers below the crosses indicates how the receptions are divided into 13 subgroups for post-processing.

to achieve pulse compression. For the purposes of all the numerical results presented in this thesis, the received pressure time series consists of these matched-filtered demodulates.

During the experiment, the position of the VLA was tracked using a long-baseline acoustic navigation system consisting of four transponders deployed on the bottom and several interrogator hydrophones on the array. Navigation data was recorded immediately before and after each reception. This thesis relies on the mooring motion calculations done by the group at Scripps. Array positions for each of the 10 four-period averages were determined by interpolating between the beginning and ending locations of the array.

Before analyzing the mode arrivals in the ATOC receptions, it is useful to have estimates of the input noise levels. The intent is to provide some approximate noise statistics for use in setting thresholds for plotting and peak detection, rather than

to undertake a thorough analysis of the noise at the ATOC arrays. Since no separate noise measurements were made for the ATOC experiment, noise levels must be estimated from the receptions themselves. The approach taken here is to use two “noise-only” segments of the 27.28 second received time series to calculate statistics. For the Hawaii array, at least 7 seconds at the beginning of the reception and 4 seconds at the end of the reception do not appear to contain any strong signal components. These two sections of data are used in the noise analysis.

Figure 4-2 shows estimated noise spectra on two hydrophones for the first reception on yearday 363 (one of the 4-period averages). These estimates were computed

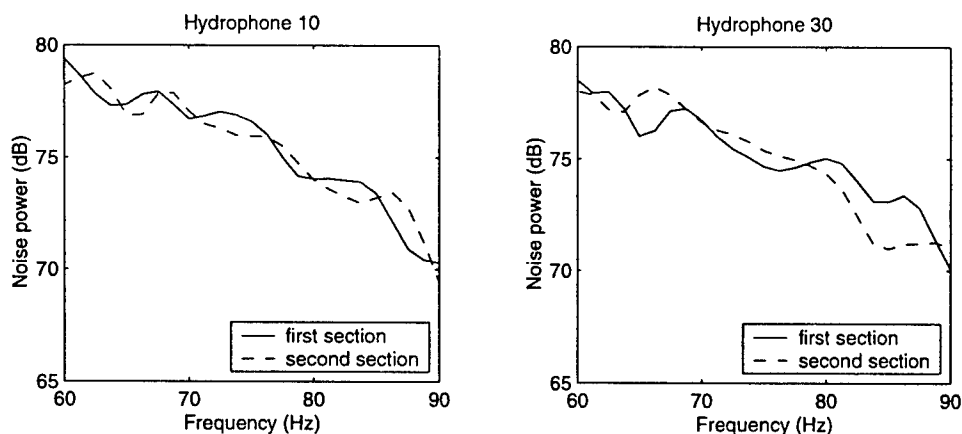


Figure 4-2: Estimated noise spectra for hydrophones 10 and 30. The solid line is computed using the noise-only section prior to the signal arrival; dashed line is computed using the noise-only section after the signal arrivals.

using the modified periodogram method of Welch [70, 66]. The data window used in the processing is an 0.4 second Hanning window, thus the frequency resolution of the noise estimates is comparable to that of the STFT mode processor (approximately ± 2.5 Hz bandwidth). Window overlap is 50%, resulting in 30 and 24 segments for the periodogram averages of the first and second noise-only sections, respectively. As the figure shows, noise power estimates for the first and second sections (beginning and end of the received time series, respectively) are consistent. Noise is obviously a function of frequency, with the levels at 90 Hz being down from those at 60 Hz by

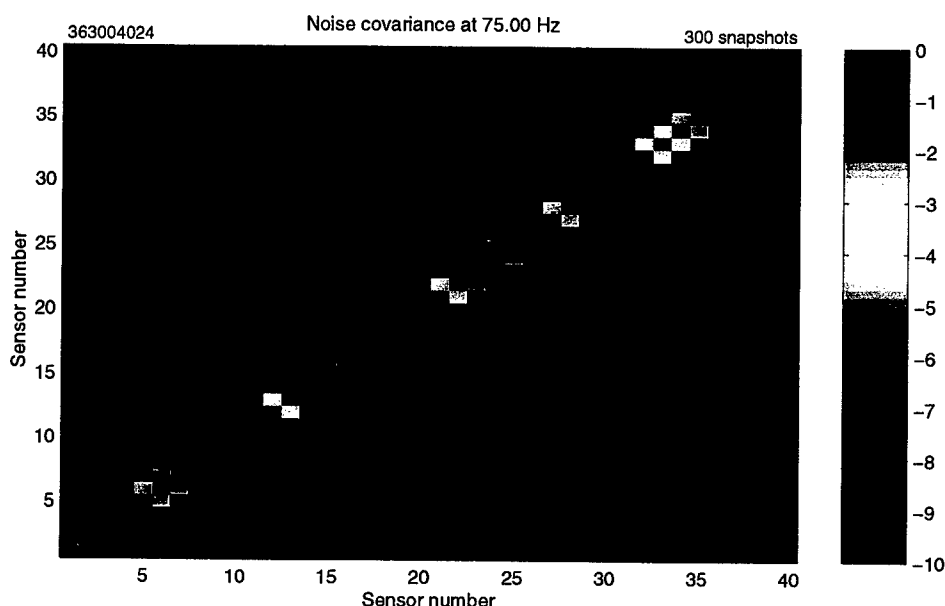


Figure 4-3: Estimated spatial covariance in the 75 Hz bin; calculated from 300 snapshots. Units are dB, referenced to peak value.

approximately 6 dB.

Based on Fig. 4-2, the noise levels on hydrophone numbers 10 and 30 are comparable. To get a better idea about the spatial characteristics of the noise, consider the spatial covariance matrix shown in Fig. 4-3. This covariance matrix is calculated for the 75 Hz bin of the same reception. The beginning (30 segments) were used and the results were averaged over the 10 periods (4-period averages) recorded by the receiver. The covariance is dominated by the diagonal terms, with some nearest neighbor correlation, but no other obvious structure.

The results shown in Figures 4-2 and 4-3 are representative of the results for other receptions and support the conclusion that the noise field is approximately spatially white. Since the results for the first noise-only section are similar to the second section, it is reasonable to average those results together. In addition, the noise estimates can be averaged over hydrophones (assuming spatially white) and over the 10 4-period averages in order to obtain a single average noise spectrum for each reception. No frequency-averaging has been done. Figure 4-4 shows how

these averaged noise statistics vary over the course of the experiment. For reference,

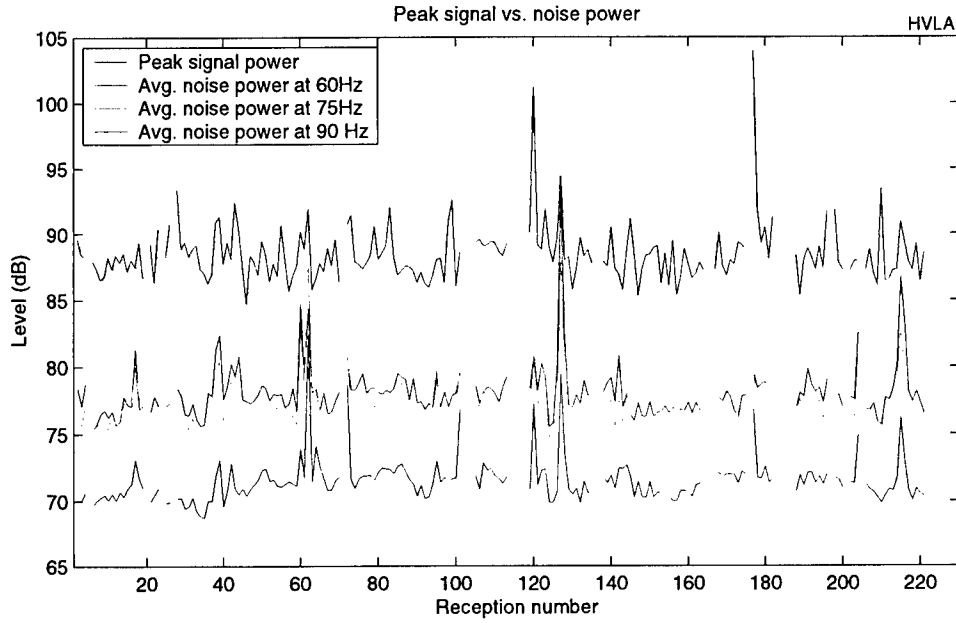


Figure 4-4: Input noise levels at 60, 75, and 90 Hz as a function of reception number.

the peak signal power in each reception (*i.e.*, the maximum pressure received on a single hydrophone) is also shown. Note that the noise varies significantly enough from reception to reception that it is important to set plotting/detection thresholds individually for each.

Assuming a spatially white model for the input noise, it is easy to compute the noise levels at the output of each bin of the STFT mode processor. If the gain of the lowpass filter for the STFT is set to give unit power throughput, the noise power at the output of the filterbank is identical to the spectral estimates described above. Since the noise is assumed to be spatially white, the noise power in the estimate of mode m is simply the estimated noise level for that frequency bin times the squared length of the weight vector for that mode, *i.e.*, $\mathbf{w}_m^H[\omega_k]\mathbf{w}_m[\omega_k]$.

In the numerical results presented in this chapter, the plotting thresholds are set on a reception-by-reception basis as follows. For plots of the received pressure time series, the 0 dB power level corresponds to the estimated noise floor associated with

the 75 Hz bin. In the modal time series, the 0 dB level corresponds to the noise level in mode 1 at 75 Hz for that reception.

4.2 Simulated Data Set

For comparison purposes, a simulated data set has been generated using the parabolic equation code RAM [14]. The simulations are designed to model propagation along the Pioneer-Hawaii path. Background sound speed profiles for the simulation environment are the Levitus-winter profiles along the geodesic path between Pioneer Seamount and the Hawaii array, shown in Chapter 2. The bathymetry for the simulations corresponds to actual bathymetry along the path with the exception of one simplification: the steep downslope near the source has been eliminated. The source is at 939.5 meters depth (the depth of the seamount where the source is located); bottom depth at the source range is 3317 m. Section 4.3.3 illustrates the effects of adding the seamount back into the simulations, and indicates that source bathymetry may affect the spread of the final arrivals.

The simulated data set consists of multiple realizations of the received time series on a 40-element array with sensors located at the nominal ATOC VLA depths. In addition to one time series for the Levitus background environment, there are 15 time series which include sound speed perturbations due to internal waves. Realizations of the internal wave (IW) field were generated using the method of Colosi and Brown [13]. A 1/2 Garrett-Munk strength was used for all simulations, in accordance with the earlier findings of Colosi. Ten of the 15 IW simulations are for independent realizations of the internal wave field. The other 5 are for successive time steps associated with one of the independent realizations.

The PE code generates solutions of the frequency-dependent wave equation. Broadband simulations therefore require Fourier synthesis of the PE results to produce a time series. The frequency-spacing used for the PE calculations determines

the time interval that can be represented without aliasing. For the ATOC environment, the time spread of all the arrivals (ray-like and mode-like) is on the order of 10-20 seconds, implying a required frequency spacing of 0.1-0.05 Hz. Since the low mode arrivals are the signals of primary interest in this thesis, a simplification is possible, which permits a wider frequency spacing (thus a significant computational savings). In these simulations the pressure field is calculated for each frequency and projected onto the modes of the receiver environment. Then, only a subset of those modes are used to synthesize the time series. Empirical results indicate that, for this frequency range, 45 modes are fully contained within an 8 second interval; 25 modes are contained within a 4 second window. Thus, a frequency spacing of 0.125 Hz or 0.25 Hz is permitted provided that the time series is synthesized with only 45 or 25 modes, respectively. Note that 4-second simulations are more than adequate for examining the behavior of the first 10 modes.

The simulations do not contain any additive noise components. In order to use a dB scaling for the plots that is consistent with the real data, it is assumed that there is a noise floor 12 dB below the peak in the pressure field. This level was chosen based on the average peak-to-noise ratio in Figure 4-4. Simulated pressure time series are scaled so that this assumed noise floor is at 0 dB; mode time series are scaled with respect to the assumed noise floor for the mode 1 estimate.

4.3 Modal Time Series: Experiment vs. Simulation

This section examines the mode estimates for one ATOC reception and compares them to estimates for two simulated receptions. One simulation is for the Levitus background environment; the other is for the background environment plus sound speed perturbations due to internal waves. The purpose of this section is to highlight important features of the short-time mode spectra and to illustrate qualitative

agreement between the ATOC data and the simulation that includes internal wave effects.

4.3.1 ATOC Reception

Figure 4-5 is a plot of a demodulated pressure time series (one 4-period average) recorded on the Hawaii array in late December 1995. For reference, the pressure time series for the simulations discussed later are displayed below the ATOC reception (Figures 4-6 and 4-7). In the ATOC reception, the early-arriving planewaves (or ray arrivals) are rather weak. Unlike the adiabatic examples considered in previous chapters, there are no immediately identifiable modes contained in the late-arriving energy.

The mode estimates for this reception are calculated using short-time Fourier techniques developed in Chapter 3. Recall that the STFT processor designed for the ATOC data uses an 0.4 second Hanning window and a 10-mode pseudo-inverse spatial filter. Note that for the plots in this chapter, the STFT estimates are computed for the 60-90 Hz band, with a bin spacing of 1.25 Hz. The latter is chosen for plotting purposes only; the critical frequency spacing required by the choice of window is 2.5 Hz.

Figure 4-8 shows the frequency-stacked plots for the first 10 modes of this ATOC reception. There are a number of observations to make about these results. First, each mode consists of multiple arrivals, spread over 2-3 seconds. This is a stark contrast to the single, dispersive arrivals that characterized the adiabatic propagation example discussed in the last chapter. Also, recall that in the adiabatic case, the modes arrive in descending order and the highest modes are temporally separable from the lowest modes. For this ATOC reception, there is no obvious ordering of the arrivals and the spread of the signals is such that the first ten modes overlap in time.

The third point to consider concerns a common feature of multipath channels: frequency-selective fading. This type of fading occurs when two signals with different

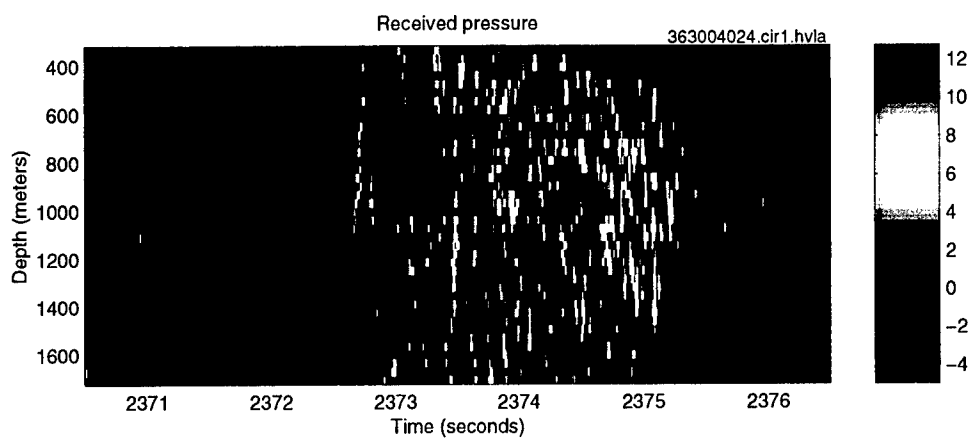


Figure 4-5: ATOC Reception

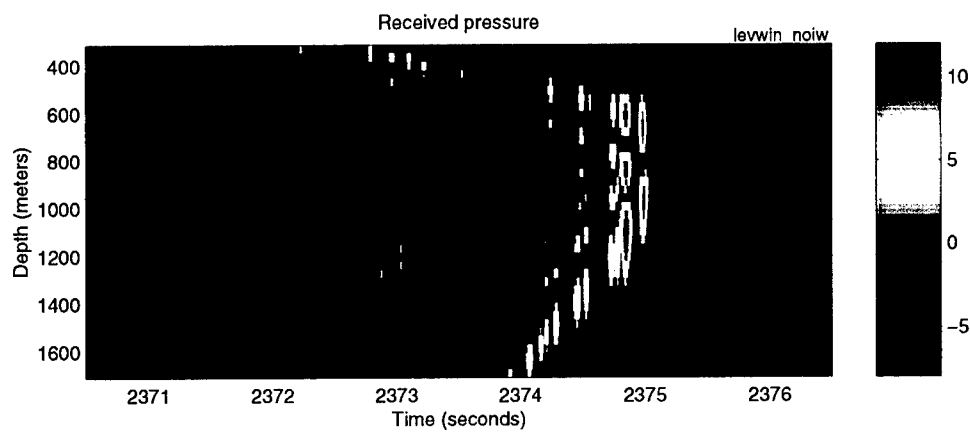


Figure 4-6: PE simulation without internal waves

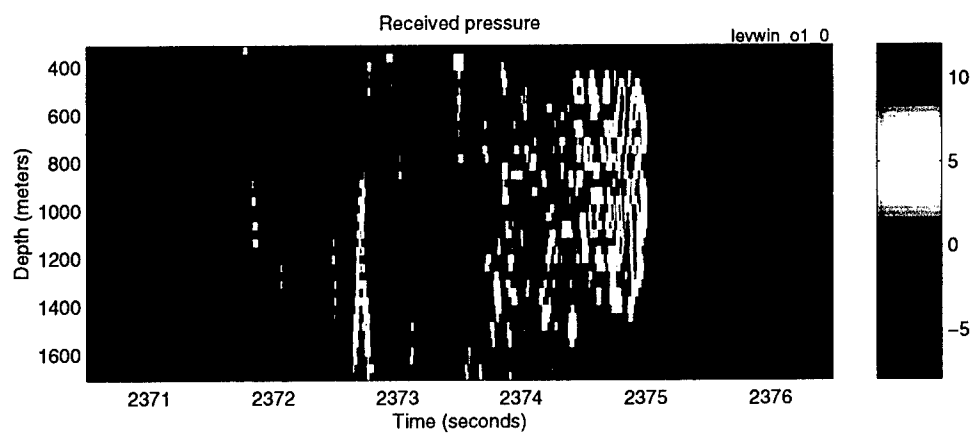


Figure 4-7: PE simulation with internal waves at 1/2 Garrett-Munk strength

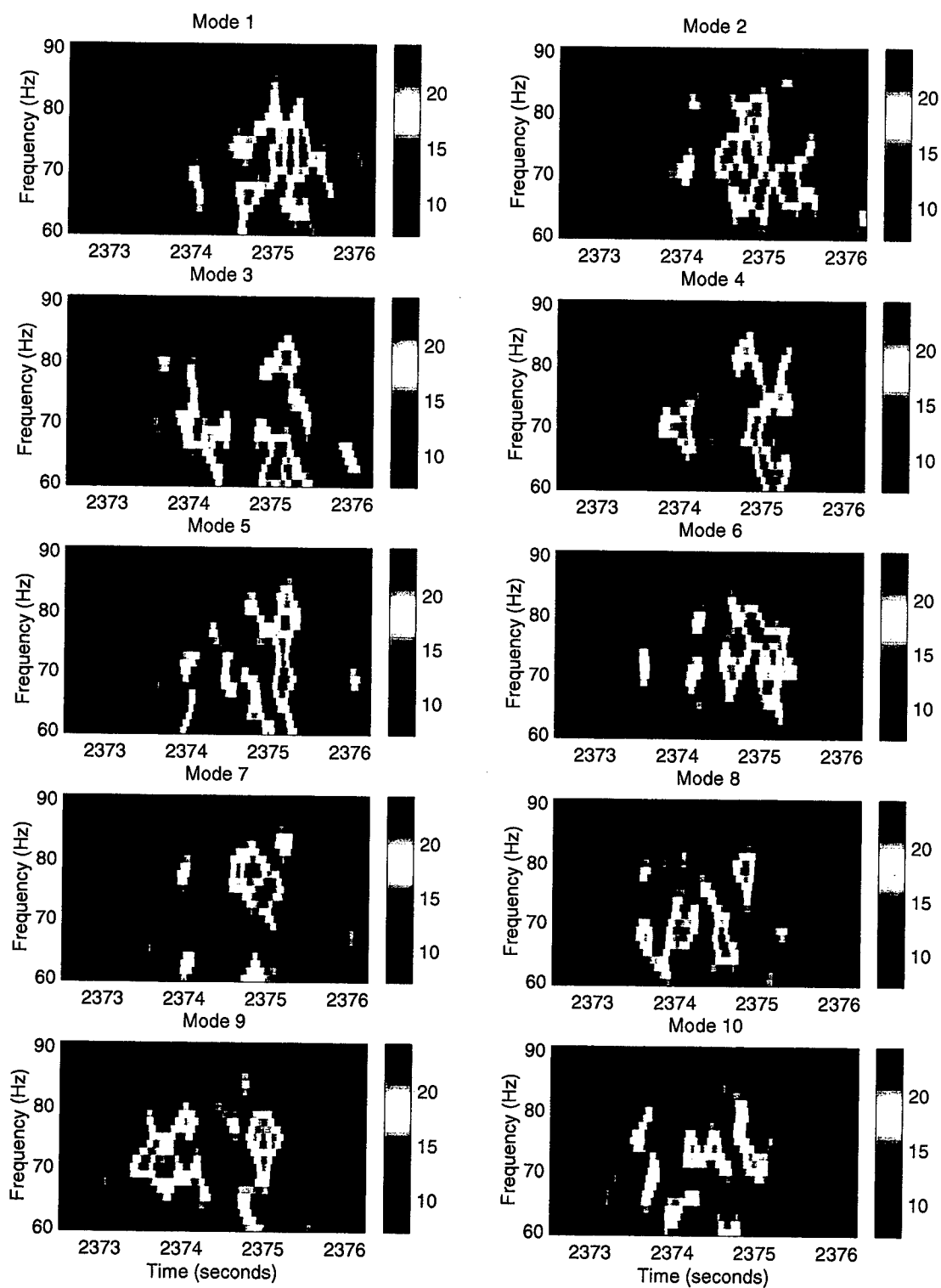


Figure 4-8: Frequency-stacked mode estimates for the ATOC reception in Fig. 4-5. Color scale is in dB.

phase characteristics arrive at the same time. The spectrum for the superposition of these signals may contain amplitude fades due to destructive interference. If the individual arrivals are temporally-resolvable using a short-time transform, then the characteristics for each path can be measured. In this case, the magnitude across frequency should not contain deep fades.

The STFT processor used on the ATOC data can begin to temporally resolve signals at a separation of 0.2 seconds (see discussion on page 69). Note that since bins with 2.5 Hz spacing are slightly correlated (due to the overlap of the bandpass filters associated with the STFT), signals must show coherence over bandwidths of greater than 5 Hz before it is clear that the coherence is due to the underlying arrival and not an artifact of processing. Although the plots in Fig. 4-8 indicate the presence of faded arrivals, they also contain some arrivals that extend over 5-10 Hz bandwidths. This suggests that the STFT processor may be resolving some individual multipaths.

4.3.2 Simulated Receptions

The previous section reviewed important characteristics of the mode arrival structure estimated from ATOC data. For comparison, this section considers two of the simulated receptions (described in Section 4.2). The first is for propagation through the Levitus background environment; the second includes internal-wave-induced sound speed perturbations.

Figure 4-6 shows the received time series for propagation through the background environment. Note that individual mode arrivals are evident in the pressure field *e.g.*, mode 2 is the strongest final arrival located at 2375 seconds. (Mode 1 is not strongly excited by a source located at 939.5 m depth.) Figure 4-9 displays the short-time Fourier mode estimates for the first 10 modes, indicating that these modes arrive in descending order. The solid black line on each of the frequency-stacked plots represents the adiabatic arrival times. Agreement between the adiabatic predictions

and the PE simulation without internal waves is quite good. While this does not prove that propagation through the Levitus background environment is adiabatic, it does demonstrate that, in the absence of internal waves, each of the first 10 modes is dominated by a single dispersive arrival.

In contrast to the background simulation, the results for the internal wave simulation show more complicated mode arrival patterns. Figure 4-7 is the pressure time series for the internal wave simulation, and Figure 4-10 displays the corresponding mode estimates. Similar to the ATOC data, the estimates for the perturbed environment contain multiple arrivals in each mode. Some of these arrivals also exhibit frequency-selective fading, and others appear to be coherent over bands on the order of 10 Hz.

To permit a comparison between experiment and simulation, Figure 4-11 shows the estimated spectra for modes 1 and 10 for the ATOC reception and the two simulated receptions. For reference, adiabatic travel time predictions for the California-Hawaii path are shown at the bottom. There is qualitative similarity between the mode estimates for the ATOC reception and the PE simulation containing internal waves, *i.e.*, both contain multipath arrivals and show evidence of frequency-selective fading. Although mode 10 starts arriving before mode 1 in both the ATOC data and the internal wave simulation, there is significant overlap of these two modes in time. This is in contrast to the background simulation and the adiabatic case where those two modes are temporally separated. Note that the ATOC data does show significantly more time-spread than the simulation.

The most striking disagreement between the PE simulations and the real data is that the simulations have a sharp cutoff around 2375 seconds (obvious in both the pressure time series and the mode estimates), but there is no discernible cutoff in the ATOC receptions. In the ATOC data, high energy arrivals occur before 2375.5 seconds, but the signal trails off with a series of lower energy peaks after that. Heaney has associated this "afterglow" in the arrival pattern with bottom interaction

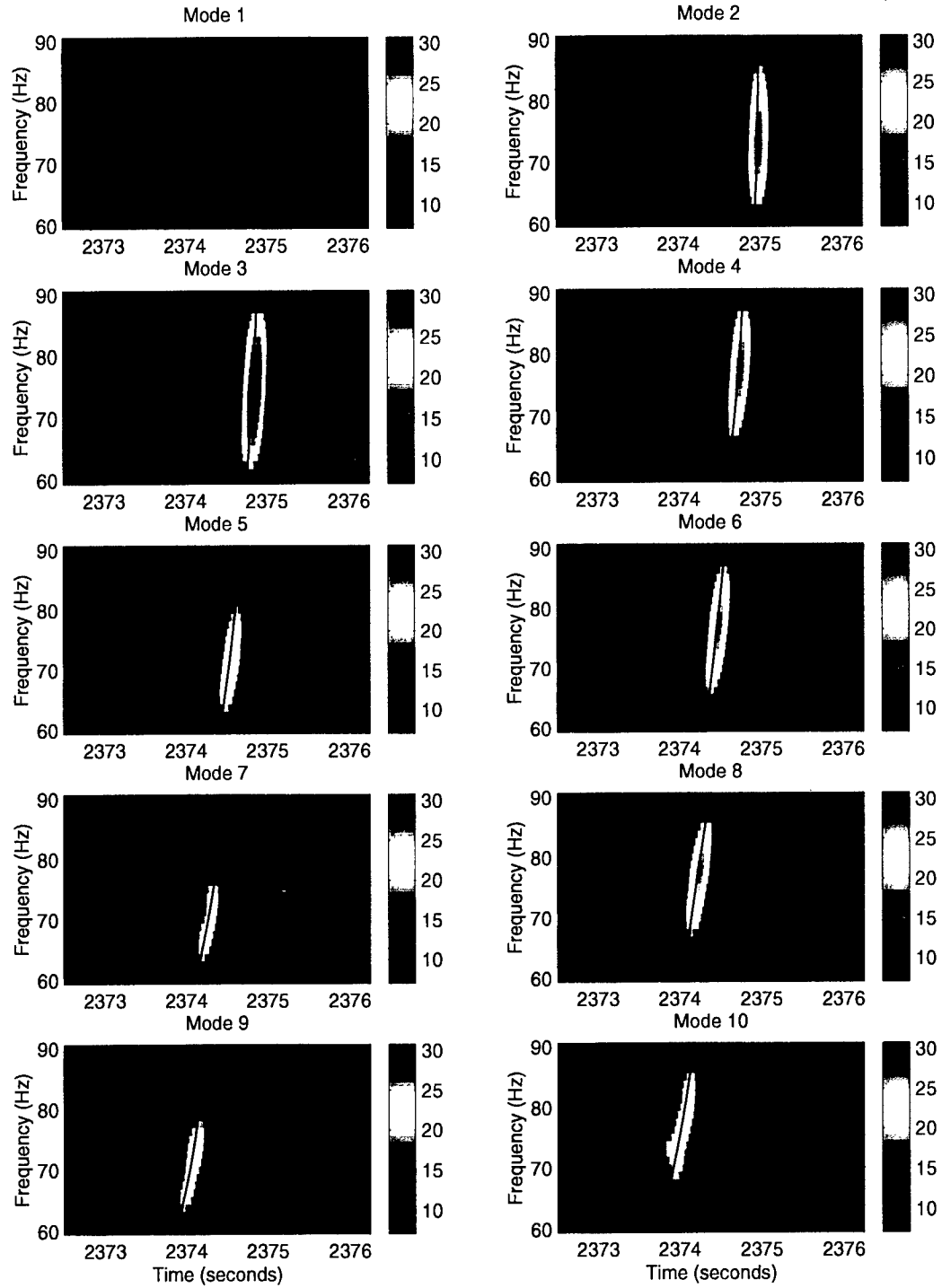


Figure 4-9: Frequency-stacked mode estimates for the PE simulation without internal waves in Fig. 4-6. Black lines in each subplot are the predicted arrival times based on adiabatic dispersion curves.

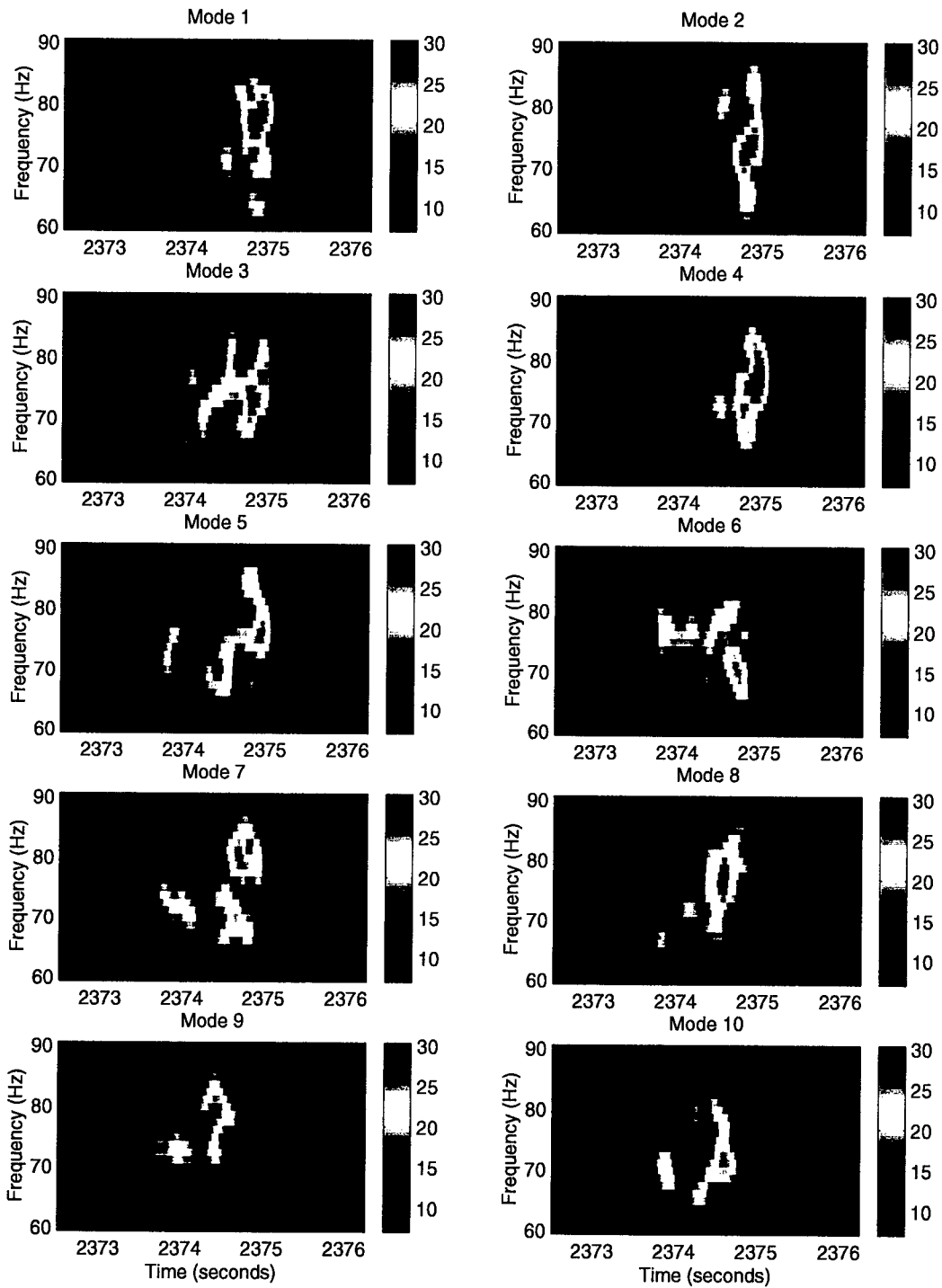


Figure 4-10: Frequency-stacked mode estimates for the PE simulation with internal waves in Fig. 4-7

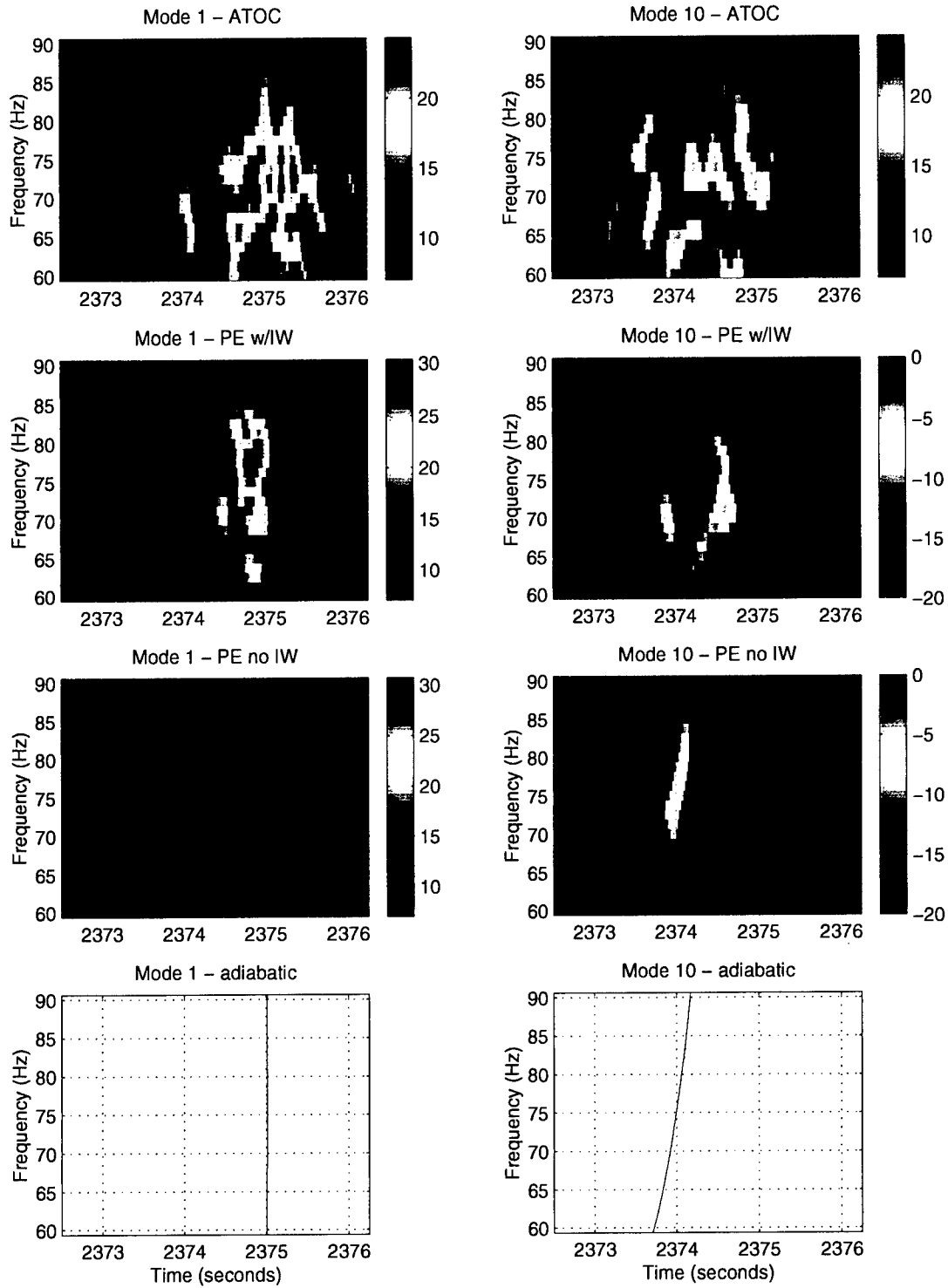


Figure 4-11: Comparison of ATOC data, PE simulations, and adiabatic predictions for modes 1 and 10.

near the source [53]. The next section considers the downslope propagation issue briefly.

4.3.3 Downslope Propagation Example

Although a thorough analysis of the downslope propagation problem is beyond the scope of this thesis, it is useful to consider one example which illustrates the effects of the slope on the initial excitation of the modes.

Figure 4-12 shows the actual bathymetry (dash-dot line) measured during source deployment, along with several approximations. The dotted line represents the bottom depths used in the simulations described in Section 4.2. Those ignore the slope entirely. As indicated by the figure, the seamount has very steep sides; at its steepest, the slope off Pioneer is approximately 20 degrees.

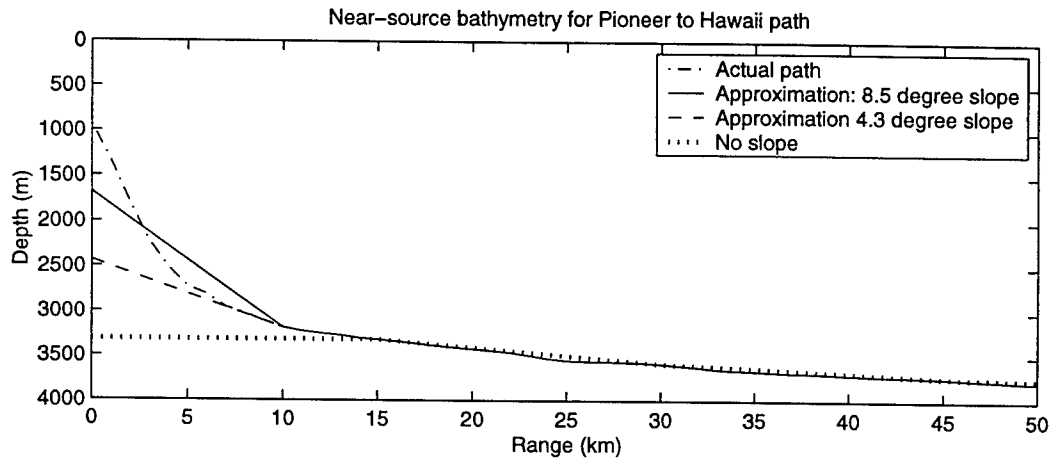


Figure 4-12: Bathymetry near the ATOC source at Pioneer Seamount

First consider a PE simulation with the actual sloping bottom near the source. The PE code does not handle shear waves, but a reasonable approximation (ignoring interface waves) for a solid bottom is to use a fluid bottom with a compressional speed equal to that of the shear parameters in the actual bottom [4]. For the ATOC source site, the bottom is basalt which has a shear speed of 2500 m/s, a density of 2.7 g/cm³, and an attenuation of 0.1 dB per wavelength. These are the bottom

parameters used in all of the simulations. Figure 4-13 compares the received pressure time series for the actual slope environment (top plot) and the no slope environment (bottom plot). These two simulations include the same internal wave perturbations. The plots are scaled to the peak pressure over the two receptions. Note that the

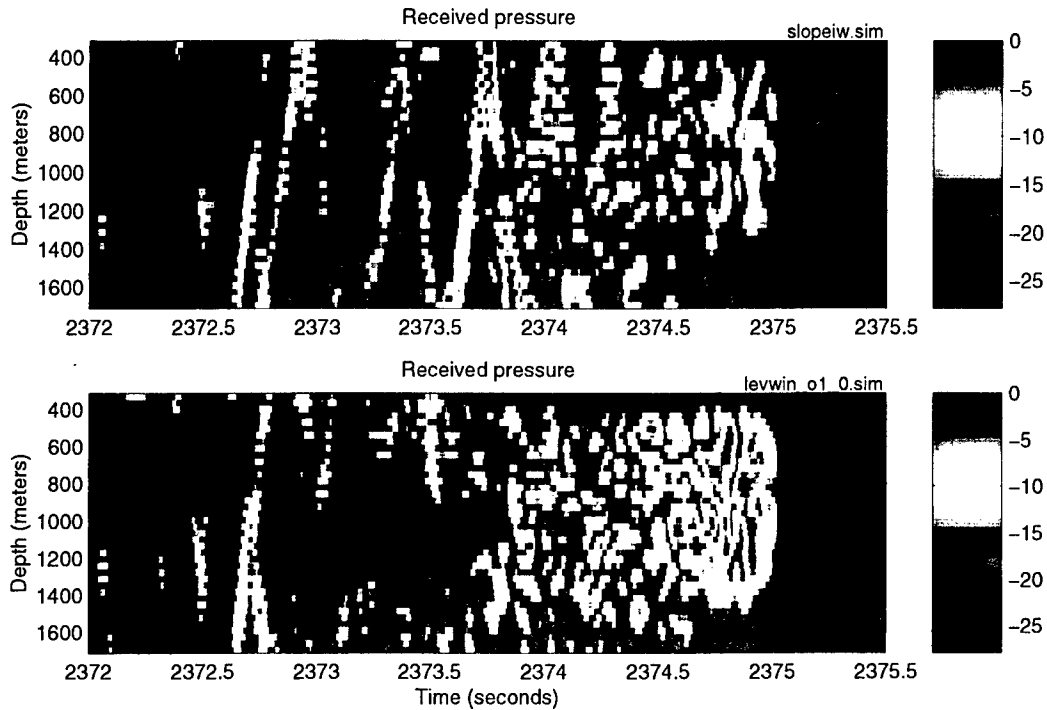


Figure 4-13: Comparison of propagation through the environment that includes the actual sloping bottom near the source (top plot) and the environment without the slope (bottom plot)

presence of a slope changes the final arrivals and adds approximately 1 second of additional, lower amplitude arrivals. Figure 4-14 illustrates the effects of the slope on the mode 1 and mode 10 estimates. Additional arrivals are added to both modes after 2375 seconds. There is also a strong arrival added in mode 10, before the cutoff. Although mode 1 does not appear to be as strongly affected as mode 10 in this case, it is unclear whether that would be true for other realizations of the internal wave field.

To get insights into what is happening near the source, consider a plot of the time series for the first 80 modes at a distance of 50 km from the array. Figure 4-15

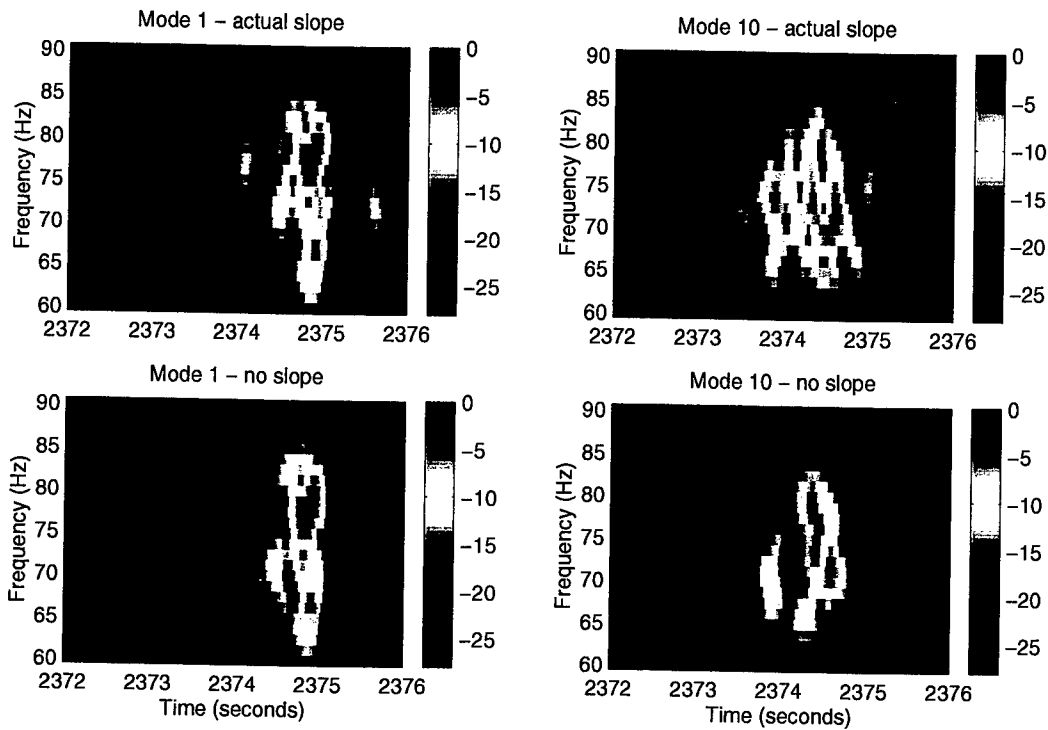


Figure 4-14: Comparison of arrivals in modes 1 and 10 for the sloping bottom (top plots) and the zero-slope approximation (bottom plots)

shows these results for the actual slope and for the 3 approximations to that slope in order to illustrate how steep the slope has to be to produce this effect. These are broadband time series computed by projecting onto the modes at 50 km at each frequency and then synthesizing a time series for each mode. The top plot shows the results for a simulation with the actual source bathymetry. In most of the modes below 60, the energy is concentrated in two pulses that are spaced approximately one second apart. This is in contrast to the no slope case, shown in the bottom plot, which contains only one dominant pulse in each mode. The two middle plots indicate how the second pulse fades out as the slope is decreased. The presence of the seamount clearly changes the mode excitation, but more work is needed to verify the actual mode scattering mechanisms down the slope that produce this effect. Heaney attributes the afterglow to a bottom bounce near the source [53]. It seems likely that the second pulse in the mode excitation is due to that bottom

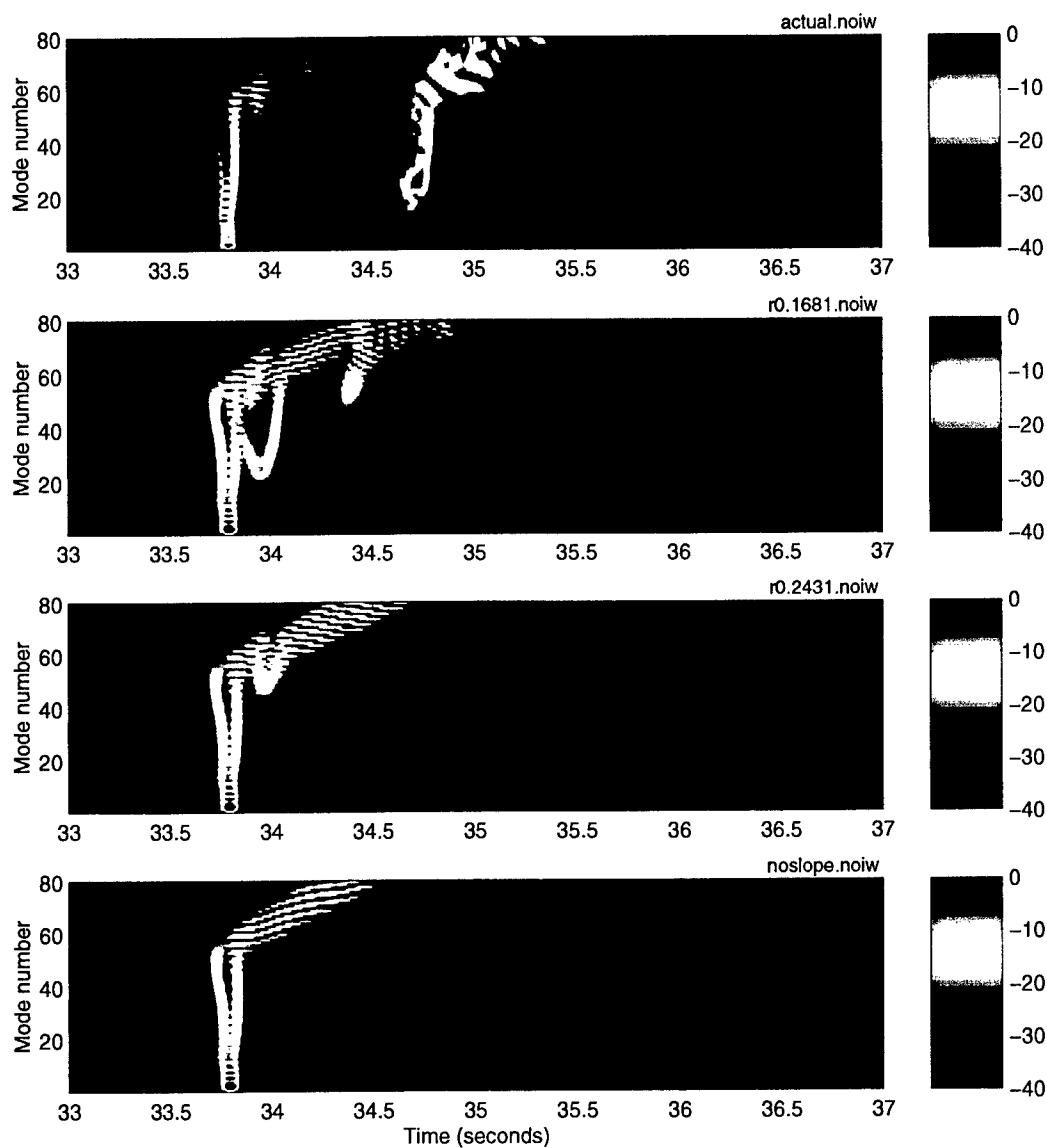


Figure 4-15: Comparison of the time series for the first 80 modes at 50 km range from the Pioneer Seamount source. Top plot is for the actual slope. Middle two plots are for the 8.5 degree and 4.3 degree approximations, respectively. The bottom plot corresponds to the no slope case.

bounce. Although more research is clearly required in this area, these simulation results indicate that the ATOC measurements may represent the response of the ocean channel to a superposition of two temporally-separated pulses rather than the response to a single pulse.

This section (4.3) has examined mode estimates for a single ATOC reception and compared them to results for a simulation through internal waves at 1/2 Garrett-Munk strength. The ATOC results and the simulation agree qualitatively, with both indicating that the mode signals at megameter ranges contain multiple, faded arrivals rather than the single dispersive arrivals that characterize adiabatic propagation. Although the similarities between experiment and simulation are encouraging, the ATOC data does show significantly more time-spread. The most striking disagreement between the simulated time series and the measured data is the sharp cutoff in the simulation, which was shown to be a consequence of ignoring the source bathymetry.

4.4 Temporal Variability

The purpose of this section is to consider the temporal variability of the mode arrivals. In previous work, Tang and Tappert obtained measurements of the temporal coherence of pulses propagating through internal waves in a shallow (200 m deep) water environment at ranges of 20 km. They considered the coherence times of pulses and did not address the issue of modes specifically. For deep water environments, Colosi *et al.* [71] (citing the work of Flatte and Stoughton [72]) indicate that acoustic coherence times are on the order of tens of minutes, whereas the coherence times for internal waves are on the order of hours. In analyzing data from the ATOC Engineering Test (range=3250 km), Worcester *et al.* used 12.7 minute coherent averages for the ray arrivals, since the SNR did not increase for longer averaging times. For that same data set, Colosi *et al.* concluded that time fluctuations in the wavefronts

show no coherence at 2 hour lag times. Note that in the works cited above, the focus was primarily on analyzing the ray arrivals, rather than the late-arriving modes. The rest of this section considers the temporal variations of the mode arrivals in ATOC.

Recall that for each source transmission, the ATOC VLA recorded 10 four-period averages of the 27.28 second pseudo-random sequence. The results discussed in Section 4.3.1 were computed using the first 4-period average of reception 363004024 at the Hawaii array. Figure 4-16 compares mode estimates for the first 4-period average and the last 4-period average for that reception. The top plots are the estimated spectra for modes 1 and 10 of the first average in the transmission and the bottom plots correspond to the last average. Note that the time difference between the end of the first reception and the start of the tenth is approximately 14.5 minutes. The plot clearly demonstrates that the mode signals change significantly over that time interval: some arrivals drop out entirely, and new arrivals emerge.

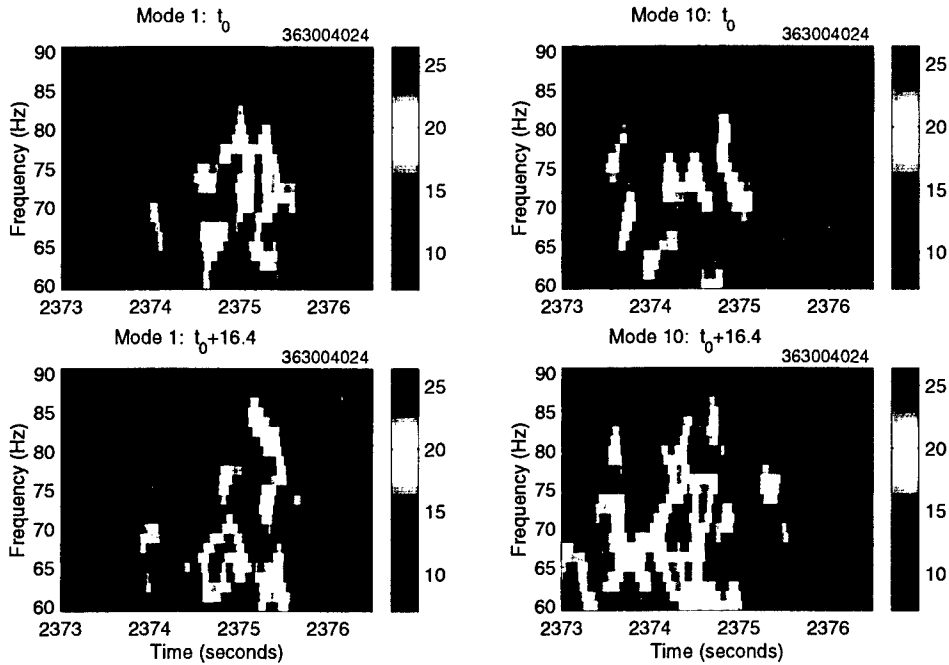


Figure 4-16: Comparison of modes 1 and 10 for the first (top plots) and last (bottom plots) periods of a source transmission

For comparison, consider the results of PE simulations that take into account

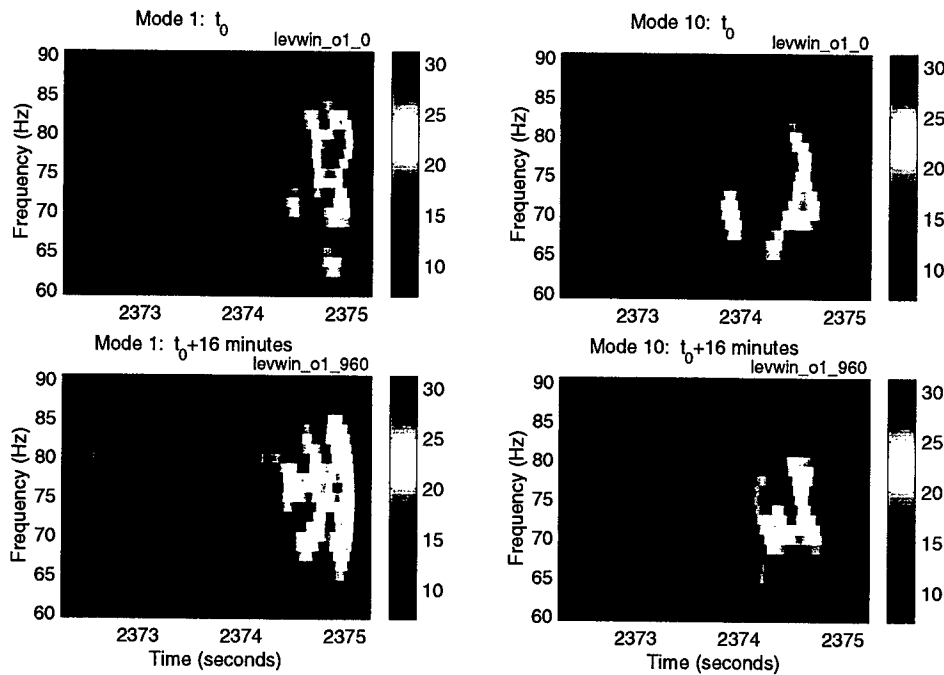


Figure 4-17: Comparison of modes 1 and 10 for realizations of a time-varying internal wave environment. The lag time between the top and bottom plots is 16 minutes.

time variations of the internal wave field. Using Colosi and Brown's approach, a realization of the time-varying internal wave field was generated for a nominal time t_0 , and for $t_0 + 16$ minutes. Fig. 4-17 shows the estimates for modes 1 and 10 that result from these simulations. These plots demonstrate fade-ins and fade-outs that are similar to those seen in the ATOC data.

Based on the single realizations of the ATOC data and the simulated data shown above, the low order mode arrivals fluctuate over time intervals on the order of minutes. The following approach was used to obtain a measure of the average coherence time for each mode. First, correlation coefficients were computed at a set of 10 lags for the received signals in a particular mode, corresponding to the 10 four-period averages. Note that the time interval used for these calculations was 2373 seconds to 2376 seconds, where the mode arrivals are concentrated. These correlation coefficients were then averaged over 96 ATOC receptions (from yearday 363 to yearday 435). The results are shown in Figure 4-18. The left plot in the figure shows the

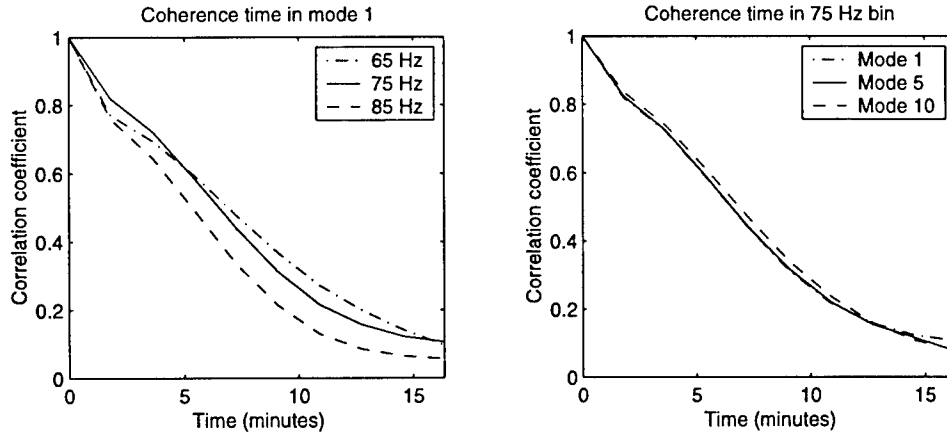


Figure 4-18: Temporal coherence as a function of frequency for mode 1 (left plot) and as a function of mode number for the 75 Hz bin (right plot). These results were obtained by averaging across 96 receptions (yeardays 363-435).

temporal coherence of mode 1 for three different frequencies. There does appear to be some mild frequency dependence, with mode 1 in the 65 Hz bin being more correlated than the same mode at 85 Hz. For mode 1, correlation decreases to a level of 0.5 between 6 and 8 minutes. The right plot in the figure shows coherence as a function of mode number for the 75 Hz bin. Based on these results, temporal coherence is not a function of mode number, which is not surprising given the amount of mode coupling.

The above calculations provide a measure of the coherence time of the whole signal in a particular mode, *i.e.*, all the multipath arrivals. An interesting question to ask is whether some peaks are more stable than others across the 18.2 minute transmission interval. Figure 4-19 illustrates how mode signals in the 75 Hz bin vary over the 18.2 minutes. The plots are stacks of the received signals in mode 1 (top) and mode 10 (bottom) at successive 1.82 minute lags. Some of the peaks are consistent across the full transmission interval, while others fade out suddenly, *e.g.*, the mode 1 arrival at 2375 seconds that drops out around 12 minutes. Again, it is interesting to compare these results to PE simulations involving time-varying internal wave fields. For these results, the internal wave sound speed perturbations were computed at

4-minute intervals between 0 and 20 minutes. Figure 4-20 shows the resulting stacks for modes 1 and 6 for the 75 Hz bin. This data confirms that the PE simulations with internal waves at 1/2 Garrett Munk strength result in qualitatively similar time variations of the modes.

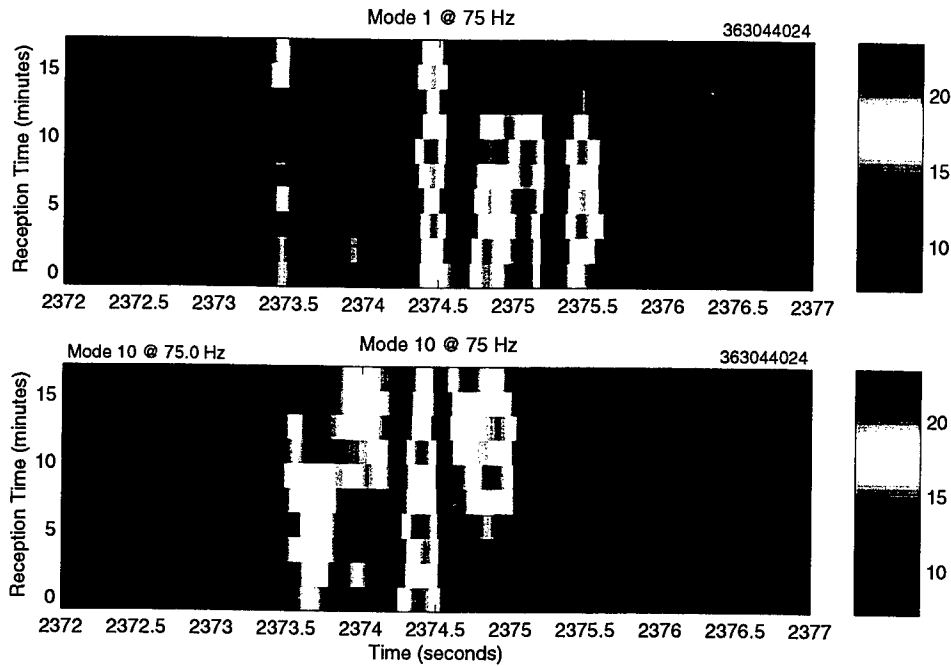


Figure 4-19: Variability of modes 1 and 10 across a single transmission (18.2 minutes) in the 75 Hz bin

This section has shown that the mode arrival structure varies considerably over intervals on the order of 20 minutes. The following section considers four hour intervals and asks whether averaging over multiple transmissions can be used to obtain insight into mode behavior.

4.5 Mode Statistics

On days that the ATOC source was on there were transmissions at 4-hour intervals. Given the large amount of variability in the mode signals over a 20-minute period, it is expected that the transmissions at four-hour intervals will sample very different re-

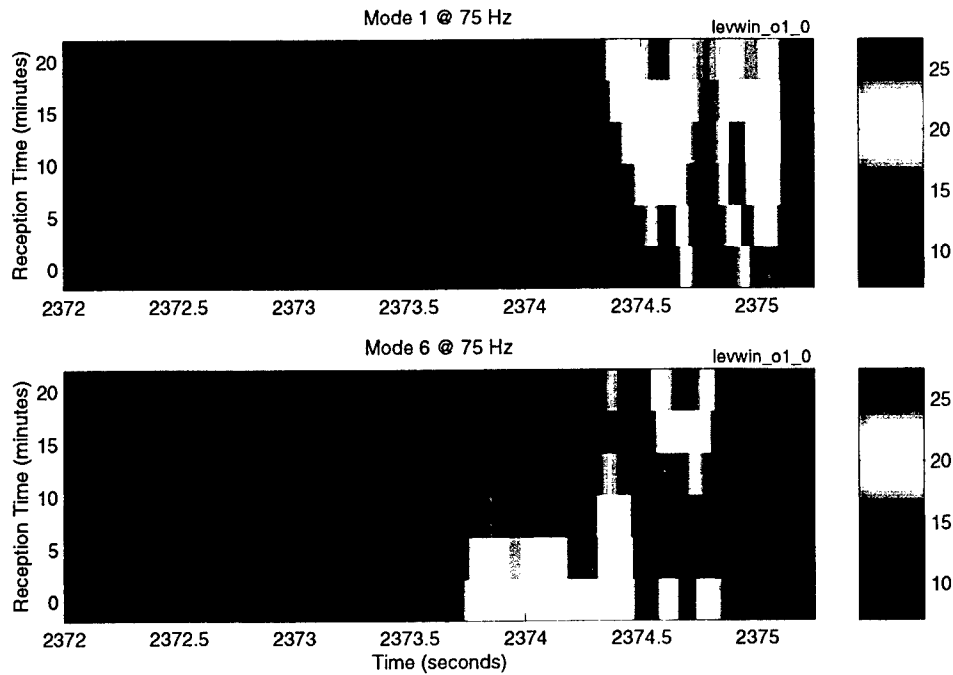


Figure 4-20: Variability of modes 1 and 6 for the simulated data in the 75 Hz bin, calculated at 4 minute intervals.

alizations of the internal wave field. Such behavior can be seen in Figure 4-21, which shows the short-time spectra for mode 1 (the first 4-period average) for three consecutive transmissions. Clearly, the mode arrival structure is significantly different at 4-hour lags. Although all arrivals for all three receptions shown are approximately centered around 2375 seconds, and there is some consistency in the weaker peaks (*e.g.*, the faded arrival around 2376 seconds), the strong arrivals do not occur in the same places for each reception, and overall the interference pattern is quite different.

To get an idea of how the peak arrivals are distributed as a function of time, consider the histograms shown in Figure 4-22. These plots were compiled from the first 96 good receptions recorded on yeardays 363 through 436, using a detection threshold of 12 dB above the estimated noise level for each mode. These results confirm that there is not a dominant arrival time in each mode; rather, the peaks are distributed between 2373 seconds and 2376 seconds for all of the modes. Note

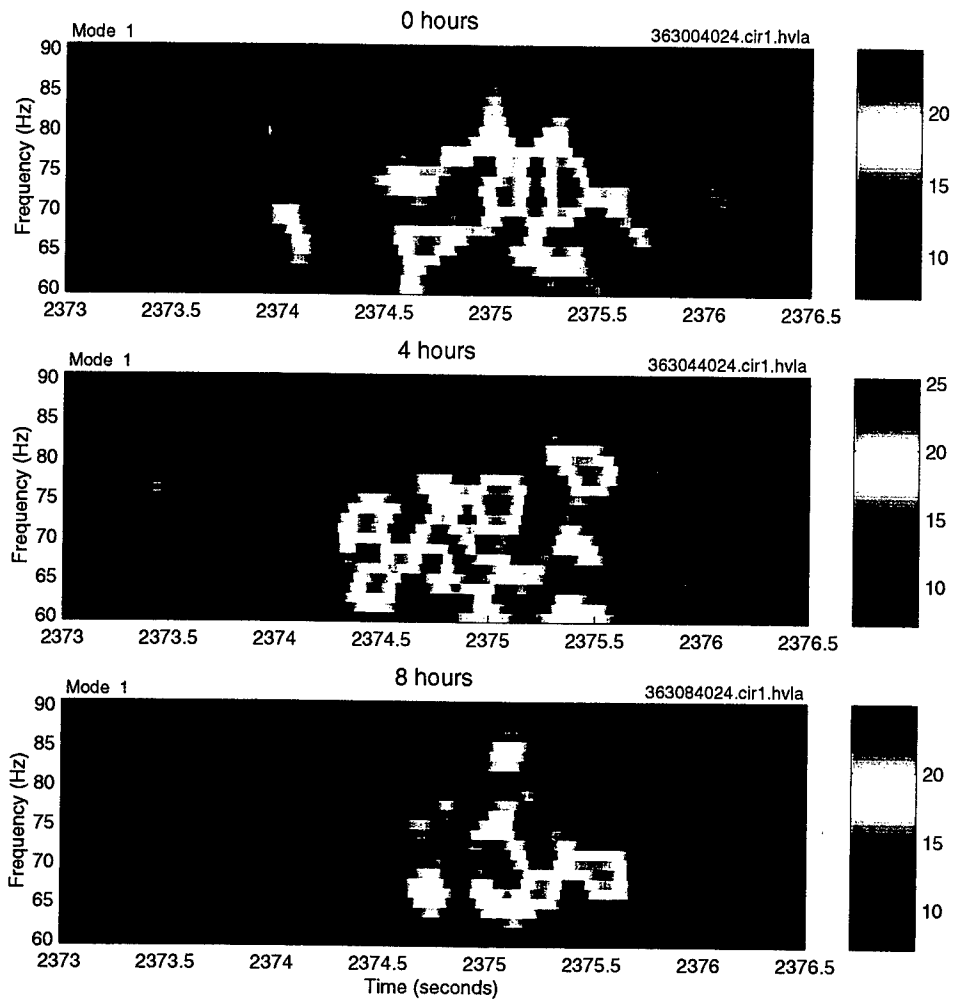


Figure 4-21: Mode 1 in ATOC receptions at 4-hour intervals

that the distribution of the higher modes (*e.g.*, mode 10) is skewed towards the early part of the 3-second interval while the low modes are concentrated towards the latter part of the interval. This is consistent with the deep water dispersion, where higher modes arrive first.

Given the amount of variability in the arrival structure, does averaging over multiple transmissions reveal consistent features in the mode signals? To answer this question, it is useful to consider several statistics: leading edge, falling edge, and centroid. Note that the leading and falling edges are (respectively) the first and last time indices where the complex envelope of the mode estimate exceeds a threshold.

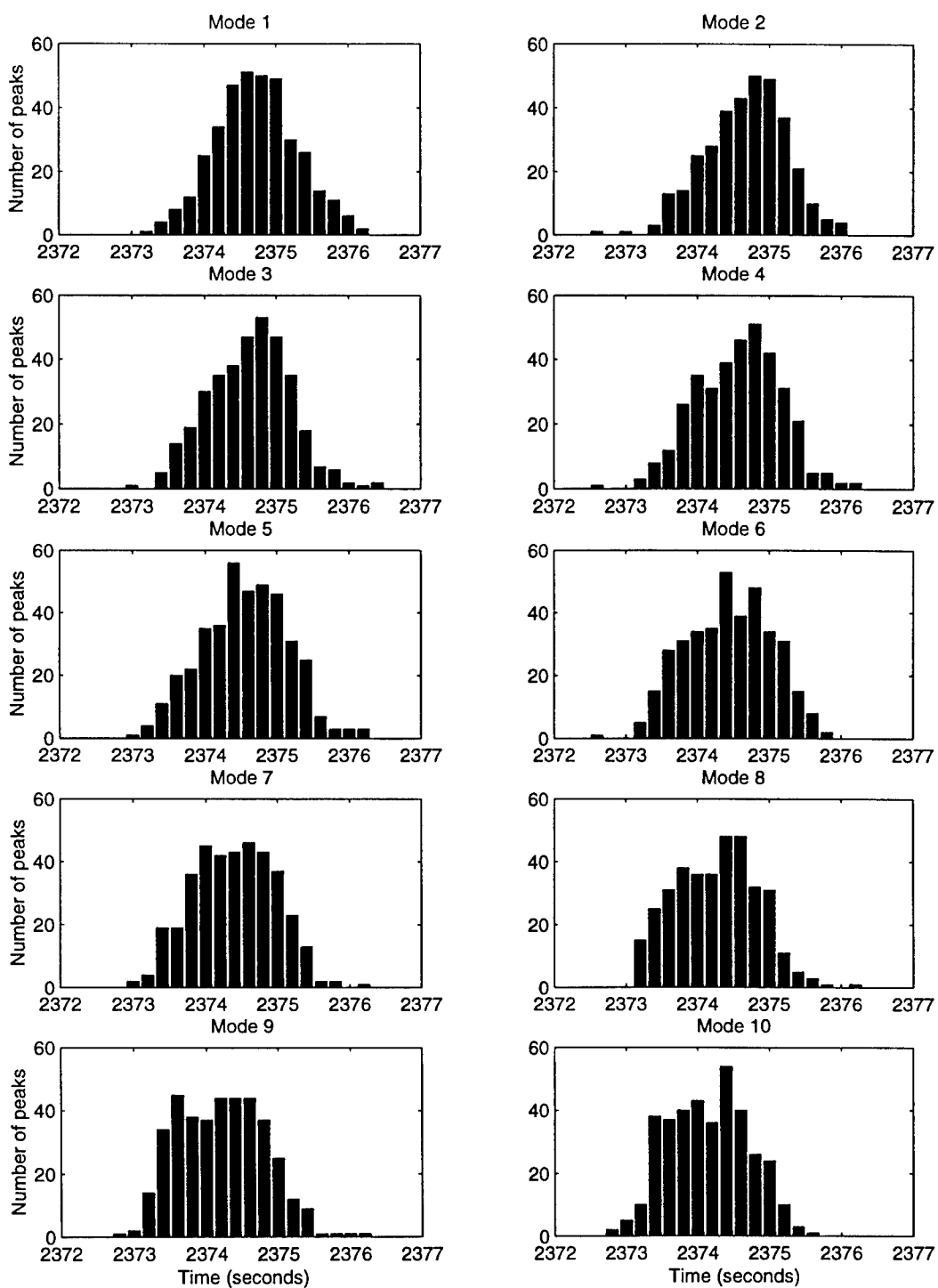


Figure 4-22: Histogram of peak arrivals in the 75 Hz bin. Threshold for peak detection was set at 12 dB above the noise floor. These results were computed from the first 96 good receptions (yeardays 363 to 436).

The centroid is defined to be the center of mass of the portion of the complex envelope that is higher than the threshold value. For all of the results presented below, the threshold was set at 12 dB above the noise floor in each mode. In order to examine how these statistics vary as a function of time over the course of the experiment, the ATOC receptions were divided into 13 groups as indicated in Fig. 4-1.

Figure 4-23 shows the leading edge, falling edge, and centroid in the 75 Hz bin for the first group of receptions. This group consists of 20 receptions, each containing 10 four-period averages. The data is plotted so that each whole number on the x-axis represents the start of a set of 4-period averages. As this figure indicates, the

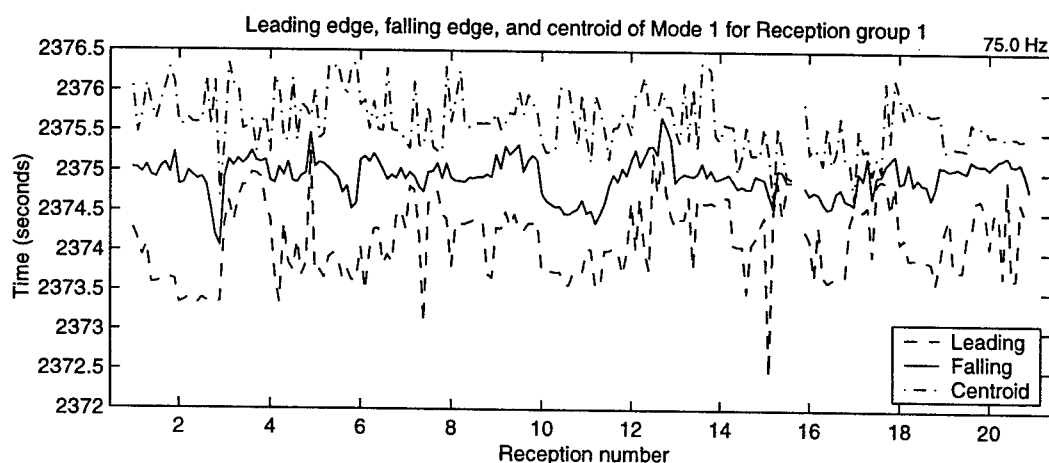


Figure 4-23: Leading edge, falling edge, and centroid in the 75 Hz bin for the first 20 ATOC receptions, each consisting of 10 four-period averages.

three statistics of interest can fluctuate significantly over one source transmission (18.2 minutes) as arrivals fade in and out.

Figure 4-24 shows the results of averaging over all the receptions in the first group (a total of 200³) to obtain the leading and falling edges as a function of frequency for the first 10 modes. For reference, the figure also includes the average leading and falling edges for the mode estimates of 10 simulated receptions. The

³Note that the average may contain less than 200 points since there are a few receptions where no part of the estimate exceeds the detection threshold.

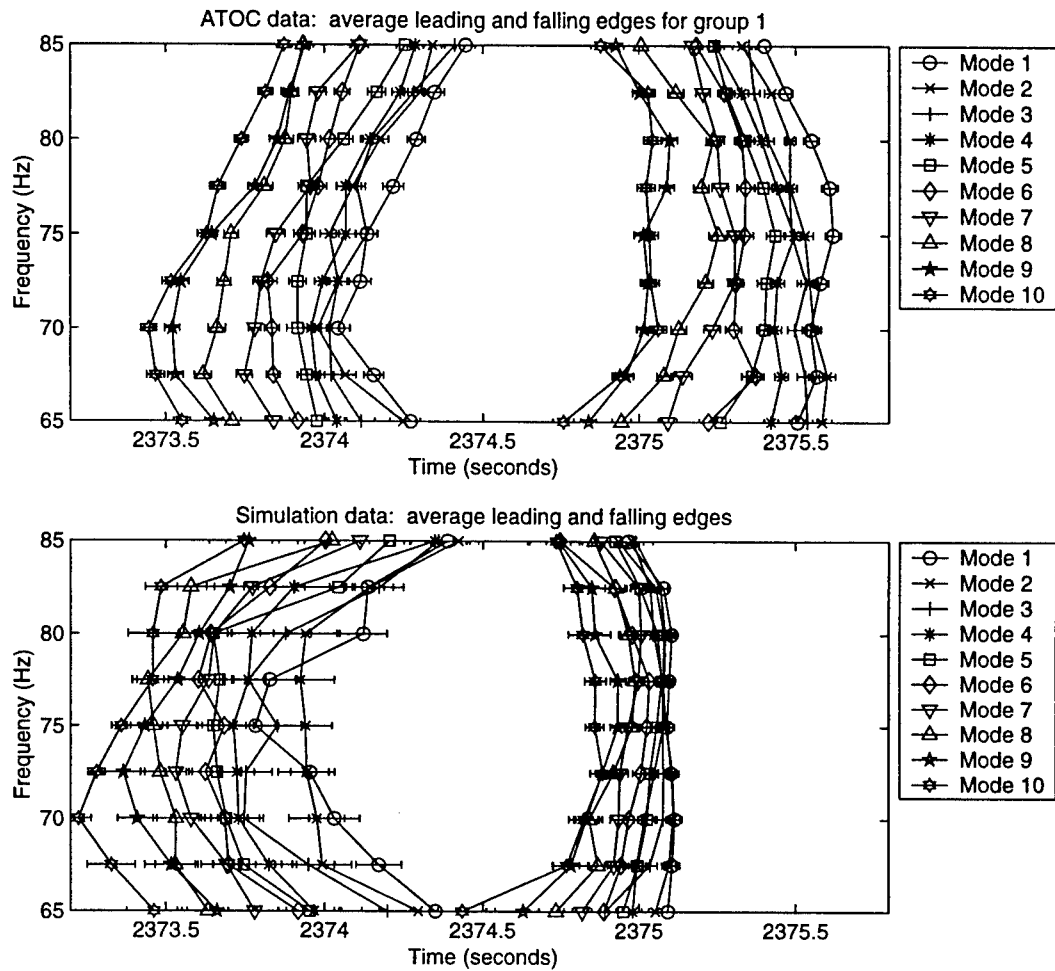


Figure 4-24: Comparison of average leading and falling edges for the first group of ATOC receptions and the simulated data set

error bars on these plots (and all subsequent ones) represent the estimated RMS error, *i.e.*, the sample standard deviation divided by the square root of the number of samples included in the average. The ATOC statistics reveal several significant features. First, the average spread between leading and falling edges is on the order of 1.5 seconds. Second, the high modes have earlier arrival times, while low modes have later arrival times, as would be expected in a deep water channel. Although there is some crossover between neighboring modes, the leading and falling edges show that there are statistically significant differences in arrival time among the modes, *e.g.*, compare modes 1 and 10. Finally, note that the plot indicates that the signals at the center frequency (75 Hz) are more spread than those at either end of the band. This effect may be partially due to the fact that the same detection threshold is used for all frequency bins, while the source spectrum rolls off as a function of frequency.

Since the simulated data is averaged over only ten receptions, the resulting curves in Fig. 4-24 are not as smooth as the ATOC data and the error bars are larger. Nevertheless, the simulated data is comparable to the real data in two important respects: the leading edges show similar behavior (as a function of frequency) to the ATOC data, and the arrival times are also comparable. Unlike the falling edges in the ATOC data, however, the falling edges in the simulated data are much more concentrated. This sudden cutoff has been noted previously and is likely the result of the lack of modeling of the downslope propagation in the simulation.

Now consider the average centroid statistics as a function of frequency. Figure 4-25 compares the average centroid locations for the first group of ATOC receptions with the average centroids for the simulated receptions. Predicted adiabatic travel times are included for reference. The experimental data centroid data shows the modes arriving in descending order (though there is some crossover among nearest-neighbors). For the highest modes, there is a slight trend across frequency: the higher frequencies arrive later, as would be expected in deep water. The simulated data show good agreement: the centroids extend over approximately the same time interval

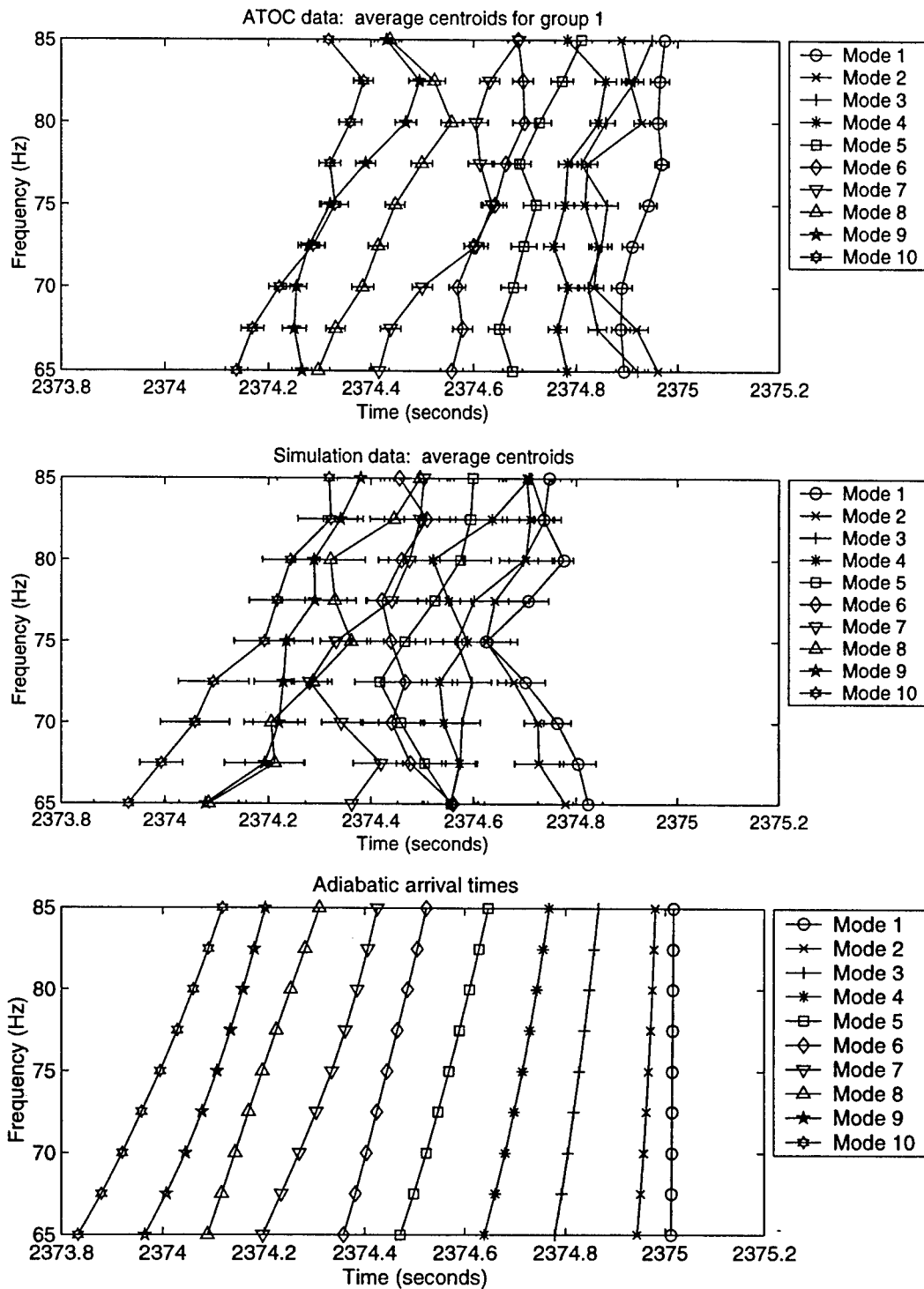


Figure 4-25: Comparison of average centroid locations for the first group of ATOC receptions, the simulated receptions, and adiabatic predictions

(≈ 0.8 seconds), and there is again a slight trend of increasing arrival time with increasing frequency in the higher modes. This supports the idea that $1/2$ Garrett-Munk strength is appropriate. The key difference between the ATOC data and the simulated data in Figure 4-25 is a shift in the mean arrival times: the centroids for the first group of ATOC data occur approximately 0.2 seconds later than the centroids of the simulated receptions. Comparing the ATOC and simulated data to the predicted adiabatic arrival times, one key difference is evident: the interval over which the arrival times are spread is much longer in the adiabatic case. This is expected because mode scattering accounts for the concentration in the ATOC and simulated data.

Figures 4-26 and 4-27 show the centroids as a function of frequency for the 13 groups of receptions defined in Figure 4-1. These receptions were taken over a period of approximately 5 months, between the end of December of 1995 and May of 1996. The centroids in each of the groups show similar behavior as a function of frequency, but there is clearly a drift in the arrival times from one set of receptions to the next. The drift in arrival times is more obvious in the plot of Figure 4-28, which shows the average centroids of first 10 modes at 75 Hz as a function of yearday. Note that the minimum travel time for all of the modes occurs around yearday 427, which corresponds to the beginning of March, 1996. The trend of decreasing mode arrival time from the start of the experiment until March and increasing afterwards agrees with the trend observed in the ray arrivals for the Hawaii VLA [73]. The difference in the arrival times between the first group of receptions (yearday 363) and the sixth group of receptions (yearday 427) is between 0.3 and 0.5 seconds for the first 10 modes. A T-test confirms that these time differences are statistically significant (using a significance level of 0.01). Based on the 1998 Science article by the ATOC Consortium [73], the ray arrivals exhibit somewhat smaller time shifts on the order of 0.25 seconds over that same period. The Science article notes that the trend observed at the Hawaii array is not in agreement with the expected seasonal

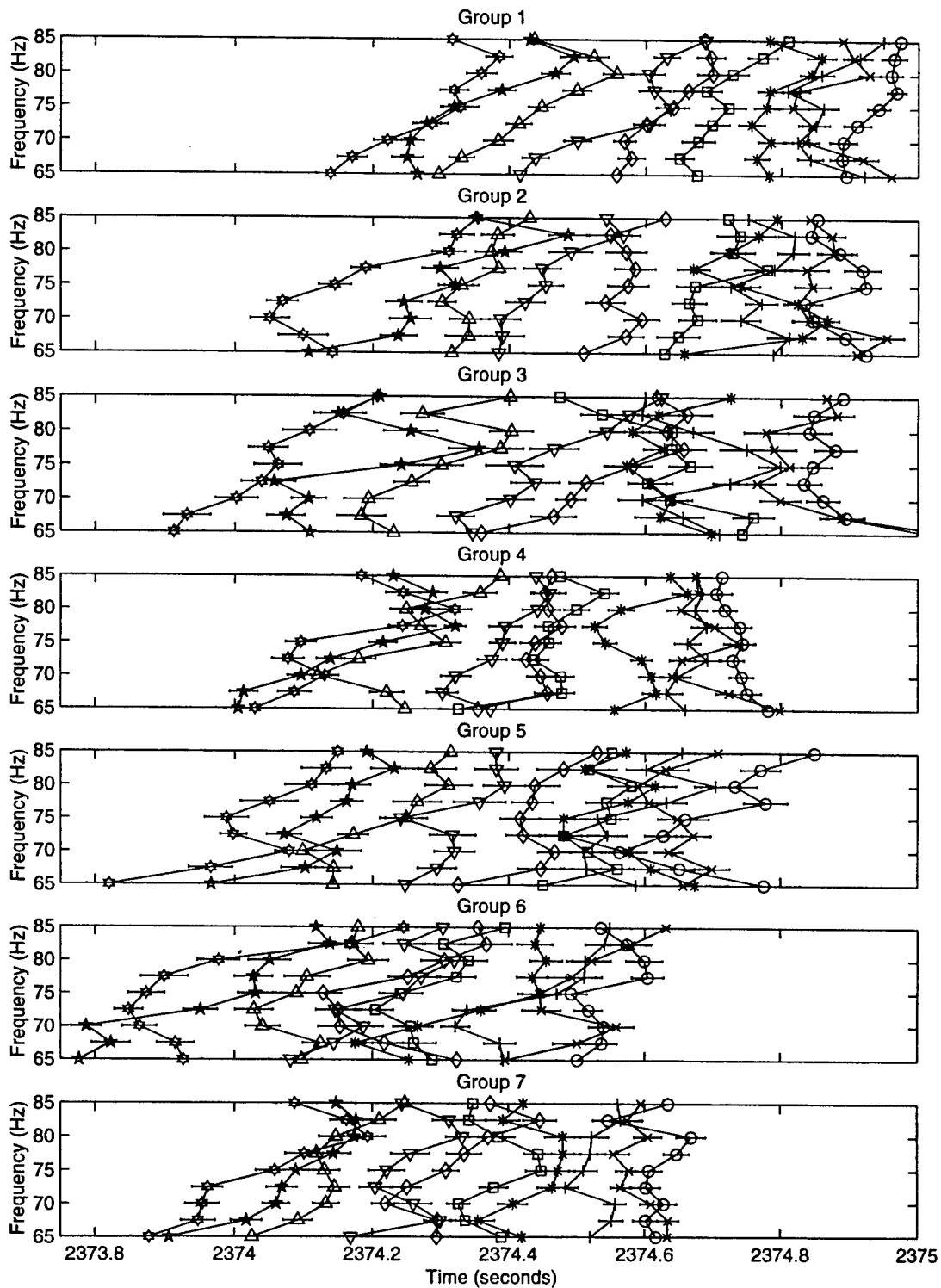


Figure 4-26: Average centroids as a function of frequency for the first 7 groups of ATOC receptions. Legend is identical to that shown in Fig. 4-25. See Fig. 4-1 for a definition of the groups.

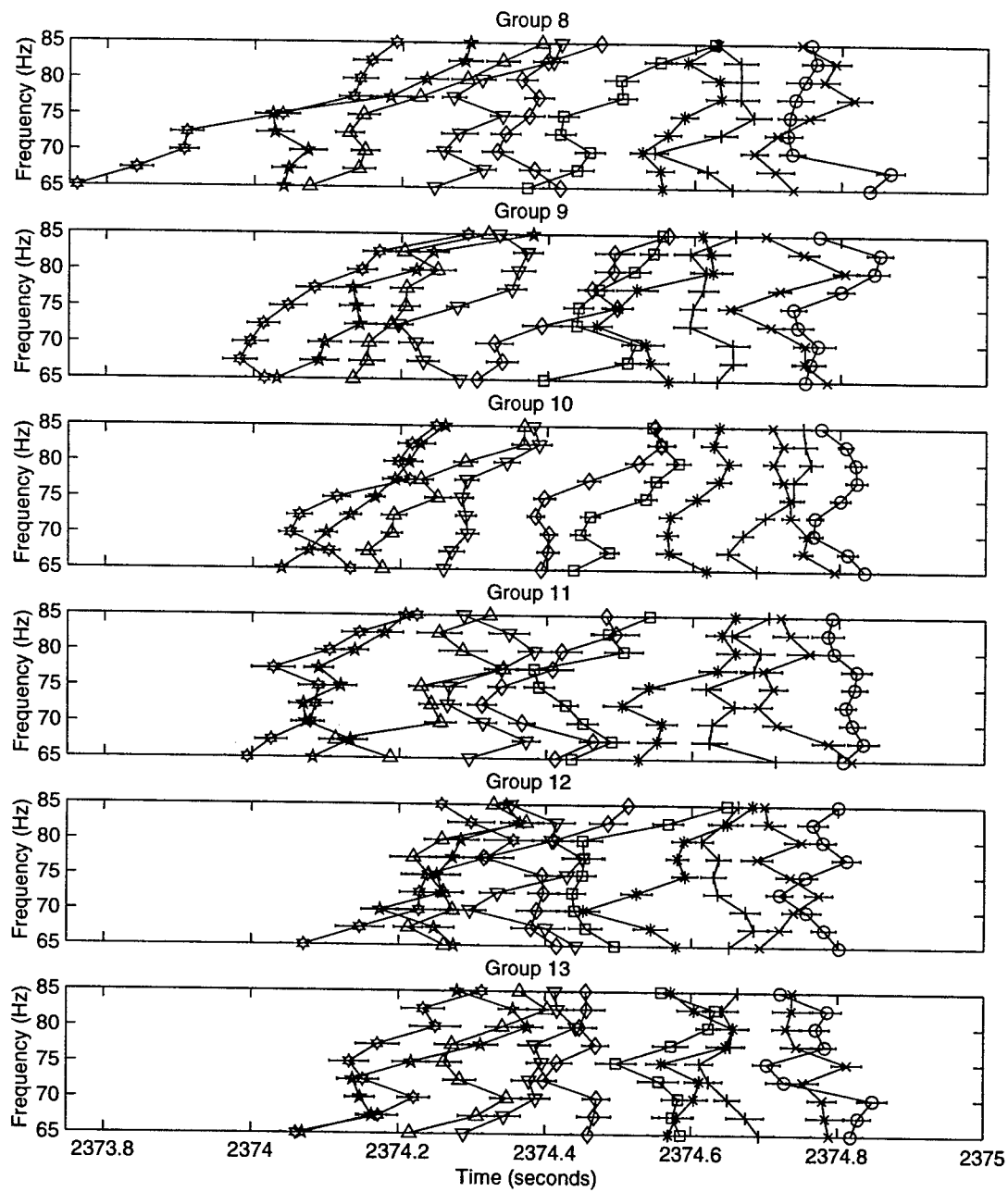


Figure 4-27: Average centroids as a function of frequency for groups 8-13 of the ATOC receptions. Legend is identical to that shown in Fig. 4-25. See Fig. 4-1 for a definition of the groups.

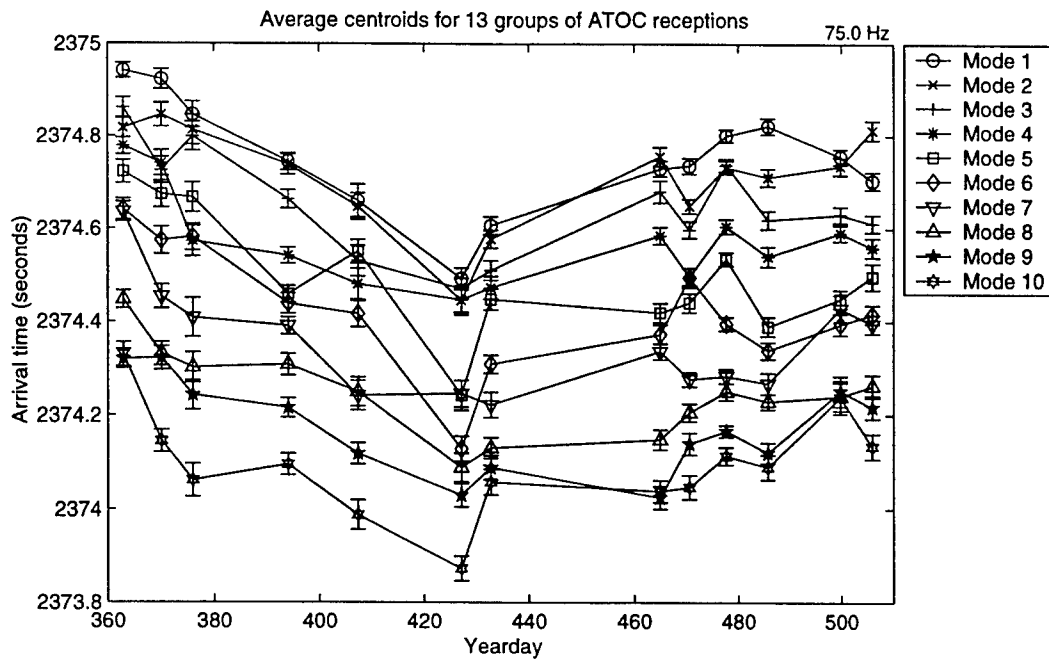


Figure 4-28: Average centroids in the 75 Hz bin for modes 1-10 as a function of yearday

trend (which would have shown increasing travel times in winter and decreasing in the summer) and postulates that this is due to a subsurface warming near the receiver that offsets the winter surface cooling layer near the source.

The trend in arrival times as a function of yearday is apparent in the falling edges of the modes, but is not as evident in the leading edge statistic. Figure 4-29 illustrates this point using mode 1 in the 75 Hz bin as an example. These curves are representative of the results for other low modes. Note that the falling edge shows a decrease in arrival time from January to March that correlates well with the centroid data. The maximum shift in the mean falling edge time is also 0.45 seconds. While the leading edge data show a significant decrease in arrival time for the set of receptions around yearday 427, there is no obvious downward trend in the first five groups of receptions as there is in the centroid and falling edge statistics.

It is important to consider the errors associated with these statistics. For the centroids and falling edges, Figure 4-30 shows the average (over the 13 groups of

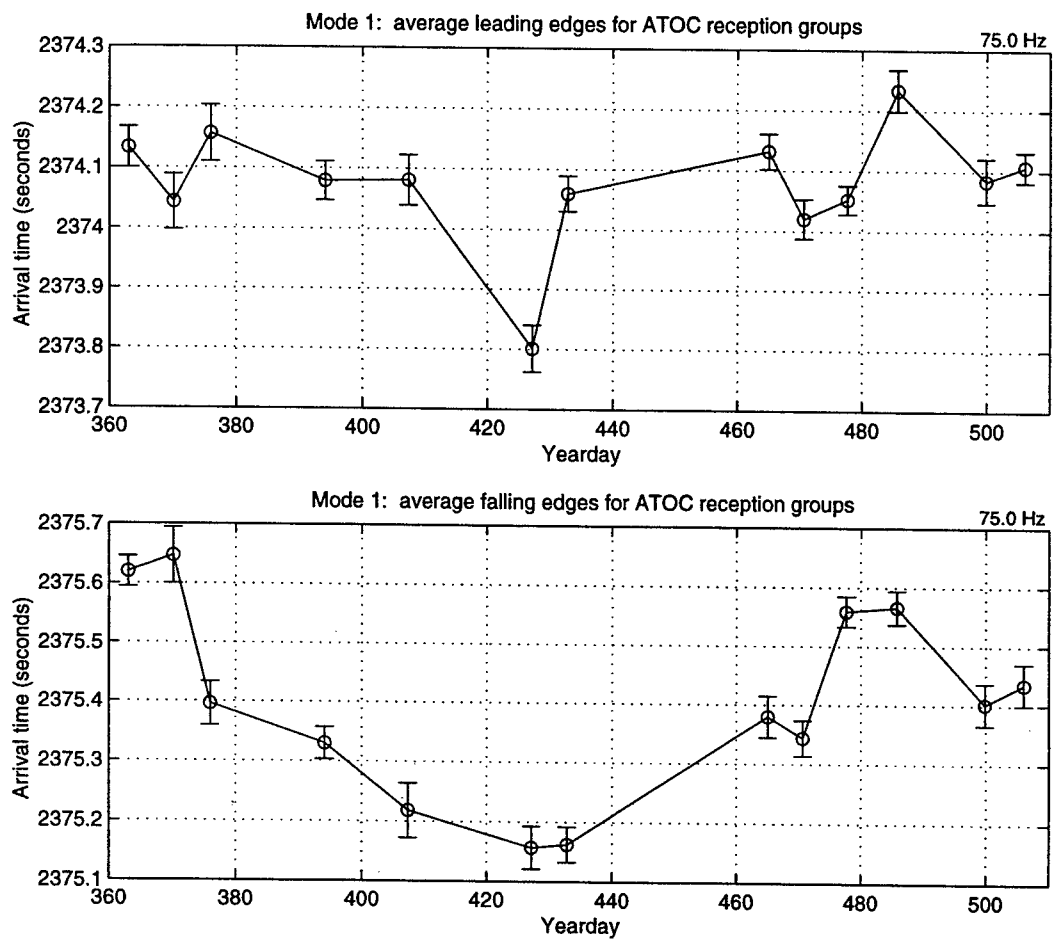


Figure 4-29: Average leading and falling edges for mode 1 in the 75 Hz bin as a function of yearday

receptions) RMS error at 75 Hz for the first 10 modes. The average RMS error for the centroids is between 20-27 milliseconds, with a slight trend of increasing error with mode number. Error for the falling edge statistics tends to be larger (29-34 milliseconds) and does not exhibit a mode-dependent trend. Note that the

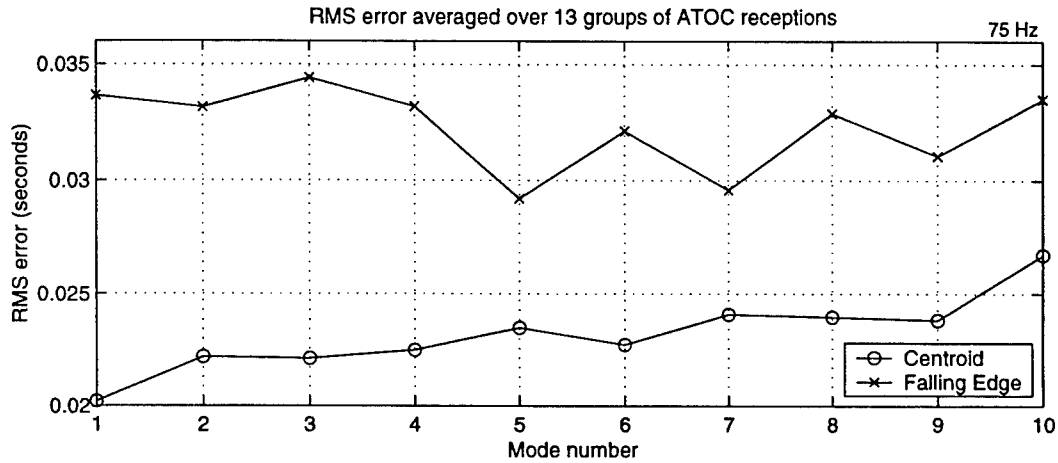


Figure 4-30: Average of the RMS error over 13 groups of receptions as a function of mode number. Results are shown for the centroids and the falling edges of the 75 Hz bin.

order of magnitude of these errors is comparable to the measured fluctuations of the identifiable ray arrivals (11-19 ms) and the pulse termination (22 ms) [71].

4.6 Summary

This chapter has provided the first detailed look at the low-mode signals in the ATOC receptions at Hawaii. While much work remains to be done, some important conclusions about the nature of the low-mode arrivals can be drawn from this analysis.

The first observation is that modes 1-10 at 3515 km range contain multiple arrivals, rather than the single, dispersive arrivals that are associated with adiabatic propagation. This has important implications for matched field processing

and tomography because the problem of associating a signal with a particular path through the ocean becomes difficult.

Second, many of the arrivals in the data show frequency-selective fading due to the destructive interference of overlapping multipaths. There is evidence of frequency-coherent arrivals in the ATOC receptions, suggesting that the STFT processor may be resolving some individual paths. More work is necessary to parameterize the frequency-selectivity of the channel and to determine how often coherent arrivals can be expected.

Third, the modal multipath structure exhibits significant temporal variability. Average coherence times⁴ for the modes are on the order of 6-8 minutes, which is less than the 18 minute source transmission time. Coherence appears to be a mild function of frequency, but not a function of mode number for the first 10 modes. Some arrivals are temporally stable over a 20-minute reception, but are not usually detectable in the next reception, four hours later. The results of this chapter indicate that each transmission at 4-hour intervals essentially samples a different realization of the internal wave field.

Fourth, despite the complexity of the mode arrival structure, averaging over source transmissions at successive 4-hour intervals reveals some of the expected dispersion characteristics of a deep water channel. An analysis of three statistics (leading edge, falling edge, and centroid) suggests that the modes retain some travel time information at megameter ranges. The results of this chapter indicate that there were statistically significant changes in the centroid and falling edge arrival times over the 5 months of data analyzed for the Hawaii VLA. On average⁵, the mode arrival times decrease by 0.4 seconds between December and March, and then increase by 0.2 seconds between March and May. The RMS errors in these centroid measurements are 20-30 ms on average, on the same order as fluctuations of ray

⁴*i.e.*, the time at which the correlation coefficient is approximately 0.5

⁵Averaging over the modes in the 75 Hz bin

arrivals and pulse termination observed by other researchers.

Comparisons of the ATOC receptions to PE simulations through internal wave fields at $1/2$ Garrett-Munk strength support these conclusions. Both the nature of the frequency-selective fading and the time variations of the modes in the simulated data qualitatively agree with the experimental data. Furthermore, the centroid statistics demonstrate, in a more quantitative way, that the simulations using $1/2$ GM levels are in agreement with the data. This is an important conclusion because studies of the ray-like arrivals indicate internal wave strengths on the order of $1/2$ GM.

One major discrepancy between the simulations and the ATOC data is that the simulations contain a sharp axial cutoff, whereas the ATOC data does not. This is likely the consequence of ignoring the bottom interaction near the Pioneer Seamount source, but more analysis is needed to verify the exact coupling mechanisms that are producing the complicated excitation pattern in the low modes. In addition, future work should include computing the mode estimates for more realizations of the internal wave field so that temporal statistics for the simulations can be compared to the measured coherence times from ATOC. These should incorporate the effects of the sloping bottom near the source.

Chapter 5

Conclusions and Future Directions

This dissertation has developed methods of estimating the modal content of broadband receptions and used those methods to analyze low-mode arrivals for the Acoustic Thermometry of Ocean Climate experiment. This chapter will summarize the key contributions of the work and indicate directions for future research.

The first contribution of this thesis is a general framework for broadband mode processing. Most previous work has focused on narrowband mode estimation, but recent experiments such as ATOC require wider bandwidths. This thesis has developed a mode processor based on the short-time Fourier transform and addressed the fundamental issue of the frequency resolution required for broadband mode estimation. A key advantage of the STFT approach is that it allows study of the frequency characteristics of individual arrivals (within the temporal resolution limits of the processor).

Chapter 3 explored the time- and frequency-domain characteristics of two deterministic modal beamforming algorithms: the matched filter and the pseudo-inverse filter. A detailed performance analysis using the ATOC array configuration showed that it is possible to estimate the first 10 modes using a pseudo-inverse spatial filter, and a frequency bin spacing of 2.5 Hz. The latter specification implies that the temporal resolution of the processor is on the order of 0.2 seconds (depending on the

type of temporal filter used).

The second major contribution of this work is an investigation of the low-mode arrivals in the ATOC Hawaii data set. In experiments like ATOC, understanding the axial mode arrivals is crucial because they are the most energetic signals at long ranges. The analysis presented in this thesis is the first detailed look at variability of the mode signals on short time and frequency scales. In particular, STFT processing of the Hawaii VLA receptions has identified several important features of the mode signals at 3515 km range. First, each low mode contains series of arrivals, rather than the single dispersive arrival that would characterize adiabatic propagation. This multipath structure exhibits both frequency-selective fading and significant temporal variability. Average coherence times are on the order of 6-8 minutes, which are somewhat less than the tens of minutes predicted by Flatte and Stoughton [72] and the 12.7 minute averaging times used by Worcester *et al.* [74] for the ATOC Engineering Test experiment. (Note that since some peak arrivals in the STFT estimates are coherent over the full 18.2 minute transmission, future experiments should include longer transmission times in order to measure the actual duration of these stable peaks.) Given this high degree of variability, it is not surprising that receptions at 4-hour intervals show significant differences. Each one of the transmissions effectively measures a different realization of the internal wave field. These results indicate that stochastic methods will be required for tomography and matched field applications that use the mode signals.

The mode statistics used in this thesis were computed by averaging over groups of receptions at 4-hour intervals. The leading edge, falling edge, and centroid of the mode arrivals reveal some of the expected dispersion characteristics of a deep water channel, indicating that the modes retain travel time information at megameter ranges. Both the mode centroids and the falling edges showed statistically significant changes in mean arrival time over the 5 months of data that were analyzed: decreasing arrival times from December to March followed by increasing travel times from

March to May. The observed trends agree with results for the ray arrivals over the same period of time. As noted in the Science article by the ATOC Consortium, these trends do not follow the seasonal trends in the surface layer and are likely related to a subsurface warming near the Hawaii array [73]. The RMS errors on the centroid and falling edge statistics are on the order of 20-30 ms and 30-35 ms, respectively.

PE simulations of the propagation through internal waves at $1/2$ Garrett-Munk strength model the experimental data in important respects. Since $1/2$ GM has proved useful in explaining some of the internal wave effects associated with the ray arrivals, this is a useful consistency check. The primary discrepancy between the simulations and the ATOC receptions is that the simulations show a sharp axial cut-off, whereas the experimental data does not. This thesis indicated that bathymetric coupling near the Pioneer Seamount source complicates the mode excitation pattern and may be responsible for the difference between simulated and experimental data.

In terms of future research, this thesis has laid a foundation for a stochastic channel model that is useful for modal tomography and other applications. In pursuing this ultimate goal, the rich set of data provided by the ATOC experiment merits further study. The short-time Fourier framework developed here could be extended to include methods for generating a time series from the time-varying spectral estimates of each mode. Fourier synthesis provides a useful method of examining which arrivals add coherently across frequency bands. Note that the key to implementing the synthesis step in mode processing is the dispersion correction. As indicated in Chapter 3, phase shifts across frequency due to dispersion are significant at megameter ranges. Since scattering may produce multiple arrivals in a single mode, each with its own phase characteristics, the correction will have to be done by "steering" over a set of possible corrections.

Once the methods for synthesizing modal time series have been developed, statistics of the broadband, frequency-coherent mode arrivals in the ATOC data can be measured. Time-of-arrival, temporal coherence, and intensity fluctuations are

especially of interest since comparable statistics exist for the ray arrivals. The relationship of rays and modes propagating through random internal wave fields is currently an important topic of research.

In addition to extending the STFT framework and continuing the analysis of the Hawaii data set, this thesis suggests several other intriguing topics for future research. First, the problem of modal beamforming in uncertain environments has been raised, but not solved, by this thesis. Based on the degree of mismatch between the modes for the environments measured at deployment and recovery of the ATOC arrays (described in Chapter 2), it is strongly recommended that future experiments include regular sampling of the environment at the array. Measurements of the local temperature profile, in particular, would reduce the uncertainty in the sound speed profile, thereby reducing the potential for significant modeshape mismatch.

Second, an in-depth theoretical analysis of the modal mismatch problem should be undertaken. Such a study could provide useful insights about the robustness of mode filters and set guidelines for the required temporal and spatial sampling of the environment. One approach to this problem would be to use a simple dynamical model for the mesoscale sound speed fluctuations and relate them to fluctuations in the modes using linear perturbation theory. From there it should be possible to compute performance bounds for mode estimators under a variety of conditions and to explore possible strategies for mitigating the effects of environmental uncertainty. This is a relatively open problem, although there is a large body of related work in the matched field processing literature.

Third, a study of the excitation of the axial modes by a bottom-mounted source located on a steep slope is important. The obvious starting point for this research is to model the propagation down the slope using a code, such as range-dependent OASES, that accounts for the elastic properties of the bottom. In addition to investigating the forward propagation problem, the receptions on the ATOC VLA's from a related experiment known as the Alternate Source Test (AST) should be analyzed.

This experiment used a source suspended from a ship; thus, it excited the low modes directly. A comparison of the AST data with the ATOC data might provide useful insights into the effects of the bathymetric coupling on the arrival patterns. Once the excitation pattern of the low modes is known, an interesting question to ask is whether some of the effects of the bottom interaction can be removed via deconvolution techniques. Although this is likely to be a difficult problem, a solution might provide researchers with a simpler signal for use in studying internal wave effects and/or temperature changes.

Appendix A

Acoustic Mode Perturbations

As discussed in Ch. 2, underwater acoustic normal modes satisfy a second-order eigenvalue equation:

$$\left[\frac{d^2}{dz^2} + \frac{\Omega^2}{c^2(z)} \right] \phi_m(z, \Omega) = k_m^2(\Omega) \phi_m(z, \Omega). \quad (\text{A.1})$$

Equation A.1 assumes unit density ($\rho(z) = 1, \forall z$), which is reasonable for the water-borne modes. These modes form a complete set of orthogonal basis functions and are normalized such that

$$\int_0^{z_{\max}} \phi_m(\Omega, z) \phi_n(\Omega, z) dz = \delta(m - n), \quad (\text{A.2})$$

again assuming unit density. The purpose of this chapter is to investigate how the mode wavenumbers and shapes are affected by changes in Ω , using linear perturbation theory. The discussion begins with a brief review of perturbation theory. Following that, the solution to the problem of frequency perturbations is straightforward.

Linear perturbation theory provides a method of solving for the eigenvalues and

eigenfunctions of a perturbed problem, *i.e.*,

$$\overbrace{[A + \epsilon A_1 + \epsilon^2 A_2 + \dots]}^{\tilde{A}} \tilde{\phi}_m = \tilde{\mu}_m \tilde{\phi}_m \quad (\text{A.3})$$

in terms of the solutions to an unperturbed problem

$$A\phi_m = \mu_m \phi_m. \quad (\text{A.4})$$

where the boundary conditions are the same for both problems. The intent of this section is to review standard results found in a number of references, *e.g.*, [75, 76], rather than to provide a rigorous derivation. See the book by Rellich for a thorough mathematical treatment of the problem [77]. For the purposes of this discussion, the operator A has distinct eigenvalues and its eigenvectors form a complete orthonormal (CON) set. Let the abbreviation (x, y) represent the inner product:

$$(x, y) = \int_0^{z_{max}} x(z)y(z)dz \quad (\text{A.5})$$

where x and y represent arbitrary functions of z . The following results rely on the standard assumption that the operator A is self-adjoint, *i.e.*, $(Ax, y) = (x, Ay)$.

Assuming that \tilde{A} may be written in terms of a power series in a small parameter ϵ , perturbation theory seeks solutions to Eq. A.3 of the form

$$\begin{aligned} \tilde{\mu}_m &= \mu_m + \epsilon \mu_m^{(1)} + \epsilon^2 \mu_m^{(2)} + \dots \\ \tilde{\phi}_m &= \phi_m + \epsilon \phi_m^{(1)} + \epsilon^2 \phi_m^{(2)} + \dots \end{aligned} \quad (\text{A.6})$$

Substituting A.6 into Eq. A.3 and equating terms of order ϵ yields:¹

$$A\phi_m^{(1)} + A_1\phi_m = \mu_m\phi_m^{(1)} + \mu_m^{(1)}\phi_m \quad (\text{A.7})$$

¹The ϵ^0 terms represent the unperturbed problem.

Taking the inner product of both sides with ϕ_m and solving gives the first-order corrections to the eigenvalues:

$$\mu_m^{(1)} = (A_1 \phi_m, \phi_m). \quad (\text{A.8})$$

Since the modes of the unperturbed problem form a CON set, the eigenfunction corrections can be written in terms of the modal basis set, *i.e.*,

$$\phi_m^{(1)} = \sum_{k=1}^{\infty} g_{km}^{(1)} \phi_k \quad (\text{A.9})$$

where $g_{km}^{(1)}$ is the coefficient representing the contribution of the k th mode to the first-order perturbation of the m th mode. Substituting Eq. A.9 into Eq. A.3 and taking the inner product with ϕ_k ($k \neq m$) gives the perturbation expansion coefficients:

$$g_{km}^{(1)} = \begin{cases} \frac{(A_1 \phi_m, \phi_k)}{\mu_m - \mu_k} & k \neq m \\ 0 & k = m \end{cases}. \quad (\text{A.10})$$

The second-order corrections can be obtained in a similar manner.

$$\mu_m^{(2)} = \sum_k g_{km}^{(1)} g_{mk}^{(1)} (\mu_k - \mu_m) + (A_2 \phi_m, \phi_m) \quad (\text{A.11})$$

and

$$\phi_m^{(2)} = \sum_{k=1}^{\infty} g_{km}^{(2)} \phi_k, \quad (\text{A.12})$$

where

$$g_{km}^{(2)} = \begin{cases} \frac{1}{\mu_m - \mu_k} \left[\sum_k g_{km}^{(1)} (\mu_m - \mu_k) - \mu_m^{(1)} g_{km}^{(1)} + (A_2 \phi_m, \phi_k) \right] & k \neq m \\ -\frac{1}{2} \sum_k (g_{km}^{(1)})^2 & k = m \end{cases}. \quad (\text{A.13})$$

Consider how the mode parameters vary when the desired frequency is equal to $\tilde{\omega} = \omega + \Delta\omega$. In this case, the perturbed eigenvalue problem becomes

$$\left[\frac{d^2}{dz^2} + \frac{\omega^2}{c^2(z)} \left(1 + 2\frac{\Delta\omega}{\omega} + \left(\frac{\Delta\omega}{\omega} \right)^2 \right) \right] \tilde{\phi}_m = \tilde{k}_m^2 \tilde{\phi}_m. \quad (\text{A.14})$$

Using the following definitions, this problem fits the standard form discussed above:

$$\begin{aligned} \epsilon &= \frac{\Delta\omega}{\omega}, \\ A_1 &= 2 \left(\frac{\omega^2}{c^2(z)} \right), \\ A_2 &= \frac{\omega^2}{c^2(z)}. \end{aligned}$$

Bibliography

- [1] B. M. Howe, "Acoustic Thermometry of Ocean Climate (ATOC): Pioneer Seamount Source Installation," Tech. Rep. APL-UW TM 3-96, Applied Physics Laboratory - University of Washington, Seattle, Washington, April 1996.
- [2] NOAA, National Geophysical Data Center, Boulder, CO, *Data Announcement 88-MGG-02, Digital relief of the Surface of the Earth*, 1988.
- [3] L. Brekhovskikh and Y. Lysanov, *Fundamentals of Ocean Acoustics*. New York, NY: Springer-Verlag, 2nd ed., 1991.
- [4] F. B. Jensen, W. A. Kuperman, M. B. Porter, and H. Schmidt, *Computational Ocean Acoustics*. New York, NY: AIP Press, 1994.
- [5] G. V. Frisk, *Ocean and Seabed Acoustics*. Englewood Cliffs, NJ: Prentice Hall, 1994.
- [6] S. Levitus, R. Burgett, and T. Boyer, *World Ocean Atlas 1994 Volume 3: Salinity*, 1994. NOAA Atlas NESDIS 3.
- [7] S. Levitus and T. Boyer, *World Ocean Atlas 1994 Volume 4: Temperature*, 1994. NOAA Atlas NESDIS 4.
- [8] A. B. Baggeroer, "Prüfer Transformation Methods For Determining Normal Modes of Ocean Acoustics." Unpublished - in preparation.
- [9] Y. Desaubies, "A uniformly valid solution for acoustic normal mode propagation in a range varying ocean," *J. of the Acoustical Society of America*, vol. 76, pp. 624–626, August 1984.
- [10] Y. Desaubies, C.-S. Chiu, and J. H. Miller, "Acoustic mode propagation in a range-dependent ocean," *J. of the Acoustical Society of America*, vol. 80, pp. 1148–1160, October 1986.
- [11] C. Garrett and W. Munk, "Space-time scales of internal waves: A progress report," *Journal of Geophysical Research*, vol. 80, pp. 291–297, January 1975.

- [12] W. Munk, "Internal waves and small-scale processes," in *Scientific Surveys in Honor of Henry Stommel* (B. A. Warren and C. Wunsch, eds.), ch. 9, pp. 264–291, MIT Press, 1981.
- [13] J. A. Colosi and M. G. Brown, "Efficient numerical simulation of stochastic internal-wave-induced sound-speed perturbation fields," *J. of the Acoustical Society of America*, vol. 103, pp. 2232–2235, April 1998.
- [14] M. D. Collins, *User's Guide for RAM*. Naval Research Laboratory, Washington, D.C.
- [15] W. Munk, P. Worcester, and C. Wunsch, *Ocean Acoustic Tomography*. New York, NY: Cambridge University Press, 1995.
- [16] W. Munk and C. Wunsch, "Ocean acoustic tomography: Rays and modes," *Reviews of Geophysics and Space Physics*, vol. 21, pp. 777–793, May 1983.
- [17] S. M. Flatte, R. Dashen, W. H. Munk, K. M. Watson, and F. Zachariasen, *Sound Transmission Through a Fluctuating Ocean*. Cambridge, England: Cambridge University Press, 1979.
- [18] L. Dozier and F. Tappert, "Statistics of normal mode amplitudes in a random ocean. I. Theory," *J. of the Acoustical Society of America*, vol. 63, pp. 353–365, February 1978.
- [19] L. Dozier and F. Tappert, "Statistics of normal mode amplitudes in a random ocean. II. Computations," *J. of the Acoustical Society of America*, vol. 64, pp. 533–547, August 1978.
- [20] A. Nechaev, "Sound field in an underwater waveguide with random inhomogeneities," *Soviet Physics Acoustics*, vol. 31, pp. 211–214, May-June 1985.
- [21] A. Nechaev, "Decay of the interference structure of the sound field in an ocean with random inhomogeneities," *Soviet Physics Acoustics*, vol. 33, pp. 312–314, May-June 1987.
- [22] A. Sazontov and V. Farfel, "Matched filtering of a narrowband pulse signal transmitted through a random waveguide channel," *Soviet Physics Acoustics*, vol. 38, pp. 591–595, November-December 1992.
- [23] A. Sazontov and V. Farfel, "Fluctuation characteristics of the response of a horizontal array in a randomly inhomogeneous ocean with short-time averaging," *Soviet Physics Acoustics*, vol. 37, pp. 514–518, September-October 1991.

- [24] E. Gorodetskaya, A. Malekhanov, A. Sazontov, and V. Farfel, "Effects of Long-Range Propagation of Sound in a Random Inhomogeneous Ocean on the Gain Loss of a Horizontal Antenna Array," *Acoustical Physics*, vol. 42, no. 5, pp. 543–549, 1996.
- [25] N. Vdovicheva, E. Gorodetskaya, A. Malekhanov, and A. Sazontov, "Gain of a Vertical Antenna Array in a Randomly Inhomogeneous Oceanic Waveguide," *Acoustical Physics*, vol. 43, no. 6, pp. 669–675, 1997.
- [26] A. Sazontov, "Quasiclassical solution of the radiation transport equation in a scattering medium with regular refraction," *Acoustical Physics*, vol. 42, no. 4, pp. 487–494, 1996.
- [27] E. Y. Gorodetskaya, A. I. Malekhanov, A. G. Sazontov, and N. K. Vdovicheva, "Deep-Water Acoustic Coherence at Long Ranges: Theoretical Prediction and Effects on Large-Array Signal Processing," *IEEE J. of Oceanic Engineering*, vol. 24, pp. 156–171, April 1999.
- [28] J. A. Colosi, S. M. Flatte, and C. Bracher, "Internal-wave effects on 1000-km oceanic acoustic pulse propagation: Simulation and comparison with experiment," *J. of the Acoustical Society of America*, vol. 96, pp. 452–468, July 1994.
- [29] J. A. Colosi and S. M. Flatte, "Mode coupling by internal waves for multi-megameter acoustic propagation in the ocean," *J. of the Acoustical Society of America*, vol. 100, pp. 3607–3620, December 1996.
- [30] J. A. Colosi and the ATOC Group, "A Review of Recent Results on Ocean Acoustic Wave Propagation in Random Media: Basin Scales," *IEEE J. of Oceanic Engineering*, vol. 24, pp. 138–155, April 1999.
- [31] M. G. Brown, J. Viechnicki, and F. D. Tappert, "On the measurement of modal group time delays in the deep ocean," *J. of the Acoustical Society of America*, vol. 100, pp. 2093–2102, October 1996.
- [32] H. L. V. Trees, *Detection, Estimation, and Modulation Theory, Part I*. New York, NY: John Wiley and Sons, 1968.
- [33] W. Menke, *Geophysical Data Analysis: Discrete Inverse Theory*. New York, NY: Academic Press, Inc., 1989.
- [34] R. H. Ferris, "Comparison of measured and calculated normal-mode amplitude functions for acoustic waves in shallow water," *J. of the Acoustical Society of America*, vol. 52, no. 3, pp. 981–988, 1972.
- [35] F. Ingenito, "Measurements of mode attenuation coefficients in shallow water," *J. of the Acoustical Society of America*, vol. 53, no. 3, pp. 858–863, 1973.

- [36] C. Tindle, K. Guthrie, G. Bold, M. Johns, D. Jones, K. Dixon, and T. Bird-sall, "Measurements of the frequency dependence of normal modes," *J. of the Acoustical Society of America*, vol. 64, pp. 1178–1185, October 1978.
- [37] J. J. Polcari, *Acoustic Mode Coherence in the Arctic Ocean*. PhD thesis, Massachusetts Inst. of Technology/Woods Hole Oceanographic Inst., May 1986.
- [38] G. R. Wilson, R. A. Koch, and P. J. Vidmar, "Matched mode localization," *J. of the Acoustical Society of America*, vol. 84, pp. 310–320, July 1988.
- [39] E. Shang, "Source depth estimation in waveguides," *J. of the Acoustical Society of America*, vol. 77, pp. 1413–1418, April 1985.
- [40] S. Jesus, "Normal-mode matching localization in shallow water: Environmental and system effects," *J. of the Acoustical Society of America*, vol. 90, pp. 2034–2041, October 1991.
- [41] T. Yang, "A method of range and depth estimation by modal decomposition," *J. of the Acoustical Society of America*, vol. 82, pp. 1736–1745, November 1987.
- [42] A. Voronovich, V. Goncharov, A. Y. Nikol'tsev, and Y. A. Chepurin, "Comparative analysis of methods for the normal mode decomposition of a sound field in a waveguide: numerical simulation and full-scale experiment," *Soviet Physics Acoustics*, vol. 38, pp. 365–370, July-August 1992.
- [43] J. R. Buck, J. C. Preisig, and K. E. Wage, "A unified framework for mode filtering and the maximum *a posteriori* mode filter," *J. of the Acoustical Society of America*, vol. 103, pp. 1813–1824, April 1998.
- [44] A. B. Baggeroer, B. Sperry, K. Lashkari, C.-S. Chiu, J. H. Miller, P. N. Mikhalevsky, and K. von der Heydt, "Vertical array receptions of the Heard Island transmissions," *J. of the Acoustical Society of America*, vol. 96, pp. 2395–2413, October 1994.
- [45] B. J. Sperry, "Modal Analysis of Vertical Array Receptions for the Heard Island Feasibility Test," Master's thesis, Massachusetts Inst. of Technology/Woods Hole Oceanographic Inst., May 1994.
- [46] P. N. Mikhalevsky, A. N. Gavrilov, and A. B. Baggeroer, "The Transarctic Acoustic Propagation Experiment and Climate Monitoring in the Arctic," *IEEE J. of Oceanic Engineering*, vol. 24, pp. 183–201, April 1999.
- [47] H.-Y. Chen and I.-T. Lu, "Localization of a broadband source using a matched-mode procedure in the time-frequency domain," *IEEE J. of Ocean Engineering*, vol. 19, pp. 166–174, April 1994.

- [48] J. J. Romm, *Applications of Normal Mode Analysis to Ocean Acoustic Tomography*. PhD thesis, Massachusetts Inst. of Technology, March 1987.
- [49] T. Yang, "Broadband source localization and signature estimation," *J. of the Acoustical Society of America*, vol. 93, pp. 1797–1806, April 1993.
- [50] P. Casey, "Mode Extraction for Long Range Underwater Acoustic Signals," Master's thesis, University of Auckland, February 1995.
- [51] C.-S. Chiu, C. W. Miller, and J. F. Lynch, "Optimal Modal Beamforming of Bandpass Signals Using an Undersized Sparse Vertical Hydrophone Array: Theory and a Shallow-Water Experiment," *IEEE J. of Oceanic Engineering*, vol. 22, pp. 522–533, July 1997.
- [52] P. Sutton, W. Morawitz, B. Cornuelle, G. Masters, and P. Worcester, "Incorporation of acoustic normal mode data into tomographic inversions in the Greenland Sea," *J. of Physical Oceanography*, vol. 99, pp. 12487–12502, June 1994.
- [53] K. D. Heaney, *Inverting for Source Location and Internal Wave Strength Using Long Range Ocean Acoustic Signals*. PhD thesis, University of California San Diego, 1997.
- [54] K. D. Heaney and W. Kuperman, "Very long-range source localization with a small vertical array," *J. of the Acoustical Society of America*, vol. 104, pp. 2149–2159, October 1998.
- [55] A. B. Baggeroer, W. A. Kuperman, and P. N. Mikhalevsky, "An overview of matched field methods in ocean acoustics," *IEEE J. of Oceanic Engineering*, vol. 18, pp. 401–424, October 1993.
- [56] A. Tolstoy, "Sensitivity of matched field processing to sound-speed profile mismatch for vertical arrays in a deep water pacific environment," *J. of the Acoustical Society of America*, vol. 85, pp. 2394–2404, June 1989.
- [57] W. Munk and C. Wunsch, "Ocean acoustic tomography: a scheme for large scale monitoring," *Deep-Sea Research*, vol. 26A, pp. 123–161, 1979.
- [58] E. Shang, "Ocean acoustic tomography based on adiabatic mode theory," *J. of the Acoustical Society of America*, vol. 85, pp. 1531–1537, April 1989.
- [59] E. Shang and Y. Wang, "On the possibility of monitoring El Niño by using modal ocean acoustic tomography," *J. of the Acoustical Society of America*, vol. 91, pp. 136–140, January 1992.
- [60] E. Shang and Y. Wang, "Tomographic Inversion of the El Niño Profile by Using a Matched-Mode Processing (MMP) Method," *IEEE J. of Ocean Engineering*, vol. 19, pp. 208–213, April 1994.

- [61] J. B. Allen and L. R. Rabiner, "A Unified Approach to Short-Time Fourier Analysis and Synthesis," *Proceedings of the IEEE*, vol. 65, pp. 1558–1564, November 1977.
- [62] S. H. Nawab and T. F. Quatieri, *Advanced Topics in Signal Processing*, ch. Short-Time Fourier Transform, pp. 289–337. Englewood Cliffs, NJ: Prentice Hall, 1988.
- [63] L. R. Rabiner and R. W. Schafer, *Digital Processing of Speech Signals*. Englewood Cliffs, NJ: Prentice Hall, 1978.
- [64] D. H. Johnson and D. E. Dudgeon, *Array Signal Processing: Concepts and Techniques*. Englewood Cliffs, NJ: Prentice Hall, 1993.
- [65] H. Cox, R. M. Zeskind, and M. M. Owen, "Robust adaptive beamforming," *IEEE Trans. on Acoustics, Speech, and Signal Processing*, vol. ASSP-35, p. 1365–1376, October 1987.
- [66] J. S. Lawrence Marple, *Digital Spectral Analysis with Applications*. Englewood Cliffs, NJ: Prentice Hall, 1987.
- [67] F. J. Harris, "On the Use of Windows for Harmonic Analysis with the Discrete Fourier Transform," *Proceedings of the IEEE*, vol. 66, pp. 51–83, January 1978.
- [68] A. V. Oppenheim and R. W. Schafer, *Discrete-Time Signal Processing*. Englewood Cliffs, NJ: Prentice Hall, 1989.
- [69] P. Worcester, "ATOC95: Autonomous Vertical Line Arrays Experiment Plan," 1995.
- [70] P. Welch, "The use of the Fast Fourier Transform for the estimation of power spectra," *IEEE Trans. on Audio and Electroacoustics*, vol. AU-15, pp. 70–73, June 1970.
- [71] J. A. Colosi, E. K. Scheer, S. M. Flatte, B. D. Cornuelle, M. A. Dzieciuch, P. F. Worcester, B. M. Howe, J. A. Mercer, R. C. Spindel, K. Metzger, T. G. Birdsall, and A. B. Baggeroer, "Comparisons of measure and predicted acoustic fluctuations for a 3250-km propagation experiment in the eastern North Pacific Ocean," *J. of the Acoustical Society of America*, vol. 105, pp. 3202–3218, June 1999.
- [72] S. M. Flatte and R. B. Stoughton, "Predictions of internal-wave effects on ocean acoustic coherence, travel-time variance, and intensity moments for very long-range propagation," *J. of the Acoustical Society of America*, vol. 84, pp. 1414–1424, October 1988.

- [73] The ATOC Consortium, "Ocean Climate Change: Comparison of Acoustic Tomography, Satellite Altimetry, and Modeling," *Science*, vol. 281, pp. 1327–1332, August 28 1998.
- [74] P. F. Worcester, B. D. Cornuelle, M. A. Dzieciuch, W. H. Munk, B. M. Howe, J. A. Mercer, R. C. Spindel, J. A. Colosi, K. Metzger, T. G. Birdsall, and A. B. Baggeroer, "A test of basin-scale acoustic thermometry using a large-aperture vertical array at 3250-km range in the eastern North Pacific Ocean," *J. of the Acoustical Society of America*, vol. 105, pp. 3185–3201, June 1999.
- [75] R. Courant and D. Hilbert, *Methods of Mathematical Physics*, vol. I. New York, NY: Interscience Publishers, 1953.
- [76] S. Lomov, *Introduction to the General Theory of Singular Perturbations*, vol. 112 of *Translations of Mathematical Monographs*. Providence, RI: American Mathematical Society, 1992.
- [77] F. Rellich, *Perturbation Theory of Eigenvalue Problems*. New York, NY: Gordon and Breach Science Publishers, 1969.

Document Library

Distribution List for Technical Report Exchange—November 1999

University of California, San Diego
SIO Library 0175C
9500 Gilman Drive
La Jolla, CA 92093-0175

Hancock Library of Biology & Oceanography
Alan Hancock Laboratory
University of Southern California
University Park
Los Angeles, CA 90089-0371

Gifts & Exchanges
Library
Bedford Institute of Oceanography
P.O. Box 1006
Dartmouth, NS B2Y 4 A2
CANADA

NOAA/EDIS Miami Library Center
4301 Rickenbacker Causeway
Miami, FL 33149

Research Library
U.S. Army Corps of Engineers
Waterways Experiment Station
3909 Halls Ferry Road
Vicksburg, MS 39180-6199

Institute of Geophysics
University of Hawaii
Library Room 252
2525 Correa Road
Honolulu, HI 96822

Marine Resources Information Center
Building E38-320
MIT
Cambridge, MA 02139

Library
Lamont-Doherty Geological Observatory
Columbia University
Palisades, NY 10964

Library
Serials Department
Oregon State University
Corvallis, OR 97331

Pell Marine Science Library
University of Rhode Island
Narragansett Bay Campus
Narragansett, RI 02882

Working Collection
Texas A&M University
Dept. of Oceanography
College Station, TX 77843

Fisheries-Oceanography Library
151 Oceanography Teaching Bldg.
University of Washington
Seattle, WA 98195

Library
R.S.M.A.S.
University of Miami
4600 Rickenbacker Causeway
Miami, FL 33149

Maury Oceanographic Library
Naval Oceanographic Office
Building 1003 South
1002 Balch Blvd.
Stennis Space Center, MS 39522-5001

Library
Institute of Ocean Sciences
P.O. Box 6000
Sidney, B.C. V8L 4B2
CANADA

National Oceanographic Library
Southampton Oceanography Centre
European Way
Southampton SO14 3ZH
UK

The Librarian
CSIRO Marine Laboratories
G.P.O. Box 1538
Hobart, Tasmania
AUSTRALIA 7001

Library
Proudman Oceanographic Laboratory
Bidston Observatory
Birkenhead
Merseyside L43 7 RA
UK

IFREMER
Centre de Brest
Service Documentation-Publications
BP 70 29280 PLOUZANE
FRANCE

REPORT DOCUMENTATION PAGE	1. REPORT NO. MIT/WHOI 00-08	2.	3. Recipient's Accession No.
4. Title and Subtitle Broadband Modal Coherence and Beamforming at Megameter Ranges		5. Report Date February 2000	
7. Author(s) Kathleen E. Wage		6.	
9. Performing Organization Name and Address MIT/WHOI Joint Program in Oceanography/Applied Ocean Science & Engineering		8. Performing Organization Rept. No.	
12. Sponsoring Organization Name and Address Office of Naval Research GE Fund Faculty for the Future Fellowship University of California-Scripps		10. Project/Task/Work Unit No. MIT/WHOI 00-08	
		11. Contract(C) or Grant(G) No. (C) N00014-97-1-0788 (G)	
		13. Type of Report & Period Covered Ph.D. Thesis	
15. Supplementary Notes This thesis should be cited as: Kathleen E. Wage, 2000. Broadband Modal Coherence and Beamforming at Megameter Ranges. Ph.D. Thesis. MIT/WHOI, 00-08.		14.	
16. Abstract (Limit: 200 words) Normal modes, the eigenfunctions of the ocean waveguide, are useful in underwater acoustics because the lowest modes provide an efficient description of the most energetic signals at long ranges. Understanding the structure of the mode arrivals at megameter ranges is crucial to tomographic and matched field processing applications, but there have been few opportunities for experimental observation of these signals. First, this thesis develops a short-time Fourier transform (STFT) framework for estimating broadband signals propagating in the lowest modes. Since previous research has focused on narrowband sources, this work concentrates on broadband processing issues. Specifically, it addresses the fundamental issue of frequency resolution required for mode estimation, analyzes the performance characteristics of two modal beamforming algorithms and explores the time/frequency trade-offs inherent in STFT mode processing. Second, this work presents a detailed analysis of the low-mode arrivals at megameter ranges using data from the Acoustic Thermometry of Ocean Climate experiment. Short-time Fourier processing of receptions at a range of 3,515 kilometers reveal a complicated multipath arrival structure. This thesis characterizes the temporal coherence of the arrivals, computes average dispersion curves, and examines trends in arrival time over five months of data.			
17. Document Analysis			
a. Descriptors modes acoustic broadband			
b. Identifiers/Open-Ended Terms			
c. COSATI Field/Group			
18. Availability Statement Approved for publication; distribution unlimited.		19. Security Class (This Report) UNCLASSIFIED	21. No. of Pages 146
		20. Security Class (This Page)	22. Price